

UC Irvine

UC Irvine Electronic Theses and Dissertations

Title

Extending the Chemical and Optical Sensitivity of the Scanning Tunneling Microscope

Permalink

<https://escholarship.org/uc/item/18p6g0bh>

Author

Yu, Arthur

Publication Date

2016

Peer reviewed|Thesis/dissertation

UNIVERSITY OF CALIFORNIA,
IRVINE

Extending the Chemical and Optical Sensitivity of the Scanning Tunneling Microscope
DISSERTATION

submitted in partial satisfaction of the requirements for the degree of

DOCTOR OF PHILOSOPHY

in Physics

by

Arthur Yu

Dissertation Committee:

Professor Wilson Ho, Committee Chair

Professor Peter Taborek

Professor Ruqian Wu

2016

Chapter 2 © 2015 American Chemical Society

Chapter 3, 4 © 2016 American Chemical Society

All other materials © 2016 Arthur Yu

DEDICATION

To

My parents

TABLE OF CONTENTS

	Page
LIST OF FIGURES	vi
ACKNOWLEDGMENTS	x
CURRICULUM VITAE	xii
ABSTRACT OF THE DISSERTATION	xv
Chapter 1: Introduction	1
1.1 Scanning Tunneling Microscopy and Inelastic Electron Tunneling Spectroscopy	1
1.2 IETS with Hydrogen Molecules	4
1.3 Light Emission from STM Junction	5
1.4 Methods	6
1.5 Summary of Contents	8
Bibliography	13
Chapter 2: Single-Molecule Rotational and Vibrational Spectroscopy and Microscopy with the Scanning Tunneling Microscope	15
2.1 Abstract	15
2.2 Article	16
Bibliography	31
Chapter 3: Tunneling Electron Induced Light Emission from Single Gold Nanoclusters	33
3.1 Abstract	33
3.2 Article	34

Bibliography	49
Chapter 4: Tunneling Electron Induced Charging and Light Emission of Single Panhematin Molecules	51
4.1 Abstract	51
4.2 Article	52
Bibliography	65
Chapter 5: Visualization of Nano-Plasmonic Coupling to Molecular Orbital in Light Emission Induced by Tunneling Electrons	67
5.1 Abstract	67
5.2 Article	68
Bibliography	82
Chapter 6: Concluding Remarks and Future Prospects	84
6.1 Concluding Remarks	84
6.2 Future Prospects	86
Bibliography	88
Appendix A: Operation and Maintenance of the STM2 Femtosecond Laser System	89
A.1 Introduction, Safety, and General Maintenance	89
A.2 Ti:Sapphire Femtosecond Laser Operation	92
A.3 Basic Optical Alignment	111
A.4 MIIPS Operations	116
A.5 Aligning Delay Stage	121
A.6 Aligning to the Tunnel Junction	126
Bibliography	130
Appendix B: Design and Construction of a Helium Purification System	131
B.1 Introduction	131

B.2	Generation 1	131
B.3	Generation 2	141
B.4	Generation 3	159

LIST OF FIGURES

		Page
Figure 1.1	Elastic vs. Inelastic Tunneling in STM	11
Figure 1.2	Light Emission Mechanism in STM	12
Figure 2.1	STM topography of MgP molecules on Au (110) surface	24
Figure 2.2	Measurement of dI/dV and d^2I/dV^2 at different points on MgP molecule	26
Figure 2.3	STM-IETS mapping of MgP molecule	28
Figure 2.4	IETS imaging of a MgP molecule on the Au (110)2×1 surface	30
Figure 3.1	Topography of Au nanoclusters studied in a STM junction	42
Figure 3.2	STS spectrum and photon emission for an Au nanocluster	44
Figure 3.3	Light emission spectra from individual Au nanoclusters of different sizes	46
Figure 3.4	Light emission from Au nanocluster dimers	48
Figure 4.1	STM topography of panhematicin (hemin) molecules	60
Figure 4.2	Tunneling electron induced charging of hemin molecules	62
Figure 4.3	Tunneling electron induced light emission from hemin molecules	64
Figure 5.1	STM topography of azulene on Ag (110)	75
Figure 5.2	STS measurements and imaging of azulene electronic states	77
Figure 5.3	Tunneling electron induced light emission spectrum of azulene	79

Figure 5.4	Light emission imaging of azulene with the STM	81
Figure A.1	Cleaning optics and laser crystal	91
Figure A.2	Water cooling for Verdi Laser	93
Figure A.3	Energy diagram for Ti:Sapphire lasing	95
Figure A.4	Schematic diagram of laser cavity	96
Figure A.5	Gigaoptics laser performance characteristics	98
Figure A.6	Verdi 6 laser controller front panel	99
Figure A.7	Gigajet laser cavity mirror positions	102
Figure A.8	Ti:Sapphire laser crystal holder	104
Figure A.9	Beamwalking M3 and OC	107
Figure A.10	Mounting crystal onto holder	109
Figure A.11	Quote for replacement Ti:Sapphire crystal	110
Figure A.12	Optical path for laser system in STM 2	112
Figure A.13	Alignment using irises	113
Figure A.14	Laser Power Controller front panel	115
Figure A.15	External and internal view of MIIPS	117
Figure A.16	Main Menu and Measurement Menu for MIIPS	119

Figure A.17	Optical diagram for delay stage	122
Figure A.18	Linear translator and autocorrelation	125
Figure A.19	Alignment to STM junction	127
Figure B.1	Overall structure of generation 1 purifier	132
Figure B.2	Generation 1 nitrogen tank flange	133
Figure B.3	Generation 1 purifier body top flange	135
Figure B.4	Generation 1 purifier body bottom flange	136
Figure B.5	Generation 1 purifier body 3-3/8" flange assembly	137
Figure B.6	Welding for ball valve ends	139
Figure B.7	Center hollow tube for purifier bottom	140
Figure B.8	Generation 2 purifier overall view	142
Figure B.9	Generation 2 purifier nitrogen tank flange assembly	143
Figure B.10	Generation 2 purifier nitrogen tank flange	144
Figure B.11	Generation 2 purifier condenser assembly	145
Figure B.12	Generation 2 purifier condenser bottom plate	146
Figure B.13	Generation 2 purifier outlet shield assembly	147
Figure B.14	Generation 2 purifier outlet shield top plate	148

Figure B.15	Generation 2 purifier cover flange	149
Figure B.16	Generation 2 purifier body top flange	150
Figure B.17	Generation 2 purifier body bottom flange	151
Figure B.18	Generation 2 purifier body assembly	152
Figure B.19	Generation 2 purifier zero-length reducer assembly	153
Figure B.20	Gas flow for generation 2 purifier	154
Figure B.21	Doubled-sided flange assembly	156
Figure B.22	Generation 3 purifier overall layout	160
Figure B.23	Generation 3 purifier nitrogen tank flange	161
Figure B.24	Generation 3 purifier nitrogen tank flange assembly	162
Figure B.25	Generation 3 purifier cover flange	163
Figure B.26	Generation 3 purifier cover flange assembly	164
Figure B.27	Generation 3 purifier body top flange	165
Figure B.28	Generation 3 purifier body bottom flange	166
Figure B.29	Generation 3 purifier condenser assembly	168
Figure B.30	Generation 3 purifier zero-length reducer assembly	169

ACKNOWLEDGMENTS

First and foremost, I like to thank my advisor, Professor Wilson Ho for his support and guidance through all these years. From the beginning of my time working in the group, he has shown me the value of persistence and attention to details to successful experimental work. In my years working in the group, I not only learned cutting edge science, but gain valuable experience learning to operate different experimental equipment, which is just as valuable.

I also like to thank Professor Peter Taborek and Professor Ruqian Wu for serving in both my advancement to candidacy and doctoral committees, and Professor Phil Collins and Professor Nien-Hui Ge for serving in my candidacy committee. They gave helpful advice to me for completing my thesis work.

I would not have been able to complete my degree without the former group members who taught me everything. From the first year, Ungdon Ham taught me the basics of vacuum techniques and basics of STM. Qing Huan showed me the details of running an experiment as well as operating the STM 2 laser system. In our short experimental runs together, Ying Jiang taught me many techniques that have been useful ever since. I have also benefitted from discussions and interactions with Freddy Toledo and Chilun Jiang.

Special thanks goes to the people who I have worked closely with in the group. I want to thank Weicai Cao and Hikari Kimura, for our time working in STM 4 together. It was my first time operating a STM system, and it was great experience learning with these guys. At STM 2, I have worked with Shaowei Li for all of the experiments done in this thesis. He has been a great

partner and I could not have completed all the experiments without him. I have worked with Greg Czap as well and I thank him also.

All the former and current group members I have worked with in one way or another deserve a mention here. They are: Xiuwen Tu, Chi Chen, Shiwei Wu, Zhumin Han, Chen Xu, Haigang Zhang, Hankyu Lee, Calvin Patel, Christian Kim, Peter Wagner, Siyu Chen, Likun Wang, and Jiang Yao. They have contributed to a friendly and enlightening environment in the lab.

Since the beginning of my time in the group, I have had to use the machine shop for different projects. Lee Moritz and Chris Peterson at the shop have been tremendous help through the years, and I thank them for it.

Lastly, I want to thank my friends and family for their support and encouragement through the years. In particular I like to thank my parents. They have made enormous sacrifices to give me the opportunity for higher education; I love them and I deeply appreciate all they have done for me.

This work is supported by the National Science Foundation Center for Chemical Innovation on Chemistry at the Space-Time Limit (CaSTL) under Grant No. CHE-0802913.

CURRICULUM VITAE

TEL: 646-284-1805

Email: ayul@uci.edu

Dept. of Physics and Astronomy, UC-Irvine

Irvine, CA, 92697. U.S.A

Arthur Yu

Education

- July 2016 Ph.D. Physics, University of California, Irvine. Irvine, CA, USA
- (2008-2016) Thesis: “Extending the Chemical and Optical Sensitivities of the Scanning Tunneling Microscope” Supervisor: Prof. Wilson Ho
- May 2008 B.A. Physics, Mathematics, New York University, New York, NY, USA
- (2004-2008)

Work Experience

- Sep 2008 – Jun 2014 Teaching Assistant, Department of Physics, Department of Mathematics, UCI
- Sep 2007 – May 2008 Grader, Department of Mathematics, NYU
- Oct 2006 – Jun 2008 Research Assistant, Kent Lab, Department of Physics, NYU

Honors and Scholarship

- 2009 Graduate Research Fellowship, UCI
- 2007 Sigma Pi Sigma Prize, Society of Physics Students, NYU.

Conference Presentations

- Nov 2015 ACS Western Regional Meeting: “Visualization of Electron-Photon-Plasmon Coupling in Single Azulene Molecules with the STM”
- Mar 2014 APS March Meeting: “Chemically Sensitive Imaging of Magnesium Porphyrin with STM”
- Nov 2013 AVS International Symposium: “Atomic Scale Photochemistry with STM”

Publications

1. Arthur Yu, S.W. Li, W. Ho, to be submitted to *Phys. Rev. Letts.*
“Visualization of Nano-Plasmonic Coupling to Molecular Orbital in Light Emission Induced by Tunneling Electrons”
2. Arthur Yu, S.W.Li, B. Dhital, H.P. Lu, W. Ho, *J. Phys. Chem. C* **2016**, DOI: 10.1021/acs.jpcc.6b04087
“Tunneling Electron Induced Charging and Light Emission of Single Panhematin Molecules”
3. Arthur Yu, S.W. Li, G. Czap, W. Ho, *Nano Letters* **2016**, DOI: 10.1021/acs.nanolett.6b01824
“Tunneling Electron Induced Light Emission from Single Gold Nanoclusters”
4. Arthur Yu, S.W. Li, G. Czap, W. Ho, *J. Phys. Chem. C* **2015**, 119, 26
“Single-Molecule Rotational and Vibrational Spectroscopy and Microscopy with the STM”
5. S.W. Li, D.W. Yuan, Arthur Yu, G. Czap, R.Q. Wu, W. Ho, *Phys. Rev. Letts.* **2015**, 114, 206101
“Rotational Spectromicroscopy: Imaging the Orbital Interaction between Molecular Hydrogen and an Adsorbed Moleculee”
6. S.W. Li, Arthur Yu, F. Toledo, Z.M. Han, H. Wang, H.Y. He, R.Q. Wu, W. Ho, *Phys. Rev. Letts.* **2013**, 111, 146102.
“Rotational and Vibrational Excitations of a Hydrogen Molecule Trapped within a Nanocavity of Tunable Dimension”

Professional Skills and Experiences

Experience with homemade low temperature ultrahigh vacuum STM system

- Experiments on single molecule imaging, tunneling spectroscopy, and photon emission
- Construction of STM scanner, electronics, and supporting vacuum systems
- Use of low temperature cryogenic equipment, continuous flow cryostat, transferring of liquid helium
- Design of vacuum systems such as evaporators, leak checking stations
- Proficient with machining: lathe and milling machine
- Instrumental control with Labview software

Experience with femtosecond lasers, photon collection, photon imaging with STM

- Experiments on single molecule photon emission, spectrally resolved photon imaging, femtosecond pump probe experiment set up
- Operation and maintenance of Ti:Sapphire femtosecond laser system
- Optical spectroscopy with nitrogen cooled CCD

Experience with liquid helium purification and recycling system

- Design and construction of helium purifier system
- Design and construction of helium liquefier cold head
- Installing of piping for helium recycling system
- 3D modeling with AutoCad Inventor

Experience with teaching college level math and physics

- Held discussion and lab sections for introductory physics and mathematics
- Held office hours and tutoring center hours
- Prepare and grade quizzes, midterm and final exams

ABSTRACT OF DISSERTATION

Extending the Chemical and Optical Sensitivity of the Scanning Tunneling Microscope

by

Arthur Yu

Doctor of Philosophy in Physics

University of California, Irvine, 2016

Professor Wilson Ho, Chair

This dissertation discusses the theoretical basis and experimental applications to improving the capability of the STM in chemical and optical sensitivity. Traditional STM methods have achieved unprecedented spatial resolution, but suffer from a lack of sensitivity to chemical structure and composition. A new method of imaging, based on inelastic electron tunneling spectroscopy (IETS) measurement of hydrogen molecules is developed. The interaction of plasmon excitations to electronic states of a metal nano-cluster is also studied, allowing for better understanding of the mechanisms involved in the plasmon – electron coupling.

Since its application at the single molecule level in the STM was realized, IETS has been used to identify different molecules through their vibrational signal. In recent experiments, rotational excitation of H_2 was detected on metal and insulator surfaces. It was found that the energy of these excitations depend sensitively on the local chemical environment. By monitoring the rotational and vibrational IETS signal of the H_2 across the molecule, a more chemically sensitive image can be constructed. When the method is applied to imaging magnesium porphyrin (MgP) on Au (110), different components of the molecule can be observed at different energies. These differences are indication of how the various components interact with the H_2 .

Optical sensitivity of the STM manifests in the detection of photons emitted from the tunnel junction. Previous experiments have shown that we can map the excitation of molecular fluorescence with sub-Angstrom resolution. For applications in photochemistry and catalysis, understanding how plasmons interact with photons and electrons is crucial. Light emission from Au nanoclusters on oxide shows strong correlation with their electronic states. The interaction between plasmon mode in the junction and electronic states of the nano-clusters is further studied through clusters of different sizes and dimers. Emission of light from molecular orbitals is also investigated in panhematin and azulene molecules. Coupling of molecular orbital and vibronic states to junction plasmon is found and visualized through light emission spectrum and imaging.

Chapter 1

Introduction

1.1 Scanning Tunneling Microscopy and Inelastic Electron Tunneling Spectroscopy

The scanning tunneling microscope (STM) has been known to be able to image nanostructures with atomic resolution [1-6]. The origin of its high spatial resolution comes from the exponential dependence of the tunneling current on the tip – sample distance. In a simplified model, the tip and the substrate can be viewed as electrodes separated by a vacuum barrier (Fig. 1.1a). Quantum tunneling occurs between the electrodes when their electron wave functions overlap in the vacuum region. Typically, the tunneling is elastic, with the electron keeping their energy in the tunneling process. If a bias is applied between the electrodes, a net current will result. To understand the physics behind the process, a brief theoretical discussion follows below.

According to Bardeen theory of tunneling, the tunneling current can be expressed as:

$$I = \frac{4\pi e}{h} \int_{-\infty}^{\infty} [f_s(E_F - eV + \epsilon) - f_t(E_F + \epsilon)] \rho_s(E_F - eV + \epsilon) \rho_t(E_F + \epsilon) |M|^2 d\epsilon \quad (1)$$

where f is the Fermi function, e is the electron charge, V is the bias voltage, ρ_s and ρ_t are the densities of states for the sample and tip respectively, and M is the tunneling matrix element [7]. Several insights can be gained from equation (1). The Fermi function f is temperature dependent, but at the experimental conditions that will be discussed in this dissertation, deviation from the zero temperature case will be minimal. Further, if the bias is low, only states very close to the Fermi energy will contribute to the tunneling current. In effect, this reduces the range of integration to a small energy range around the Fermi levels for tip and sample. The spatial information is contained in the matrix element M , where the overlap between the wave functions

of the tip and substrate is calculated. In most cases, calculation of the tunneling matrix is a non-trivial matter, but in the low temperature, low bias limit, several simplifications can be made. In such a regime, the tunneling matrix can be viewed as energy independent [8-9]. With these approximations, the current can be expressed as:

$$I \propto \int_0^{eV} \rho_s(E_F - eV + \epsilon) \rho_t(E_F + \epsilon) d\epsilon \quad (2)$$

As we can see, the current now becomes a convolution of the electron densities of states of the tip and substrate.

Following the analysis above, it is clear that the tunneling current, thus the STM image, depends on electron density of states near the Fermi level. This has the effect that STM topography does not in general correspond to the chemical structure of the object imaged. In imaging molecules, the molecular orbitals near the Fermi level play an important role. As such, topographic images often depend on imaging bias, and can reflect the spatial distribution of the molecular orbitals [10]. For metallic substrates, the electrons near the Fermi level are delocalized, this, coupled with the fact that most prominent tip states are *s* states, makes it difficult to image single atoms on metal surfaces with bare metal tip. Atomic resolution is possible, but usually only at small tip-sample separation or after the tip electronic state is modified by attaching a molecule [11]. The dependence of the STM image on electronic states near the Fermi level makes the STM a poor discerner of chemical elements.

Besides imaging, the STM can also be used in spectroscopy. With the feedback disabled and the tip fixed over an atom or molecule, we can measure the response of the tunneling current as a function of bias. The resulting spectrum (I-V curve) can give us insight to the electronic properties of said atom or molecule. To better discern features on the I-V curve, it is useful to

consider the differential conductance, defined as dI/dV . Differentiating equation (2) with respect to bias V , we get:

$$\frac{dI}{dV} \propto \rho_s(E_F + eV)\rho_t(E_F) \quad (3)$$

Equation (3) shows the physical meaning of the dI/dV spectrum: it is proportional to the density of states of the sample at voltage V . Assuming that the tip states are independent of bias, any electronic state in the sample (or molecular orbital) will lead to an increased conductance through resonant tunneling into that state (orbital), resulting in a peak in the dI/dV spectrum. The ability to probe the electronic states of the substrate molecules makes tunneling spectroscopy an indispensable tool in surface science.

In addition to the elastic tunneling detailed above, which is the dominant mechanism in STM topography scans, tunneling can also occur inelastically (Fig. 1.1b). In such a case, the tunneling electron loses energy to an excitation (molecular vibration, rotation, phonon, plasmon, etc.) before tunneling to the substrate. The effect of the inelastic tunneling is that it opens a new conductance channel, increasing the conductance above the threshold energy. From the spectrum, the inelastic tunneling creates a step in the dI/dV curve. In general, the cross section for inelastic tunneling is small, and the increase in conductance is difficult to detect experimentally. To discern the minute IETS signal from noise, it is more convenient to monitor the d^2I/dV^2 signal, which will have a peak at the energy $\hbar\omega$ of the excitation. This method leads to better signal to noise ratio and more precise determination of the inelastic excitation energy. Note that in IETS the signal should be symmetric around zero bias, as the excitation could occur from electrons tunneling from either the tip or the substrate.

The advent of IETS to the STM gives it additional capability. Because the vibrational modes of a molecule are unique to it, the IETS signature can be used as a tool to identify different molecules. Early experiment had successfully distinguished C_2H_2 and C_2D_2 from their IETS spectrum while their topographic images look the same [12]. Combination of IETS with STM imaging has allowed visualization of molecular vibrations at the single molecule level [6]. Despite the successes of IETS, it has definite drawbacks. Only selected vibrational modes can be measured and the selection rules are non-trivial [13-15].

1.2 IETS with Hydrogen Molecules

As the simplest molecule in chemistry, hydrogen (H_2) has always been a model system in quantum mechanics due to availability of analytical solutions to Schrödinger's Equation. Due to its simplicity, rotational motion of the H_2 can be modeled with the 3D rigid rotor model. In this model, the rotational energy of the molecule is given by:

$$E = \frac{j(j+1)\hbar^2}{2\mu r_b^2} \quad (4)$$

where j is the rotational quantum number, \hbar is the reduced Planck's constant, μ is the reduced mass of H_2 , and r_b is the distance between the two H atoms. For the two nuclear spin states of ortho and para-hydrogen, symmetry selection rules will dictate what rotational state the molecule can be in. Interactions with metal surfaces will also change the ratio of ortho to para-hydrogen [16-17].

As a candidate for IETS study, H_2 has many advantages including small mass and therefore large mass difference between it and its isotope D_2 . This results in large difference in rotational energies between the two species and makes for easy identification. However, the

detection of rotational excitation for single hydrogen molecule with STM-IETS has only recently been realized [18-19]. The $j = 0 \rightarrow 2$ transition for para-hydrogen on metal and decoupler surfaces was observed with STM-IETS. To achieve this, it is crucial that H_2 interacts weakly with the substrate so that the free rigid rotor model mentioned above remains valid. In the geometry of the STM junction, the adsorption potential cannot confine the H_2 in the tunnel junction indefinitely. Molecules diffuse in and out of the nanocavity formed by the tip and substrate, in a time scale much faster than that of an IETS spectrum.

Due to the placement of the STM tip, we can tune the potential well felt by the H_2 by varying the distance between the tip and substrate. In doing so, it is possible to modify the chemical structure of the H_2 . This in turn results in a shift of the rotational energy of the molecule. Thus, the rotational energy of H_2 can serve as a sensor for the local chemical environment. Taking advantage of this can lead to a more chemically sensitive imaging technique for the STM.

1.3 Light Emission from STM Junction

Soon after its invention, the STM was used in the study of optical processes through tunneling induced light emission. Early experiments included light emission from metal and semiconductor surfaces [20-22]. It was a natural development as the spatial resolution of the STM gave it a decisive advantage over conventional optical techniques. The ability to excite photon emission with precise spatial resolution allows for study of emission from single molecules and nanostructures (Fig. 1.2a).

In the STM junction, the light emission mechanism involves heavily the tunneling junction plasmon mode. In both experimental and theoretical studies, the light emission spectrum

and intensity depends on the plasmon mode in the junction [23-24]. This plasmon in turn depends on tip material and shape, as well as the substrate. Light emission occurs as a result of inelastic electron tunneling process, where tunneling electron loses energy to the junction plasmon, and decay of the plasmon is detected in the far field as emitted photon (Fig. 1.2b). In the light emission of single molecules, the IET process is only one of possible emission channels. Molecular fluorescence, in which emission arises from transition between molecular orbitals (Fig.1.2b), had been studied with sub-molecular resolution [25-27]. The current dissertation expands upon the results of previous experiments and investigates the interaction between the junction plasmon and molecular electronic and vibronic states.

1.4 Methods

All experiments described in this dissertation were performed in a homebuilt variable temperature STM whose design was described elsewhere [28]. In order to ensure atomically clean surface and minimum thermal effects, experiments were conducted at low-temperature, ultrahigh vacuum conditions. The vacuum chamber, after baking, has a base pressure of 3×10^{-11} Torr. To achieve low temperature operation, a continuous flow liquid helium cryostat is used, reaching an equilibrium temperature of 10 K. Thermal fluctuation is around ± 2 mK/s. Continuous helium flow and refill capability, coupled with minimum X-Y drift, allow for uninterrupted experimental measurement over single molecule / nanostructure for days and even weeks.

Sample and tip treatment was performed prior to each experimental run. Typically, the single crystal metal sample is cleaned by repeated cycles of Ne^+ sputtering and annealing. Annealing temperature and time depends on sample type. On the NiAl (110) surface, a thin layer

of Al_2O_3 is grown to decouple the molecule / nanocluster from the metal substrate. To achieve this, the sample is exposed to O_2 at 1×10^{-6} Torr for 3 mins while maintaining temperature of 800 K. The oxidized surface is then crystallized by annealing to 1200 K, yielding oxide patches covering approximately 50% of the surface. All experiments were performed with Ag tips electro-chemically etched from Ag wires. A mixture of $\text{NH}_3(\text{aq})$, H_2O_2 , and ethyl alcohol solution is used with AC voltage in the first step and DC voltage in the second step. In the vacuum chamber, the tips are cleaned with cycles of annealing, Ne^+ sputtering, and annealing again. For optical experiments, the light emission intensity is closely related to tip plasmon resonance. To ensure best experimental results, multiple tips were tested for light emission before each experiment and the one with best emission characteristics was selected.

To measure the dI/dV or d^2I/dV^2 signal in STS or IETS, the lock-in technique was used. With the feedback disabled, a small sinusoidal modulation is added to the bias voltage. The response of the current is monitored with the lock-in amplifier. The first harmonic output of the lock-in is then proportional to the dI/dV signal and second harmonic output is proportional to the d^2I/dV^2 signal. In general, the modulation amplitude is an important parameter to tune to achieve best signal to noise ratio. A large modulation amplitude allows for increased signal, but also introduces broadening effects to the spectroscopic line shape. For IETS features which require high energy resolution, a balance has to be struck to obtain the best results.

The light emission from the tunnel junction was collected with a lens inside the vacuum chamber and guided to a nitrogen cooled charged coupled device (CCD) equipped with a monochromator and spectrograph. The details on how to properly align the system for data taking will be discussed in Appendix A. To study light emission from molecules and nanoclusters, there are two ways to take the data. A single spectrally resolved photon spectrum

can be taken with the tip stationary over a molecule. To create a photon emission image, the STM software is used to send out a TTL pulse at each scanning pixel to start a full emission spectrum. A Labview software is then used to reconstruct the image. Detailed description of the process can be found in Chi Chen's thesis [29].

1.5 Summary of Contents

So far in the introduction, we have discussed the background for IETS and light emission in STM and the need to improve the chemical and optical sensitivities of the instrument. In the following chapters, we describe experiments conducted to further these goals, not only establishing promising experimental techniques, but giving important insights to controlled interactions in the STM junction. A brief description of the chapters is presented below.

Chapter 2: "Single-Molecule Rotational and Vibrational Spectroscopy and Microscopy with the Scanning Tunneling Microscope", published in *Journal of Physical Chemistry C*, describes H₂ vibrational and rotational image of magnesium porphyrin (MgP) molecules adsorbed on Au (110) surface. Taking advantage of the varying local potential represented by the MgP to the H₂, IETS images at the vibrational and rotational energies of the H₂ were performed. Results highlighted different chemical components of the MgP and elucidated the interaction between H₂ and MgP.

Chapter 3: "Tunneling Electron Induced Light Emission from Single Gold Nanoclusters", published in *Nano Letters*, describes the interplay between electronic and optical properties of nanoclusters adsorbed on Al₂O₃ / NiAl (110) surface. Dosed at room temperature, Au nanoclusters exhibit quantum confined electronic states. Light emission spectra and imaging show light emission stems from inelastic electron tunneling to the nanocluster electronic states.

Analysis from size dependence and nanocluster dimer studies gives further insight to the interaction between nanocluster electronic states and tunnel junction plasmon.

Chapter 4: “Tunneling Electron Induced Charging and Light Emission of Single Panhematin Molecules”, published in *Journal of Physical Chemistry C*, describes charging and light emission from panhematin (hemin) molecules adsorbed on $\text{Al}_2\text{O}_3 / \text{NiAl}$ (110) surface. STS measurements on hemin show presence of LUMO at 1.3 eV, which becomes the SOMO / SUMO upon injection of an electron from the tip. Light emission spectrum indicates emission mechanism resulting from decay of molecular vibronic states. The experiment reveals a unique emission mechanism from previous experiment on porphyrin based molecules and lets us gain new insight into the electron-plasmon interaction.

Chapter 5: “Visualization of Nano-Plasmon Coupling to Molecular Orbital in Light Emission Induced by Tunneling Electrons”, to be submitted to *Physics Review Letters*, describes the interaction between molecular orbital of azulene adsorbed on Ag (110) surface and the surface plasmon resonance (SPR) studied through tunneling electron induced light emission. Light emission spectrum shows enhancement when tip is placed over the molecule. Bias dependent studies and photon imaging show correlation between molecular orbital and light emission, highlighting the electron-plasmon-photon interaction in the tunnel junction.

The concluding Chapter 6 summarizes the results and significance of the dissertation. A brief discussion on the future prospects and applications of the methods described in the previous chapters is included.

The Appendices describe two instrumentation projections the author was involved with during the time the dissertation was completed. Appendix A describes the operation and

maintenance of the femtosecond laser system that is critical to the light emission experiments described in this dissertation. Appendix B describes the design and construction of the helium purifier installed in the helium recycling facility.

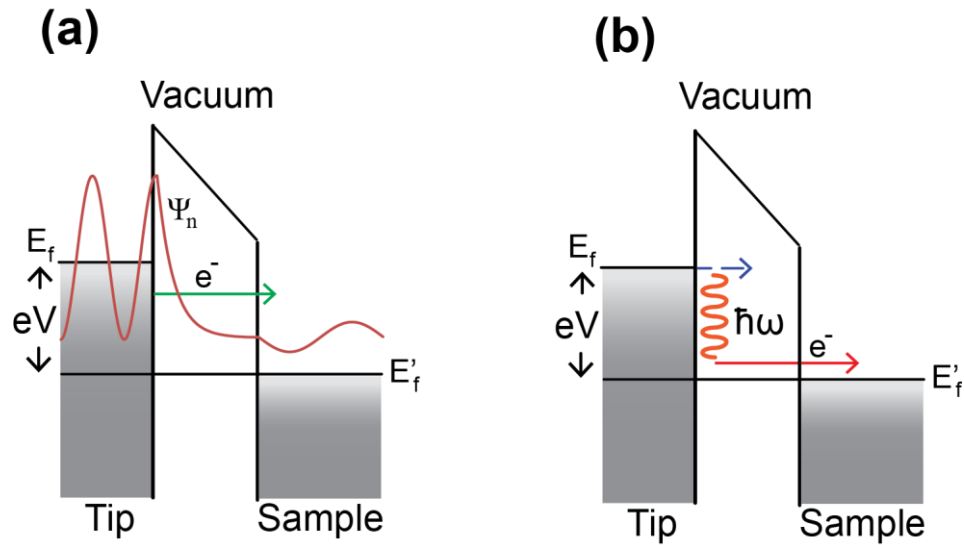


Fig. 1.1: Elastic vs. Inelastic Tunneling in STM

Energy diagrams for tunneling process in the STM junction. (a) Electrons tunnel elastically from the filled states in the tip to the empty states in the sample. The electron wavefunctions of the tip and sample are also shown. (b) Electrons lose energy $\hbar\omega$ to an excitation, such as molecular vibration or rotation, before tunneling to sample.

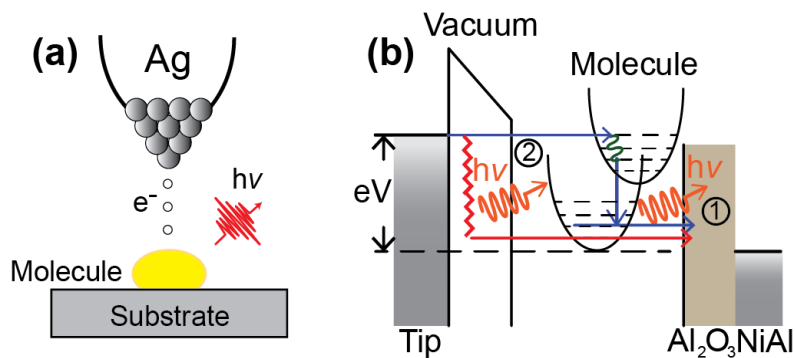


Fig. 1.2: Light Emission Mechanism in STM

Tunneling electron induced light emission from the STM. (a) Schematic diagram of the light emission process, in which tunneling electrons interaction with a molecule adsorbed on the surface, and emits light through molecular transitions or excitation and decay of the tunnel junction plasmon. (b) Energy diagram for two emission mechanism from the STM. One is molecular florescence, where electron tunnels to a vibrationally excited molecular orbital, which then decays radiatively. The second is an inelastic electron tunneling process, where the electron loses energy to a plasmon in the tunnel junction, and light emission results from decay of the plasmon. The presence of oxide layer is crucial to molecular florescence due to increased lifetime of the electron in the molecule.

Bibliography

- [1] G. Binnig, and H. Rohrer, *Helv. Phys. Acta.* **55**, 726 (1982).
- [2] G. Binnig, H. Rohrer, C. Gerber, and E. Weibel, *Phys. Rev. Lett.* **50**, 120 (1983).
- [3] R.M. Feenstra, J.A. Stroscio, J. Tersoff, and A.P. Fein, *Phys. Rev. Lett.* **58**, 1192 (1987).
- [4] M.F. Crommie, C.P. Lutz, and D.M. Eigler, *Science* **262**, 218 (1993).
- [5] P. Avouris, and R. Wolkow, *Phys. Rev. B* **39**, 5091 (1989).
- [6] W. Ho, *J. Chem. Phys.* **117**, 11033 (2002).
- [7] J. Bardeen, *Phys. Rev. Lett.* **6**, 57 (1961).
- [8] J. Tersoff, and D.R. Hamann, *Phys. Rev. Lett.* **50**, 1998 (1983).
- [9] J. Tersoff, and D.R. Hamann, *Phys. Rev. B* **31**, 805 (1985).
- [10] C.J. Chen. *Introduction to Scanning Tunneling Microscopy* (Oxford Univ. Press, 2008).
- [11] L. Bartels, G. Meyer, and K.H. Rieder, *App. Phys. Lett.* **71**, 213 (1997).
- [12] B.C. Stipe, M.A. Rezaei, and W. Ho, *Science* **280**, 1732 (1998).
- [13] M. Reed, *Mater. Today* **11**, 46 (2008).
- [14] N. Lorente, and M. Persson, *Phys. Rev. Lett.* **85**, 2997 (2000).
- [15] N. Lorente, M. Persson, L.J. Lauhon, and W. Ho, *Phys. Rev. Lett.* **86**, 2593 (2001).
- [16] K. Makoshi, M. Rami, and E. Ilisca, *J. Phys. Condens. Matter* **5**, 7325 (1993).

- [17] K. Svensson, S. Andersson, Phys. Rev. Lett. **98**, 096105 (2007).
- [18] S.W. Li, A. Yu, F. Toledo, Z.M. Han, H. Wang, H.Y. He, R.Q. Wu, and W. Ho, Phys. Rev. Lett. **111**, 146102 (2013).
- [19] F.D. Natterer, F. Patthey, and H. Brune, Phys. Rev. Lett. **111**, 175303 (2013).
- [20] J.K. Gimzewski, J.K. Sass, R.R. Schlitter, and J. Schott, Europhys. Lett. **8**, 435 (1989).
- [21] A. Downes, and M.E. Welland, Phys. Rev. Lett. **81**, 1857 (1998).
- [22] N. Nilius, N. Ernst, H.J. Freund, and P. Johansson, Phys. Rev. B **61**, 12682 (2000).
- [23] P. Johansson, R. Monreal, and P. Apell, Phys. Rev. B **42**, 9210 (1990).
- [24] R. Berndt, J.K. Gimzewski, and P. Johansson, Phys. Rev. Lett. **67**, 3796 (1991).
- [25] X.H. Qiu, G.V. Nazin, and W. Ho, Science **299**, 542 (2003).
- [26] S.W. Wu, G.V. Nazin, and W. Ho, Phys. Rev. B **77**, 205430 (2008).
- [27] C. Chen, P. Chu, C.A. Bobisch, D.L. Mills, and W. Ho, Phys. Rev. Lett. **105**, 217402 (2010).
- [28] B.C. Stipe, M.A. Rezaei, and W. Ho, Rev. Sci. Instr. **70**, 137 (1999).
- [29] C. Chen, Ph.D. Dissertation, U.C. Irvine, 2009.

Chapter 2

Single-Molecule Rotational and Vibrational Spectroscopy and Microscopy with the Scanning Tunneling Microscope*

2.1 Abstract

A new method of imaging with the scanning tunneling microscope (STM) is used to study magnesium porphyrin (MgP) molecules adsorbed on Au(110) surface. Hydrogen molecules are deposited onto the surface and diffuse freely until temporarily trapped in the tunnel junction. The vibrational and rotational modes of the H₂ are monitored with inelastic electron tunneling spectroscopy (IETS) with the STM. The MgP presents the H₂ with a highly localized position-dependent adsorption potential, which causes variations in the energies of both vibrational and rotational modes of the trapped H₂ molecule. Imaging at the vibrational and rotational energies of H₂ reveals salient features in the chemical structure of the MgP molecule, in particular, the positions of the nitrogen atoms. The electrostatic interaction between H₂ and MgP plays a crucial role in determining the imaged features, which provide a visualization of the interaction potential within the MgP molecule.

*This chapter by A. Yu, S.W. Li, G. Czap and W. Ho has been previously published under the same title in *J. Phys. Chem. C*, **119**, 206101 (2015). Copyright © 2015 by American Chemical Society.

2.2 Article

1. INTRODUCTION

Since its invention, the scanning tunneling microscope (STM) has become a powerful tool for investigating atomic scale phenomena with unparalleled spatial resolution. It has been used to study surface structure [1], single molecule chemistry [2], and nanostructures by atomic manipulation [3]. Despite these successes, a steady goal has been to extend the chemical and structural sensitivities of the STM. Because STM derives its spatial resolution from sensitivity of the tunneling current to tip-sample distance and local electron density of states, STM topography images rarely replicate molecular structure in detail. As such, chemical identification from STM topography with a bare metal tip is nearly impossible. Over the years, various efforts were made to develop new techniques for the STM to overcome these challenges. The advent of inelastic electron tunneling spectroscopy (IETS) with the STM partly alleviated the problem of chemical identification, as molecules and complexes can be identified by their vibrational signatures [4]. While atomic scale resolution is achieved, selected vibrational modes are observed, requiring theoretical analyses of the inelastic tunneling cross sections and selection rules are distinct for STM-IETS [5-6].

More recently, developments in non-contact atomic force microscopy (NC-AFM) [7], scanning tunneling hydrogen microscopy (STHM) [8], and inelastic tunneling probe (itProbe) [9] have provided the possibility to image chemical structures of molecules with unprecedented detail. In all of the above techniques, a “functionalized” tip with a probe molecule is necessary, such as a CO molecule bonded to the tip or a H₂ trapped in the tunnel junction. In general, the interaction between a molecule adsorbed on the surface and the probe molecule causes changes

in the probe molecule, which can be detected as a change in tunneling current in the STM or resonant frequency of the AFM. This interaction must depend sensitively on the relative positions of the adsorbed and probe molecules, giving the techniques their spatial resolution. Using the same basic principle, here we introduce a new method for imaging with the STM which allows for resolution of the internal features of an adsorbed magnesium porphyrin (MgP) molecule on the Au(110) 2×1 reconstructed surface. This technique, based on the rotational excitation of H_2 , offers new insights into the interactions between the MgP and H_2 molecule, and extends the capability of H_2 to act as a sensor of its local chemical environment.

The rotational excitations of H_2 molecules weakly adsorbed on surfaces of metal and decoupling layers have been measured with the STM [10-11]. It was also shown that changes in the adsorption potential well induced by varying the tip – sample distance shift the energies of both vibrational and rotational modes for the hydrogen temporarily trapped in the tunnel junction [10]. In this respect, the vibrational and rotational modes of H_2 behave similarly to vibrations of a CO molecule attached to the tip [9]. We can take advantage of the sensitivity of the H_2 modes to their local chemical environment to image the structure of adsorbed molecules in greater detail than is possible with bare metal tip. On the Au(110) 2×1 surface, H_2 can diffuse freely and be trapped in the tunnel junction of the STM, even over an adsorbed molecule. While the diffusion rate of the H_2 molecules in and out of the tunnel junction is much faster than the average imaging time, each H_2 feels the same chemical environment. The MgP molecule is ideal for STM studies due to its nearly planar geometry. In addition, the presence of nitrogen atoms and the central magnesium atom presents a diverse chemical environment to the trapped H_2 molecule, so the interaction between the H_2 and different chemical components can be probed within a single adsorbed molecule.

2. Experiment

The experiment was performed in a home-built STM system operating at temperature of 10 K and base pressure of 3×10^{-11} Torr [12]. The Au(110) 2×1 surface was prepared by repeated cycles of Ne^+ sputtering and annealing to 680 K. The STM tips were electro-chemically etched from high purity Ag wires. Upon lowering the temperature to 10 K, MgP molecules were thermally evaporated onto the surface. The H_2 gas was introduced into the chamber at a pressure of 1×10^{-10} Torr for at least 5 minutes. CO molecules were also dosed onto the surface, allowing the possibility of transferring a CO molecule to the tip for increasing the imaging resolution.

3. Results and Discussion

In the absence of H_2 as imaged by the bare metal tip, MgP molecules appear as a two-lobed square protrusion straddling the reconstructed Au rows (Fig. 2.1a). In comparison, topographic image taken in the presence of H_2 is shown in Fig. 2.1b, and that taken additionally with a CO-terminated tip (in the presence of H_2) is shown in Fig. 2.1c. A schematic diagram of the adsorption site of MgP on Au(110) 2×1 is shown in Fig. 2.1d. After dosing the surface with H_2 , the H_2 molecules diffuse freely on the Au(110) 2×1 surface with adsorbed MgP molecules (Fig. 2.1e). Due to Pauli repulsion between electrons in the H_2 molecules and in atoms of the substrate, high resolution images of the substrate can be obtained when certain conditions are met [13-14]. In this regime, it is possible to resolve the Au atoms on the surface [10]. Even outside this regime, however, the effect of H_2 can be readily seen in Fig. 2.1b, where the 4-lobe symmetry of the MgP is restored.

To investigate the interaction between H_2 and MgP, we performed IETS measurements at different points within the molecule. Figure 2.2 shows dI/dV (panel a) and d^2I/dV^2 (panel b)

spectra taken over the central Mg atom, the site of a nitrogen atom, and over the center of the pyrrole ring. To locate these features within the molecule, an image was taken with a CO-terminated tip (top of figure), which shows the outline of molecule (see also Fig. 2.1c). In each spectrum, two features are particularly notable: the lower energy dip in d^2I/dV^2 corresponding to the excitation of the vibrational mode with H₂ bouncing against the surface (orange dashed line), and the higher energy peak in d^2I/dV^2 corresponding to excitation of the rotational mode of H₂ (black dashed line). Comparing spectra taken over different locations, it is apparent that both the energy and the relative intensity of these two modes change sensitively with tip position, hence local chemical environment.

Figure 2.3 shows IETS spectra taken by positioning the tip at different positions along an axis of the molecule. The dashed lines indicate the positions of the vibrational and rotational energies of H₂ at these different positions over the molecule. As the tip was moved from the outer edge to the center of the molecule, there is an upshift of both the vibrational and rotational energies. Over the Au surface and around the carbon five-member rings, the vibrational energies are 11-12 meV. This mode energy shifts to 19 meV near the nitrogen atoms and to 27 meV over the Mg atom. The rotational energy also shifts, but not as significantly. It increases from 38 meV over the carbon rings to 42.5 meV over the Mg atom.

In Figure 2.4, we performed IETS imaging at different biases. From these images, several interesting features can be seen. In images taken at 13 mV and 30 mV about the vibrational mode, features emerge that mirror the symmetry of the underlying Au lattice. The two small circular features on two sides of the center in the image at 30 mV, after lateral distance calibration, match with positions of Au atoms underneath, indicating the possible involvement of trough atoms in the bonding between MgP and Au surface. Results from this image were included in the

determination of the schematic diagram in Fig. 2.1d. At the rotational energy of 43 meV, we can see four lobes in the image. From a comparison with the calibrated molecular skeleton, these lobes correspond to the positions of the four nitrogen atoms. These features are not clearly resolved or even absent when the imaging bias is off resonance of the rotational peak, as shown for 39 mV (Fig. 2.4c) and 45 mV (Fig. 2.4e). Interference from the vibrational line shape is absent on the high energy side of the rotation, hence the sharpness of rotational imaging is demonstrated by the lack of strong features in Fig. 2.4e. Overall, the d^2I/dV^2 images reveal chemical and structural information of the adsorbed molecule not seen in constant current topography (Fig. 2.4f). These results introduce spectroscopic vibrational and rotational imaging and provide an opportunity to better understand the interaction potentials among H₂, MgP, and the Au substrate.

In standard theory, the energy of a vibrational mode of a molecule is influenced by the curvature of the interaction potential. The large upshift of the vibrational energy for H₂ toward the center of the MgP suggests that the curvature of the interaction potential is larger near the center of the MgP molecule than near the outer rings. The increase in intensity of the IETS signal near the center could be due to a larger IETS cross section and increased trapping time of the H₂ in the tunnel junction. Since only one molecule is in the junction at a time, a rough estimate gives that the trapping time increases by a factor of two, in proportion to the IETS signal intensity. The exact nature of the IETS line shape and intensity change, however, is beyond the scope of this paper. The presence of substrate features in the IETS imaging (Fig. 2.4b) indicates the important role Au surface atoms play in determining the interaction potential between MgP and H₂. That should not be a surprise, as in the absence of a decoupling layer, the molecular orbitals of MgP hybridize with the electronic states of the Au substrate. As such, the molecule-substrate

interaction can also contribute to increased binding of H_2 to the center of MgP. Similarly, variation in the interaction potential can also transform the geometry (i.e. bond length) of the H_2 , causing a shift in its rotational energy. Figures 2.2 and 2.3 indicate that there is a downshift of the rotational energy when H_2 is over the outer rings of the MgP, as compare to over bare Au surface and center of the molecule. The energy shift suggests that the bond length of H_2 is increased over the porphyrin rings.

Because the energy of the vibrational and rotational modes of H_2 depend sensitively on its interaction potential with the MgP, the spatial distribution of these excitations at certain energies reveals details of the potential energy surface. The role of the molecule's different chemical constituents in shaping the interaction potential surface can be investigated through vibrational and rotational microscopy. As we have seen, prominent substrate features in the IETS imaging at 30 mV (Fig. 2.4b) suggest that surface Au atoms play an important role in determining the interaction potential for H_2 . The clear features matching the positions of the four nitrogen atoms in the IETS image at 43 mV (Fig. 2.4d) reveal similarly important contributions from the nitrogen atoms. The effect from the central Mg atom can also be seen by the relatively weak feature in the image at 45 mV (Fig. 2.4e). It is evident that these IETS images at the vibrational and rotational energies provide detailed information about the spatial distribution of the interaction potential between H_2 and the adsorbed molecule, highlighting the effects of the molecule's different chemical constituents in this interaction.

The interaction potential between the trapped H_2 and MgP is mostly dominated by the electrostatic interaction, which gives rise to the high resolution imaging by NC-AFM and IETS-STM, as recently proposed by Hapala and colleagues [15]. When the tip is close to the surface, the relaxation of the probe molecule in response to the highly localized Pauli repulsion by the

surface molecule sharpens the electrostatic features which follow closely the molecular skeleton. The experiment presented here is in the regime where the STM tip is far away enough from the substrate such that Pauli repulsion is negligible. If that had not been the case, topography of the MgP molecule would resemble those previously found in STHM experiments [13]. In this regime, the image is dominated by the probe-sample (in this case, H₂ and MgP) electrostatic interaction, resulting in direct resemblance of the image to the Hartree potential. The IETS images from Figure 2.4 can then be interpreted as the Hartree potential cross sections at various energies [16]. Features associated with the Au atoms in Fig. 2.4b and the N atoms in Fig. 2.4d can be thought of as electronegative centers that preferentially trap the H₂ molecule as reflected in the enhanced signals.

4. Conclusions

In conclusion, we have shown that vibrational and rotational excitations of H₂ molecules can be used as a probe to image adsorbed molecules in greater structural and chemical details than possible by topographic imaging. While H₂ IETS imaging cannot resolve features as sensitively as itProbe with CO tip, it still elucidates the structure of the imaged molecule and its interaction with H₂. Analyses of the images reveal the electrostatic forces that are involved in the interaction between H₂ and MgP. Vibrational and rotational IETS imaging of the H₂ over the adsorbed MgP relates to the Hartree potential of the MgP molecule. Results presented in this paper show the great potential of H₂ IETS imaging as a tool to resolve and visualize the spatial distribution of the interaction potential within an adsorbed molecule.

Fig. 2.1 STM topography taken (a) before H₂ exposure, at set point V_B = 50 mV, I_T = 0.1 nA, (b) with background H₂, at same set point, (c) with CO terminated tip in H₂ environment, at V_B = 500 mV, I_T = 0.1 nA. The rows of surface Au atoms are resolved in these topographic images. (d) Adsorption geometry of magnesium porphyrin (MgP) molecule on Au(110)2×1 reconstructed surface. The first, second, and third atomic layers of the Au surface are depicted by distinct colors with increasing lightness. (e) Schematic of tunneling junction, with a single H₂ diffusing over the MgP molecule and being temporarily trapped in the tunneling junction.

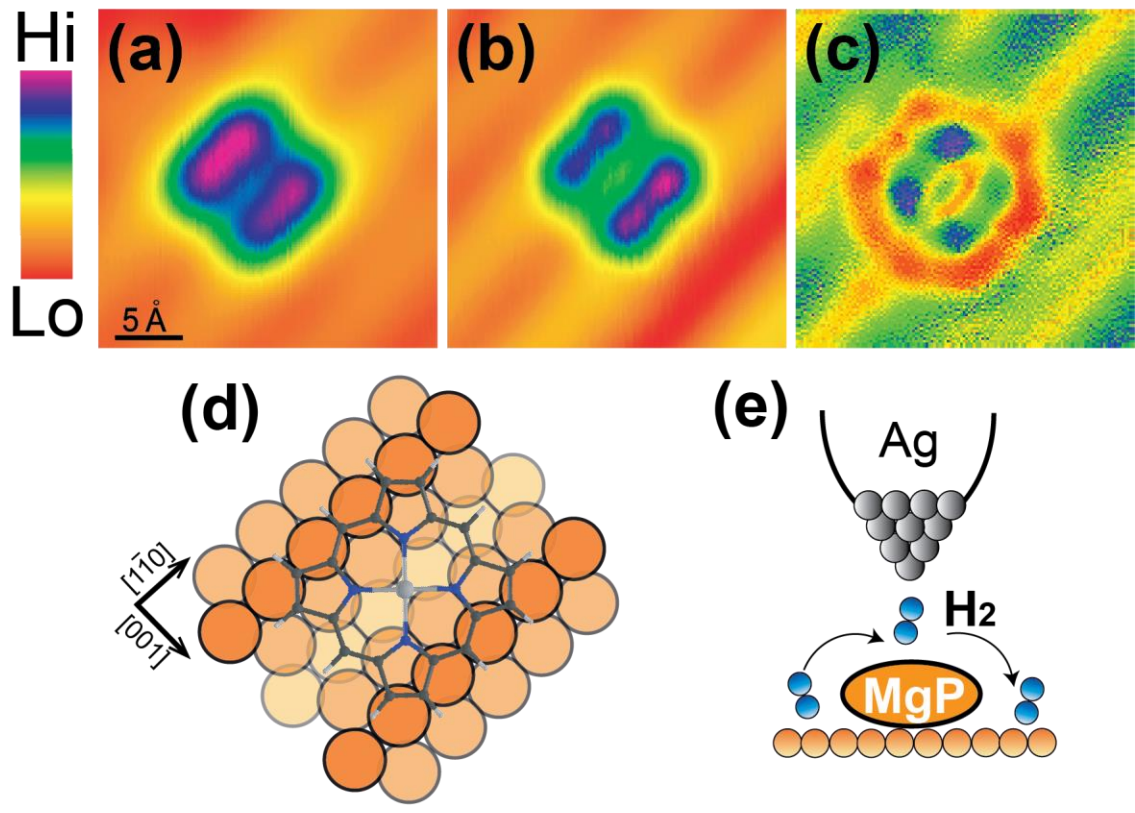


Fig. 1

Fig. 2.2 Measurement of (a) dI/dV and (b) d^2I/dV^2 spectra over different points in the molecule. The topographic image at the top was taken with CO-terminated tip and overlaid with a scaled molecular skeletal structure of MgP. Position of the tip for each spectrum is indicated by a color dot in the image. The orange and black dash lines indicate positions for the vibrational and rotational energies of the H₂, respectively. The background spectrum was taken over the Au surface in the absence of H₂. All spectra were taken at a set point of $V_B = 50$ mV, $I_T = 1$ nA, from -60 mV to 60 mV with lock-in modulation at 341 Hz and $V_{rms} = 3$ mV.

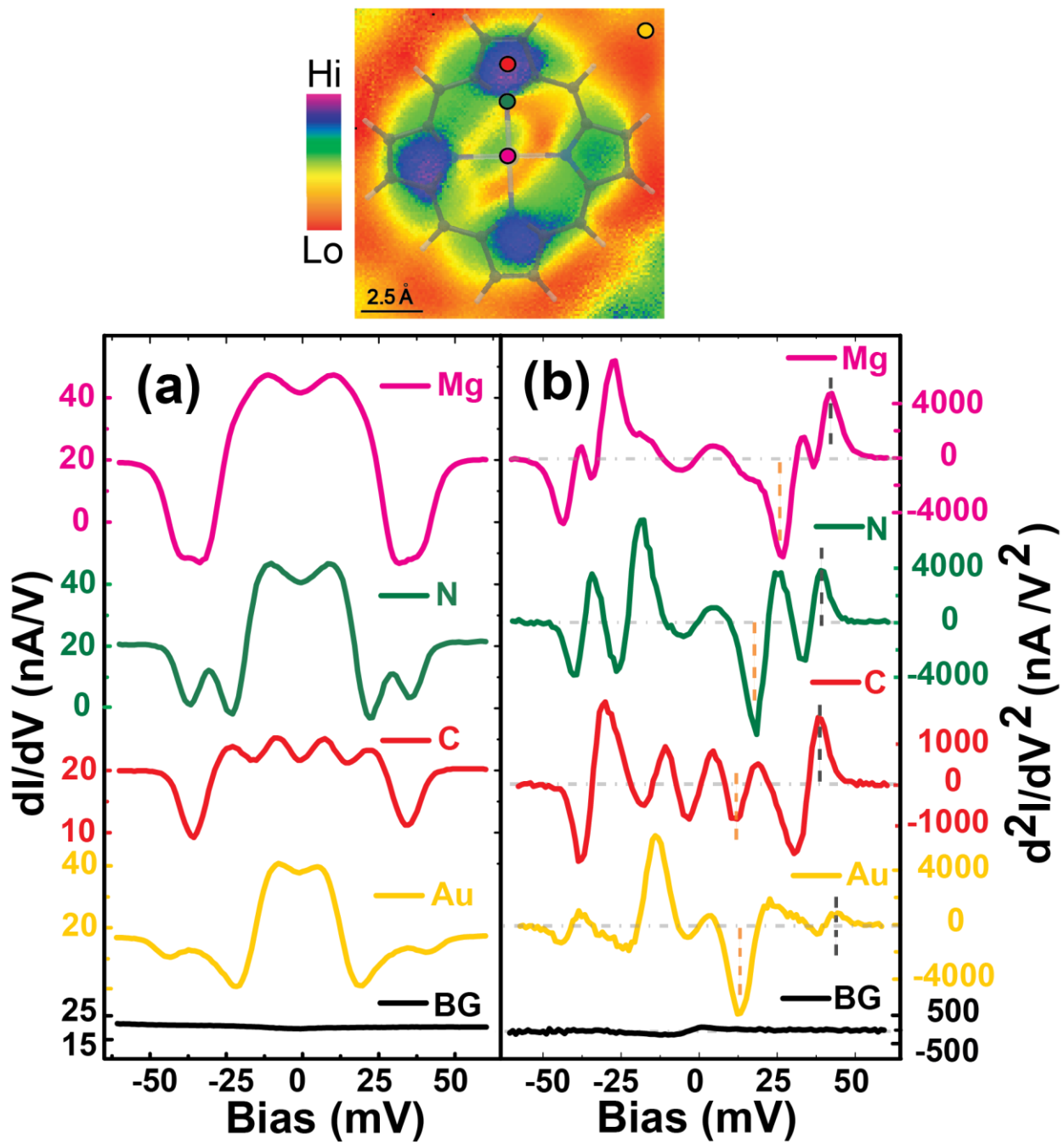


Fig. 2

Fig. 2.3 STM-IETS mapping of MgP molecule. d^2I/dV^2 was measured at 11 points along an axis of the MgP (top). The position of each spectrum is indicated by a colored dot on the topographic image, as well as by the number scale on the right side of the image. All spectra were taken with set point $V_B = 50$ mV, $I_T = 1$ nA, bias from -60 mV to 60 mV, with lock-in modulation at 341 Hz and $V_{rms} = 3$ mV. The two inner dashed lines indicate the energy of the vibrational (bouncing against the surface) mode of the H_2 . The two outer dashed lines indicate the energy of the $j = 0 \rightarrow 2$ rotational excitation of H_2 . The dashed lines are drawn through peak / dip positions on the x – axes (the actual energy positions), not through the maxima / minima of the peaks / dips. As the tip moves toward the center of the molecule, both the vibrational and rotational energies shift up.

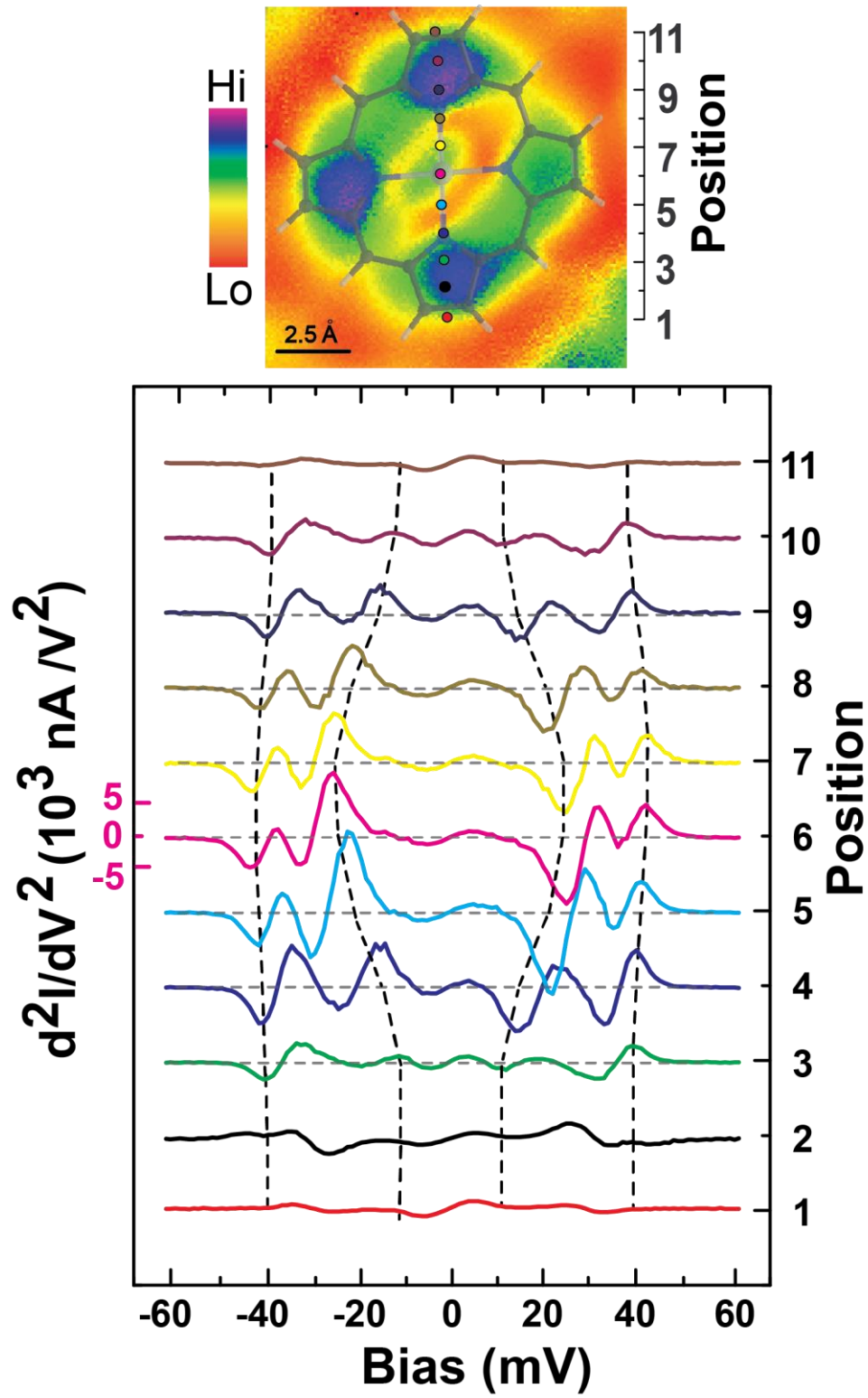


Fig. 3

Fig. 2.4 (a) – (e) IETS imaging of a MgP molecule on the Au (110)2×1 surface. In all images, the junction was set at $V_B = 50$ mV, $I_T = 1$ nA at each pixel, followed by disabling the feedback, ramping the bias to a chosen voltage, and recording d^2I/dV^2 signal by lock-in technique. The junction was reset at same set point following lock-in measurement. Thus each image depicts the spatial distribution of the d^2I/dV^2 signal strength at that particular voltage. A scaled model of MgP molecule is overlaid in (d) to show positions of the lobes in the image correspond to positions of the four nitrogen atoms. (f) For comparison, constant current topographic image taken at set point $V_B = 50$ mV, $I_T = 1$ nA.

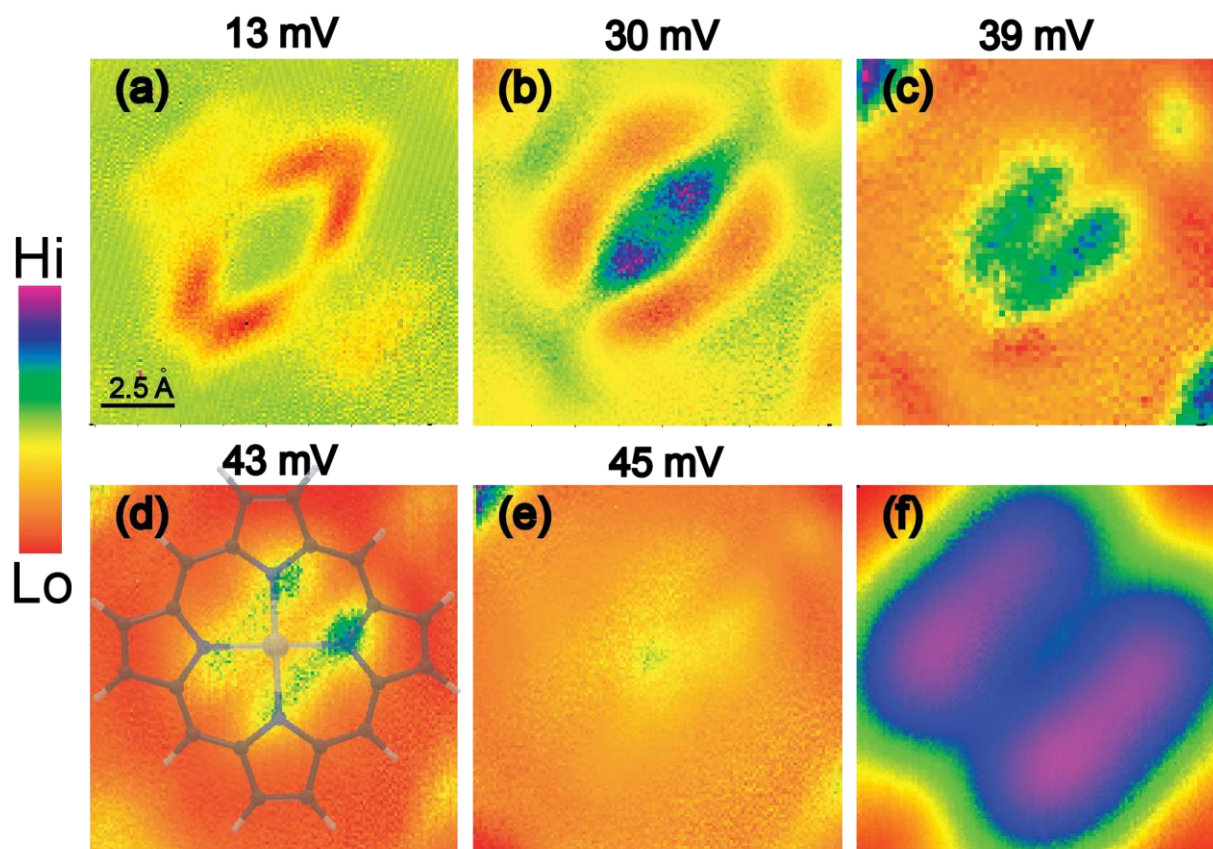


Fig. 4

Bibliography

- [1] G. Binning, H. Rohrer, C. Gerber, and E. Weibel, *Phys. Rev. Lett.* **50**, 120 (1983).
- [2] W. Ho, *J. Chem. Phys.* **117**, 11033 (2002).
- [3] M.F. Crommie, C.P. Lutz, and D.M. Eigler, *Science* **262**, 218 (1993).
- [4] B.C. Stipe, M.A. Rezaei, and W. Ho, *Science* **280**, 1732 (1998).
- [5] M. Reed, *Materials Today* **11**, 46 (2008).
- [6] N. Lorente, and M. Persson, *Phys. Rev. Lett.* **85**, 2997 (2000).
- [7] L. Gross, F. Mohn, N. Moll, P. Liljeroth, and G. Meyer, *Science* **325**, 1110 (2009).
- [8] R. Temirov, S. Soubatch, O. Neucheva, A.C. Lassis, and F.S. Tautz, *New J. Phys.* **10**, 053012 (2008).
- [9] C.L. Chiang, C. Xu, Z.M. Han, and W. Ho, *Science* **344**, 885 (2014).
- [10] S.W. Li, A. Yu, F. Toledo, Z.M. Han, H. Wang, H.Y. He, R.Q. Wu, and W. Ho, *Phys. Rev. Lett.* **111**, 146102 (2013).
- [11] F.D. Natterer, F. Patthey, and H. Brune, *Phys. Rev. Lett.* **111**, 175303 (2013).
- [12] B.C. Stipe, M.A. Rezaei, and W. Ho, *Rev. Sci. Instr.* **70**, 137 (1999).
- [13] C. Weiss, C. Wagner, C. Kleimann, M. Rohlfing, F.S. Tautz, and R. Temirov, *Phys. Rev. Lett.* **105**, 086103 (2010).
- [14] N. Moll, L. Gross, F. Mohn, A. Curioni, and G. Meyer, *New J. Phys.* **12**, 125020 (2010).

[15] P. Hapala, G. Kichin, C. Wagner, F.S. Tautz, R. Temirov, and P. Jelínek, Phys. Rev. B **90**, 085421 (2014).

[16] P. Hapala, R. Temirov, F.S. Tautz, and P. Jelínek, Phys. Rev. Lett. **113**, 226101 (2014).

Chapter 3

Tunneling Electron Induced Light Emission from Single Gold Nanoclusters*

3.1 Abstract

The coupling of tunneling electrons with the tip-nanocluster-substrate junction plasmon was investigated by monitoring light emission in a scanning tunneling microscope (STM). Gold atoms were evaporated onto the ~ 5 Å thick Al_2O_3 thin film grown on the NiAl (110) surface where they formed nanoclusters 3 – 7 nm wide. Scanning tunneling spectroscopy (STS) of these nanoclusters revealed quantum-confined electronic states. Spatially resolved photon imaging showed localized emission hot spots. Size dependent study and light emission from nanocluster dimers further support the viewpoint that coupling of tunneling electrons to the junction plasmon is the main radiative mechanism. These results showed the potential of the STM to reveal the electronic and optical properties of nanoscale metallic systems in the confined geometry of the tunnel junction.

*This chapter by A. Yu, S.W. Li, G. Czap, and W. Ho has been published in *Nano Letters* under same title. DOI: 10.1021/acs.nanolett.6b01824. Copyright © 2016 by American Chemical Society.

3.2 Article

The ability of plasmons to amplify and focus electric fields in confined spaces has made plasmonics an expanding field of study in recent years. The surface plasmon resonance of metallic nanoclusters, in particular, has been shown to play an important role in fields such as catalysis, surface science and photochemistry [1-3]. To take advantage of plasmon excitations in these studies, an understanding of the interactions among plasmon, electron, and photon is crucial. At the single molecule and nanocluster level, study of light emitted in the far field can give valuable insights on these interactions occurring in the near field.

The scanning tunneling microscope (STM) can be a useful tool in the investigation of nanocluster plasmonics. Early experiments on metal and semiconductor surfaces demonstrated STM's ability to induce light emission from the tunnel junction [4-6]. Due to the high spatial resolution of tunneling electrons, the STM acts as a localized low energy electron source, allowing for local excitation of plasmon modes within the STM junction [7-8]. Tunneling electron induced light emission has been shown to have sub-molecular resolution [9-12]. In theoretical studies of STM induced light emission, the geometry and composition of the tunnel junction play a crucial role in the photon emission process [13-14]. Silver nanoclusters have been characterized by STM induced light emission images [15] and their electronic structure simulated by theoretical calculations [16]. The tip-substrate junction plasmon mode can dictate whether light emission can occur or be detected. The direct coupling between the tip-substrate plasmon and electronic states in the junction, however, has not been widely studied. The high spatial resolution of the STM allows for the possibility of studying such tip-nanocluster-substrate plasmon in the STM junction.

In this paper, we investigate the electronic and optical properties of Au nanoclusters deposited on thin Al₂O₃ patches grown on the NiAl (110) surface. Au atoms were thermally evaporated onto the Al₂O₃ / NiAl (110) surface at room temperature. Due to their high mobility, the atoms congregate to form nanoclusters several nanometers in size. The nanoclusters tend to form on the oxide patches, with a few isolated atoms on the metal surface. The electronic structure of the clusters was studied with scanning tunneling spectroscopy (STS), and showed signs of quantum confinement effect. Tunneling electron induced light emission from Au nanoclusters, schematically shown in Fig. 3.1a, exhibit strong plasmon enhanced emission at 1.7 eV. Spatially resolved photon imaging showed the light emission is localized to certain locations of the nanocluster. Size dependence of light emission as well as light emission from nanocluster dimers were also studied, providing insights to the interaction between electronic states in the nanocluster and junction plasmon mode.

The experiment was performed in a home-built low temperature STM, operating at a temperature of 10 K and base pressure of 3×10^{-11} Torr [17]. The NiAl (110) surface was cleaned by repeated cycles of Ne⁺ sputtering and annealing to 1200 K. Al₂O₃ layer was grown by exposing the NiAl sample to oxygen at 1×10^{-6} Torr for 3 minutes while maintaining sample temperature at 800 K, followed by annealing to 1200 K to crystallize the oxide patches. The nanoclusters were formed by thermally evaporating Au from an alumina crucible onto the sample at room temperature. Typical surface landscape after dosing is shown in Fig. 3.1b. The tip was electro-chemically etched from high purity Ag polycrystalline wires. Bias voltage was applied to the sample with the tip at virtual ground. Light emission from the tunnel junction was collected with a lens inside the vacuum chamber and guided to a liquid nitrogen cooled charged couple device (CCD) attached to a monochromator [9-11].

After dosing, Au atoms form nanoclusters on the Al_2O_3 ranging from 3 to 7 nm in size. The size of the nanoclusters does not exceed more than 10 nm, even if dosing time and current are increased. Profile line cuts of nanoclusters give their average height at around 1.2 – 1.5 nm (Fig. 3.1c), approximately 1/3 to 1/4 of their lateral dimensions. The density of nanoclusters can be controlled by dosing time and current, yielding reproducible and suitable surface landscape. The ease with which we can control the nanocluster coverage gives us a wide range of cluster shapes and sizes to study, as well as dimers of nanoclusters separated by different distances (e.g. Fig. 3.1d).

Here, we study Au nanoclusters, such as the one shown in Fig. 3.2a. In addition to measuring the tunneling electron induced light emission through the mechanism illustrated in Fig. 3.2b, the electronic properties of these nanoclusters were characterized using scanning tunneling spectroscopy (STS). For the Au nanocluster of Fig. 3.2a, its dI/dV spectrum is shown in Fig. 3.2c, revealing multiple peaks representing the electronic states in the nanocluster. Due to variations in nanocluster shape, size, and adsorption geometry on the oxide surface, the energy of electronic states can vary by as much as 0.2 eV. Some nanoclusters only have two visible states, while others can have up to four, such as the nanocluster shown in Fig. 3.2c. From previous experiments on artificially constructed Au chains, the conductance value measured at different points along the chain can resemble the spatial distribution of states in a one dimensional particle in a box [18-19]. These states arise when the electronic states in the nanostructure are confined in one or more directions [20]. The electronic states in the Au nanoclusters presented here can be viewed as the extension of quantum confined states in quasi two dimensions. The presence of the oxide insulating layer isolates the nanocluster electronic states from the substrate and provides the boundary conditions required to form particle-in-a-box like states.

The inset (Fig. 3.2d – 2g) shows the spatial distribution of dI/dV for each of the four electronic peaks in the nanocluster. The resulting images display variations in the signal intensity across either horizontal (Fig. 3.2d) or vertical directions (Fig. 3.2e), as well as more complicated patterns (Fig 3.2f, 2g). Such spatial variations coincide with results expected from quantum confined electronic states, as they show more complex spatial dependence as the energy of the state increases. The lack of symmetry in the images follows from the irregular shape of the nanocluster. The origin of the nanocluster states as particle-in-a-box states can be further confirmed by performing a line cut of the dI/dV images at 1.6 V and 2.25 V (Fig. 3.2h). The positions of the peaks in the curve for the 1.6 V state correspond directly to the dips in the 2.25 V state, qualitatively consistent with the characteristics expected for quantum confined states.

The tunneling electron induced light emission from the same Au nanocluster is shown in Fig. 3.2i. The photon spectrum was collected with the tip positioned over the center of the cluster, and the tunnel junction set at $V_B = 3.0$ V and $I_T = 12$ nA. The emission spectrum shows a broad peak centered at 1.7 eV according to the radiative mechanism illustrated in Fig. 3.2b. Electrons from the tip tunnel inelastically by losing energy to a plasmon mode in the tunnel junction: the tip-nanocluster-substrate junction plasmon. Light is detected in the far field from the decay of the plasmon mode. The strong coupling between the electronic transition associated with the inelastic electron tunneling and the plasmon mode is the reason for the strong light emission signal observed. In the present case, particular care should be taken when considering the bias voltage applied to the nanocluster due to the finite voltage drop across the oxide. Previous study on $Al_2O_3 / NiAl$ (110) surface has shown that the voltage drop across the oxide is approximately 1/7 of the value compared to the vacuum gap [21-22]. The exact value depends on tip – substrate distance. Calculating the actual voltage applied to the nanocluster using this information, we find

that the transition energy between bias voltage at 3.0 V and electronic state at 1.1 V is reduced by a factor of 7/8, resulting in a value of 1.66 eV that matches the peak of photon emission spectrum in Fig. 3.2i.

To further study the plasmonic properties of the nanocluster junction, a spatially resolved photon imaging of the Au cluster was recorded in Fig. 3.2j. At each point in the image, the photon intensity was measured by integrating the photons emitted in the energy range shaded in blue in Fig. 3.2i. The resulting image shows that the light emission is localized to a few “hot spots” along the edges of the nanocluster. A way to understand the spatial distribution of the light emission image came from an earlier experiment, where it was demonstrated that spatial variations of the light emission and electronic states in a metal chain are connected through Fermi’s Golden Rule [23]. Since the light emission mechanism is similar in the two experiments, in principle we should be able to make the same connection here. The fact that the electronic states are quasi two dimensional in the present case makes visualization much less straightforward. Unlike the one-dimensional metal chains, where the electron wave functions are simple sinusoidal functions, the irregular shape of the nanocluster as well as inhomogeneity of the oxide surface produce more complex electronic states. Thus, it will be difficult to compare light emission images with derivative of wave functions as is possible in the one dimensional metal chains.

The interaction between the STM junction plasmon and nanocluster electronic states can be studied further by looking at light emission from nanoclusters of various sizes. Fig. 3.3a shows photon emission spectra for four different clusters ranging from 2.4 nm (Fig. 3.3b) to 4.5 nm (Fig. 3.3e). As the particle size increases, we see a broadening of the light emission peak, as well as a slight upshift in peak energy. Both of these phenomena can be explained with the

emission mechanism described above. As the size of the quantum well increases, both the energy of its ground state and the spacing between energy level decrease. Because of this, the inelastic transition from the initial state at 3.0 V to nanocluster electronic state will increase in energy, leading to a blue shift of the emitted photon spectrum. Closer spacing between successive electronic levels also means that there may be multiple electronic states that are coupled with the junction plasmon mode, leading to a broadening of the light emission spectrum.

We also studied light emission from nanocluster dimers, such as the pair in Fig. 3.4a. The plasmon induced field enhancement effect that occurs in the confined space between two nanoclusters has been studied and exploited in many optical experiments [24-25]. In Fig. 3.4b, the spatial distribution of the intensity for light emission from two closely situated Au nanoclusters is shown. When the tip is situated over the center of either nanocluster, the light emission spectrum (Fig. 3.4c, the upper two curves in purple and blue) is similar to emission from single clusters. In the region between the dimer, the photon emission is significantly lower. The photon intensity mapping (Fig. 3.4b) further reflects this result.

When the electric field is enhanced between two nanoclusters, its polarization lies parallel to the axis joining the two nanoclusters, thus is also parallel to the substrate surface. Since the tip-nanocluster-substrate junction plasmon has polarization along the tip-substrate axis and therefore perpendicular to the surface, the enhanced field would have negligible coupling to the junction plasmon, contributing insignificantly to the light emission process. Furthermore, the photon image (Fig. 3.4b) corresponds to the spatial distribution of the excitation probability for the radiative process when the tip is placed at each pixel of the image. In order for photon emission to occur, the tunneling electrons have to interact with the electronic states of the nanocluster in the tip-nanocluster-substrate junction. As the dI/dV images in Fig. 3.2 show, the

electronic states are confined spatially in the same region as the STM topography of the nanocluster. This means that if the tip is placed off the nanocluster, even in between two nanoclusters, the probability of the tunneling electrons to couple radiatively with the electronic states of the nanoclusters dramatically decreases. Similar phenomenon has been seen in electron microscopy experiments [26-27]. These results further reinforce the idea that the light emission originates from the coupling of inelastic tunneling electrons to the tip-nanocluster-substrate junction plasmon.

In summary, we have investigated the electronic and optical properties of oxide supported Au nanoclusters using the STM. STS measurements reveal quantum confined electronic states that couple to the tip and substrate and together form the tip-nanocluster-substrate junction plasmon that is excited by the tunneling electrons to produce photon emission. Light emission studies from nanoclusters of varying sizes, as well as from cluster dimers, further confirm this optical phenomenon. Our studies have demonstrated the integration of nanocluster electronic states and plasmon within the confined STM junction, and the possibility of the composite tip-nanocluster-substrate plasmon to decay by the emission of light. Understanding these processes will greatly enhance our ability to utilize Au nanoclusters in diverse applications in plasmonics. This experiment shows the potential of the STM to probe the electron – plasmon interaction mediated by a single nanocluster.

Fig. 3.1 Au nanoclusters studied in a STM junction. (a) Schematic of experimental setup. Au nanoclusters are deposited on $\text{Al}_2\text{O}_3 / \text{NiAl}$ (110) surface and tunneling electron induced light emission is studied. (b) Large area topography scan of $\text{Al}_2\text{O}_3 / \text{NiAl}$ (110) surface, showing distribution of Au nanoclusters. Image taken at $V_B = 3.0$ V, $I_T = 0.1$ nA. (c) Profile line cut of a nanocluster. Inset shows constant current topography of the cluster. Image taken at $V_B = 3.0$ V, $I_T = 1.0$ nA. Height of nanocluster was calibrated from the Ag (110) step edge. (d) Topography of Au nanocluster dimer, imaged at $V_B = 3.0$ V, $I_T = 1.4$ nA.

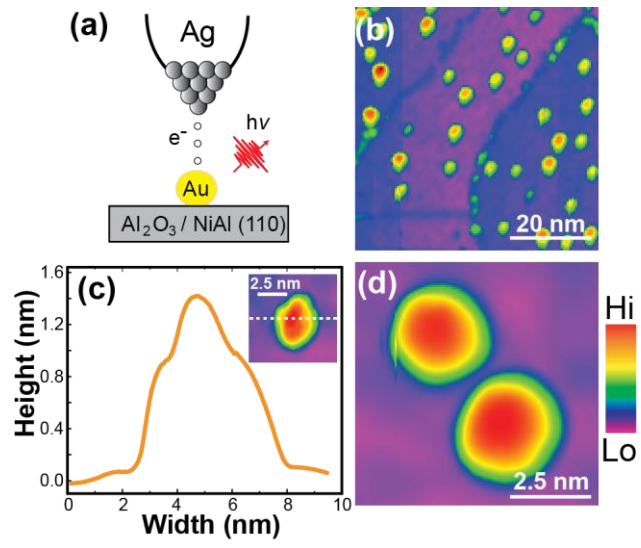


Fig. 3.1

Fig. 3.2 STS spectrum and photon emission for an Au nanocluster. (a) STM topography of an Au nanocluster at $V_B = 3.0$ V, $I_T = 1.0$ nA. (b) Schematic diagram of light emission mechanism. Electrons tunnel inelastically through the nanocluster, losing energy to excitation of the tip-nanocluster-substrate plasmon in the tunnel junction. Decay of the plasmon results in photon emission from junction. Note the voltage drop across oxide layer. (c) dI/dV spectrum recorded over center of nanocluster (green) and Al_2O_3 background (red). Both spectra were recorded with the feedback turned off at set point $V_B = 3.0$ V, $I_T = 1.0$ nA, and ramping bias from 0 to 3.0 V, with lock-in modulation at 341 Hz and $V_{rms} = 10$ mV. Four peaks were observed at energies indicated by the arrows. (d) – (g) dI/dV mapping of the spatial distribution of the intensity at each peak. Each image was recorded pixel by pixel by setting junction at $V_B = 3.0$ V, $I_T = 1.0$ nA, then after disabling the feedback, bias was ramped to the voltage for each peak and dI/dV signal recorded using lock-in technique. (h) Line cut of dI/dV images at 1.6 V (blue curve) and 2.25 V (magenta curve). The cut was performed at the dashed line shown in Fig. 3.2a. (i) Photon emission spectrum over center of the same Au nanocluster showing a broad plasmon peak at 1.7 eV. The junction was set at $V_B = 3.0$ V, $I_T = 12$ nA and the CCD was exposed for 100 s to record the spectrum. (j) Spatially resolved photon mapping of the same Au nanocluster. At each pixel, a photon emission spectrum was taken at $V_B = 3.0$ V, $I_T = 1.0$ nA for 10 s. The energy range in the blue shaded region in (i) was then integrated to obtain the photon intensity at each pixel.

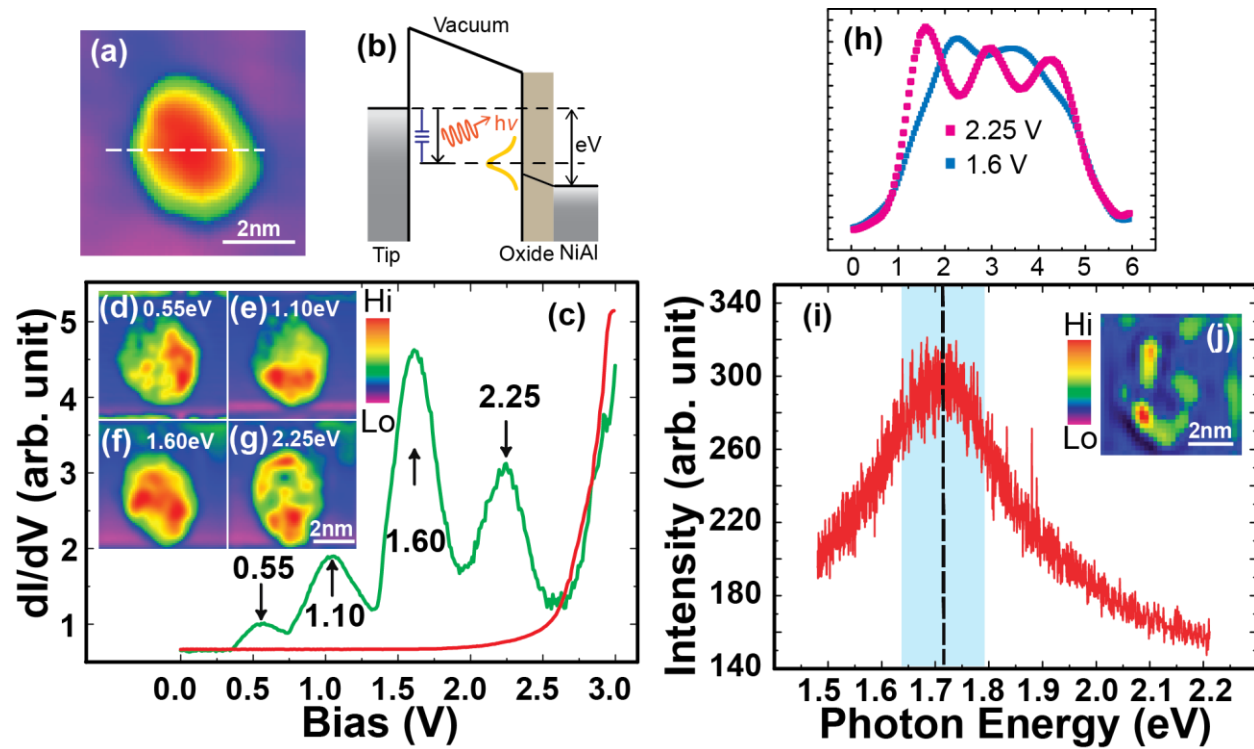


Fig. 3.2

Fig. 3.3 Tunneling electron induced light emission spectra from individual Au nanoclusters of different sizes. (a) Photon emission spectra. Topographic images in (b) – (e) were all taken at set point $V_B = 3.0$ V, $I_T = 1.0$ nA. Photon spectrum for nanocluster in (e) was taken with setpoint $V_B = 3.0$ V, $I_T = 1.5$ nA, exposure time 1000 s. The other spectra, including background were taken with $V_B = 3.0$ V, $I_T = 3.0$ nA, and 1000 s exposure time. The sizes of the nanoclusters, measuring at their largest dimension, were from (b) to (e): 2.4 nm, 2.9 nm, 3.7 nm, and 4.5 nm respectively.

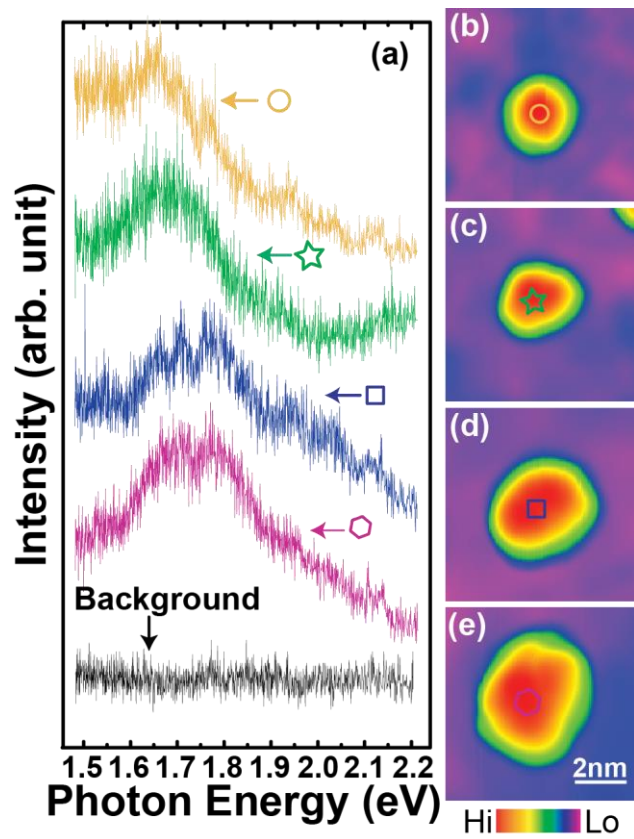


Fig. 3.3

Fig. 3.4 Photon emission from Au nanocluster dimers. (a) Topographic image of Au nanocluster dimer taken at $V_B = 3.0$ V, $I_T = 0.1$ nA. (b) Photon emission image of same dimer. In this image, photon signal was measured at the zeroth order position of the monochromator grating, representing total photon intensity over all wavelengths detected by the CCD. The set point for tunnel junction was $V_B = 3.0$ V, $I_T = 2.0$ nA, with 3 s exposure time at each pixel. (c) Photon emission spectra over another nanocluster dimer (shown in inset). All spectra, including background, measured at $V_B = 3.0$ V, $I_T = 3.0$ nA, 1000 s exposure time. Image at inset scanned at $V_B = 3.0$ V, $I_T = 0.1$ nA.

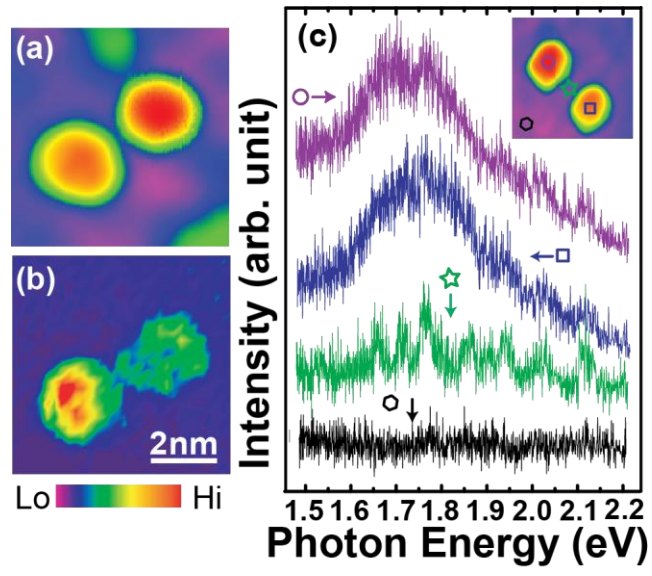


Fig. 3.4

Bibliography

- [1] M. Valden, X. Lai, and W. Goodman, *Science* **281**, 1647 (1998).
- [2] K. Watanabe, D. Menzel, N. Nilius, and H.J. Freund, *Chem. Rev.* **106**, 4301 (2006).
- [3] S. Linic, P. Christopher, and D.B. Ingram, *Nature Mater.* **10**, 911 (2011).
- [4] J.K. Gimzewski, J.K. Sass, R.R. Schlitter, and J. Schott, *Europhys. Lett.* **8**, 435 (1989).
- [5] A. Downes, and M.E. Welland, *Phys. Rev. Lett.* **81**, 1857 (1998).
- [6] N. Nilius, N. Ernst, H.J. Freund, and P. Johansson, *Phys. Rev. B* **61**, 12682 (2000).
- [7] N. Nilius, N. Ernst, and H.J. Freund, *Phys. Rev. Lett.* **84**, 3994 (2000).
- [8] M. Sakurai, and M. Aono, *Phys. Rev. B* **64**, 045402 (2001).
- [9] X.H. Qiu, G.V. Nazin, and W. Ho, *Science* **299**, 542 (2003).
- [10] S.W. Wu, G.V. Nazin, and W. Ho, *Phys. Rev. B* **77**, 205430 (2008).
- [11] C. Chen, P. Chu, C.A. Bobisch, D.L. Mills, and W. Ho, *Phys. Rev. Lett.* **105**, 217402 (2010).
- [12] Y. Zhang, Y. Luo, Y. Zhang, Y.J. Yu, Y.M. Kuang, L. Zhang, Q.S. Meng, Y. Luo, J.L. Yang, Z.C. Dong, and J.G. Hou, *Nature* **531**, 623 (2016).
- [13] P. Johansson, R. Monreal, and P. Apell, *Phys. Rev. B* **42**, 9210 (1990).
- [14] R. Berndt, J.K. Gimzewski, and P. Johansson, *Phys. Rev. Lett.* **67**, 3796 (1991).
- [15] P. Myrach, N. Nilius, and H.J. Freund, *Phys. Rev. B* **83**, 035416 (2011).
- [16] L.R. Madison, M.A. Ratner, and G.C. Schatz, *Prog. Theor. Chem. Phys. A* **29**, 37 (2015).

- [17] B.C. Stipe, M.A. Rezaei, and W. Ho, Rev. Sci. Instr. **70**, 137 (1999).
- [18] T.M. Wallis, N. Nilus, and W. Ho, Phys. Rev. Lett. **89**, 236802 (2002).
- [19] N. Nilus, T.M. Wallis, and W. Ho, J. Phys. Chem. B **109**, 20657 (2005).
- [20] N. Nilus, T.M. Wallis, and W. Ho, Science **297**, 1853 (2002).
- [21] S.W. Wu, G.V. Nazin, X. Chen, X.H. Qiu, and W. Ho, Phys. Rev. Lett. **93**, 236802 (2004).
- [22] G.V. Nazin, S.W. Wu, and W. Ho, Proc. Nat. Acad. Sci. **102**, 8832 (2005).
- [23] C. Chen, C.A. Bobisch, and W. Ho, Science **325**, 981 (2009).
- [24] S. Kühn, U. Håkanson, L. Rogobete, and V. Sandoghdar, Phys. Rev. Lett. **97**, 017402 (2006).
- [25] P.K. Jain, and M.A. El-Sayed, Chem. Phys. Lett. **487**, 153 (2010).
- [26] N. Mirsaleh-Kohan, V. Iberi, P.D. Simmons Jr., N.W. Bigelow, A. Vaschillo, M.M. Rowlands, M.D. Best, S.J. Pennycook, D.J. Masiello, B.S. Guiton, and J.P. Camden, J. Phys. Chem. Lett. **3**, 2303 (2012).
- [27] V. Iberi, N. Mirsaleh-Kohan, and J.P. Camden, J. Phys. Chem. Lett. **4**, 1070 (2013).

Chapter 4

Tunneling Electron Induced Charging and Light Emission of Single Panhematin Molecules*

4.1 Abstract

The charging and tunneling electron induced light emission from single Panhematin (hemin) molecules were studied with the scanning tunneling microscope (STM). Hemin molecules were dosed onto Al₂O₃ thin film grown on NiAl (110) surface. Scanning tunneling spectroscopy (STS) revealed LUMO state at 1.3 V, which formed the SOMO (-0.8 V) and SUMO (2.3 V) states when an electron was injected from the tip into the molecule. Vibronic states were resolved in the light emission spectrum for the charged hemin ion. Analysis of tunneling electron induced light emission spectrum suggests the possibility of hemin to form a doubly charged transient state that facilitates radiative decay into the substrate.

*This chapter by A. Yu, S.W. Li, B. Dhital, H.P. Lu and W. Ho has been published in *J. Phys. Chem. C* under same title. DOI: 10.1021/acs.jpcc.6b04087. Copyright © 2016 by American Chemical Society.

4.2 Article

1. INTRODUCTION

The molecule Panhematin (Hemin) has many applications in the medical and biological sciences. It is an important component in the protein hemoglobin and plays critical roles in chemical processes in the human body. Its electrical and optical properties have attracted considerable attention in the physical sciences as well. Extensive study has been made on its electronic structure and the charge transfer between hemin and semiconductor and metal nanoparticles [1-4]. Its optical properties have been probed by Raman Spectroscopy and photoluminescence [5-7]. Hemin has also garnered interest as a high spin system, as the center iron atom can take up different charge and spin states [8-9]. To date, the majority of the studies had been done in solution, with ensemble averaging to maximize signal to noise ratio. While such studies have yielded considerable results, a more in depth understanding of the mechanisms for electronic and optical processes can be achieved through single-molecule studies.

To study such phenomena at the single molecule level, the scanning tunneling microscope (STM) is an ideal instrument. One notable process to study with the STM is single molecule charging. The STM has the ability to inject single electrons into the orbitals of a molecule adsorbed on a surface. On metal surfaces, the injected electrons readily decay into the substrate due to the strong hybridization between molecule and substrate. If the molecule is adsorbed on insulating layers such as Al_2O_3 , Boron Nitride, or NaCl, the lifetime of the electron in the molecular orbitals is much longer. In some cases, the injected electron can permanently occupy certain orbital and the molecule becomes ionized. Previous studies have shown that both single molecules [10-15] and atoms [16] can be charged by STM. The charging processes are

usually observed as conductance hysteresis during dI/dV measurements. The ultrahigh spatial resolution of the STM allows for precise localization of the charging mechanism [10-11].

Not all of the molecular orbitals can be permanently charged by tunneling electrons. In most cases, the injected electron decays to the substrate through either radiative or non-radiative processes. If the electron lifetime is short, the electron usually releases energy through electron-phonon coupling. However, the electron lifetime of a molecule adsorbed on decoupling layers is sometimes long enough to allow for radiative transition to occur. The injected electron decays through photon emission and the emitted photon can be collected by a spectrally resolved CCD camera. Tunneling electron induced light emission provides another approach to study the interaction between molecular orbital and optical transitions in Sub-Angstrom regime, and have been used to probe the optical transition of single molecules [17-19], artificial nanostructures [20], and intermolecular interactions [21].

Here, we present STS and light emission results for hemin molecules adsorbed on $\text{Al}_2\text{O}_3 / \text{NiAl}$ (110) surface. Tunneling spectroscopy spectrum reveals molecular charging from the tip. Tunneling electron induced light emission spectrum indicates a unique emission mechanism, pointing to the interplay between molecular orbitals and optical processes.

2. EXPERIMENT

The experiment was performed in a home-built low temperature STM, operating at 10 K and base pressure of 3×10^{-11} Torr [22]. The NiAl (110) surface was cleaned by repeated cycles of Ne^+ sputtering and annealing to 1200 K. The Al_2O_3 layer was grown by exposing the NiAl sample to oxygen at 1×10^{-6} Torr for 3 minutes while maintaining sample temperature at 800 K, followed by annealing to 1200 K to crystallize the oxide patches and form mixed oxide and

metal surface. The tip was electro-chemically etched from high purity Ag polycrystalline wires. Bias voltage was applied to the sample with the tip at virtual ground. Hemin molecules were thermally evaporated onto the surface from an alumina crucible. Light emission from the tunnel junction was collected with a lens inside the vacuum chamber and guided to a liquid nitrogen cooled charged couple device (CCD) attached to a monochromator [17].

3. RESULTS AND DISCUSSION

After evaporating onto the surface, hemin molecules can adsorb on both the metal substrate and oxide layer. On the metal surface, it appears as a round protrusion (Fig. 4.1c), unlike magnesium porphyrin (MgP) molecules that we have studied previously. MgP molecules adsorbed on a metal surface appear as four-lobed squared protrusion, showing its structural symmetry [23]. While hemin has similar core structure, its ligands will undoubtedly change the way it interacts with the surface. Its appearance as a spherically symmetric protrusion can be attributed to a stronger interaction with the substrate, as such coupling would delocalize hemin's molecular orbitals, causing them to lose their spatial features.

On the oxide surface, various adsorption geometries are possible. A few of the molecules show a four-lobed structure (Fig. 4.1d) that is much different from their appearance on the metal surface. The absence of features at the center of the molecule indicates that the chlorine atom may have been detached from the molecule during thermal evaporation. STS measurement of the four-lobed hemin molecules shows a reproducible hysteresis during forward and backward bias scans, signaling the molecule undergoes charging and discharging by tunneling electrons (Fig. 4.2a). As the bias voltage is ramped up with the feedback off (Fig. 4.2a, black curve), a peak corresponding to the lowest unoccupied molecular orbital (LUMO) of hemin appears at 1.3 V. If

the bias ramp is continued, a charging event can be observed by a sudden jump in the dI/dV curve at 2.1 V. The extra electron is injected into the LUMO of hemin, creating two new molecular states. The spin degenerate LUMO state splits into the singly occupied and unoccupied molecular orbitals (SOMO and SUMO). The charging and discharging energy diagrams are illustrated in Fig. 4.2d-e. In the STS scan, the SUMO is observed as a peak at 2.3 V, while the SOMO can be seen starting at -0.8 V, before the molecule discharges at -1.03 V. Such spectroscopic line shape can be assigned to the charging and discharging events as in MgP [10-12, 14].

The effect of charging can be visualized by topographic images of the charged and uncharged molecules (Fig. 4.2b and 4.2c). The images over same scan size and same set point show the charged molecule appears smaller in size. An interesting question that the charging spectrum raises is where the injected electron resides. Previous study of MgP showed that the electron is injected into the π orbital around the rings during its ionization process, as evidence from the low charging probability at the center of the molecule [10]. In the case of hemin, the central Fe ion commonly serves as an electron acceptor during chemical reactions [24]. Our experiment shows that the charging probability and voltage threshold are relatively uniform across the hemin molecule, indicating that both Fe and outer rings are involved in the charging process.

The anion hemin is stable away from the discharging threshold at negative bias, which allows us to probe its optical properties through tunneling electron induced light emission with positive bias higher than the charging threshold (Fig. 4.3). Fig. 4.3a shows the photon emission spectrum from the same hemin molecule on Al_2O_3 when excited by tunneling electrons at a set point of $V_B = 2.5$ V, $I_T = 1.0$ nA (Green curve). The spectrum reveals multiple peaks enveloped

by a broader peak. Using multi-peak Lorentzian fit, we find the peak positions at energies of 1.77 eV, 1.87 eV, 1.94 eV, 2.02 eV, and 2.18 eV. The light emission is markedly different when electron tunneling occurs over the oxide and the metal substrate. At the same set point, there is significantly reduced light emission from the Al₂O₃. On the NiAl (110) surface, there is strong and broad plasmon emission center around 2.2 eV (Fig. 4.3b). The intensity of plasmon emission over the metal surface is much stronger than molecular emission. Even at 1/6 the exposure time (100 s), the photon emission intensity is roughly 33% larger.

Analysis of the light emission spectra from hemin and the NiAl (110) surface leads us to propose two mechanisms for the light emission. The first is an inelastic electron tunneling (IET) process, in which the tunneling electron loses energy to a plasmon excitation in the junction, and release a photon in the decay process (Fig. 4.3d). The plasmon can also decay into electron-hole pairs that can undergo radiative decay. The broad width of the plasmon emission peak can be attributed to the short lifetime of excited plasmons. These processes provide a mechanism for light emission from the metal substrate.

For the emission from the hemin molecule, the narrower peaks suggest an emission mechanism involving transition of molecular vibronic states. In this process, the electron first tunnels into an excited vibrational state of the SUMO created by the charging event. Light emission results from the decay of the electron from various vibronic states of the molecule to states near the Fermi level of the substrate (Fig. 4.3e). Fitting the multiple emission peaks observed with a linear function, we find slope to be 97 mV, representing the energy spacing between successive vibrational states (Fig. 4.3c). Consulting previous experiments on metalloporphyrins, the vibronic state energy can be assigned to the in-plane A_{1g} mode of hemin [25-26].

To better visualize the connection between light emission and the vibronic states, the dI/dV spectrum of the SUMO is overlaid with the light emission spectrum over same energy range (Fig. 4.3a, magenta curve). The overlap shows that light emission peaks occur in the same energy range as the SUMO. It should be noted that due to voltage drop across the oxide, the applied voltage will not line up with the photon energy as indicated in Fig. 4.3a. The effective voltage should be downshifted, the exact value depending on tip-sample distance as well as work function difference between tip and substrate. Nevertheless, the effect should be approximately 1/7 to 1/8 of the applied voltage [27], which still makes SUMO overlap with the vibronic transitions. The overlap suggests light emission arises from electron transition from the vibronic states to the substrate, because there are no molecular orbitals, as shown in the dI/dV spectrum in Fig. 4.2a, with suitable energy difference from the SUMO that equals to the emitted light energy. Most notably, there is no molecular orbital near and below the Fermi level, which could be pulled to the positive side at high bias and become the final state in an intramolecular transition [19].

Such an emission mechanism is different from previous experiments with porphyrin molecules on insulating surfaces, where molecular fluorescence occurs with transition between two molecular orbitals [17-19]. Further analysis shows that the dI/dV spectrum for emitting MgP molecules did not contain charging behavior [18]. While the MgP became charged in a transient state during the electron tunneling and emission process, it does not retain the charge permanently. For those MgP that are already in stable charged state, no light emission is reported [19], implying its inability to form a doubly charged transient state. In contrast to MgP, hemin has shown both stable anion state and molecular emission, suggesting that it is possible for hemin to be in a doubly charged transient state. The central Fe atom is likely responsible for the

extra electron, given its ability to change oxidation state between +2 and +3. Our results here demonstrated the distinct characteristics of hemin and the interplay between molecular charging and optical emission.

4. CONCLUSIONS

In conclusion, we have demonstrated the charging and light emission of single hemin molecules adsorbed on thin alumina layer grown on NiAl (110) surface. While the dI/dV spectrum shows comparable features to charging events in MgP experiments, the light emission results show a distinct emission mechanism. Analysis of charging and light emission spectra reveals that the emission comes from decay of vibronic states directly to the substrate, possibly due to the ability of hemin to form doubly charged transient state.

Fig. 4.1 STM topography of panhematin (hemin) molecules. (a) Schematic of experimental setup. Hemin molecules were deposited on Al_2O_3 surface at 10 K, and light emission was induced by tunneling electrons. (b) Molecular structure of hemin. (c) STM constant current topographic image of three hemin molecules on NiAl (110) metal surface. Hemin molecules appeared as round protrusions. Scan was taken at $V_B = 2.0$ V, $I_T = 0.1$ nA. (d) Constant current image of one hemin on Al_2O_3 surface. Scan taken at $V_B = 1.7$ V, $I_T = 0.1$ nA. Note the larger scan range than in (c).

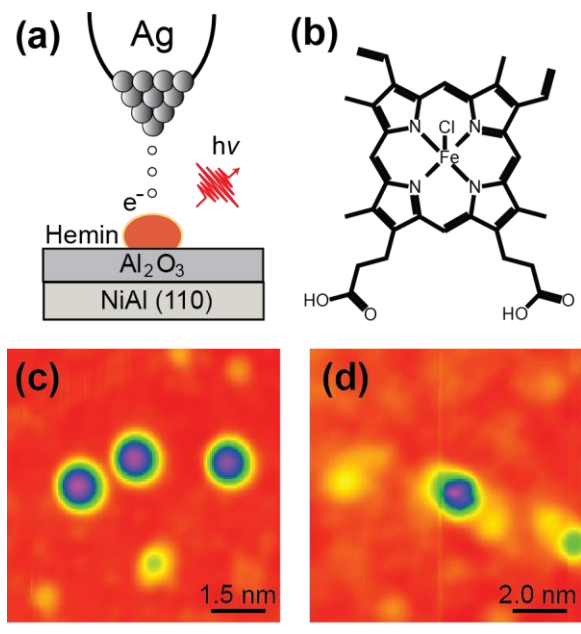


Figure 1

Fig. 4.2 Charging of hemin molecules. (a) dI/dV spectrum of hemin molecule on oxide surface. The black (red) curve represents spectrum taken by ramping bias in the forward (backward) direction. As bias was ramped up, a peak at 1.3 V representing the LUMO of the molecule was observed. At 2.1 V, a sudden rise in dI/dV signal indicates charging of molecule. As the bias was ramped down, the molecule was discharged at -1.03 V. Spectrum was taken at center of molecule, with junction set at $V_B = 2.6$ V, $I_T = 0.1$ nA, from -2.0 V to 2.5 V. Lock-in modulation was applied at 361 Hz at 10 mV RMS. Constant current topographic images of the neutral (b) and charged (c) molecule are included in the inset. Both images taken at $V_B = 1.5$ V, $I_T = 0.1$ nA (d) – (e) Energy diagrams showing the charging (d) and discharging (e) of hemin molecule. Electron is injected into LUMO at positive bias, forming singly occupied (SOMO) and singly unoccupied (SUMO) states. Electron is ejected from SOMO at negative bias. The dashed curve represents the extrapolated SOMO state.

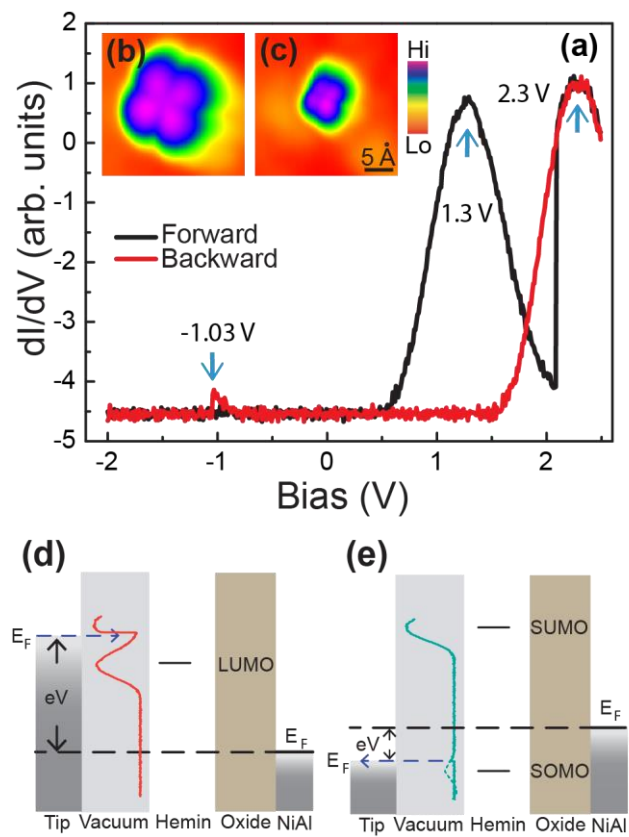


Figure 2

Fig. 4.3 Light emission from hemin molecules. (a) Photon emission spectrum (green curve) collected over center of same hemin molecule as in Fig. 4.2. Tunnel junction was set at $V_B = 2.5$ V, $I_T = 1$ nA, with the CCD exposed for 10 mins. The dI/dV spectrum (magenta curve) of same molecule over same energy range taken after charging is overlaid on top. The backward scan was chosen to show the SUMO peak. Emission peaks from vibronic transitions are shown based on multi-peak Lorentzian fit. The energy positions are 1.77 eV, 1.87 eV, 1.94 eV, 2.02 eV, and 2.18 eV. (b) Light emission spectra from the NiAl (110) substrate (green curve) and Al_2O_3 layer (grey curve). Both spectra were taken with same set point as in (a). CCD was exposed for 100 s for NiAl (110) and 10 mins for Al_2O_3 . (c) Linear fit of vibronic energy. The successive vibronic peaks are plotted to determine the vibration quanta. (d) – (e) Schematic diagrams of light emission mechanisms on substrate (d) and over hemin molecule (e). Over metal substrate, light emission occurs through inelastic electron tunneling (IET) process, exciting a plasmon in the junction. Over hemin, emission mechanism involves intramolecular radiative transitions between molecular vibronic states.

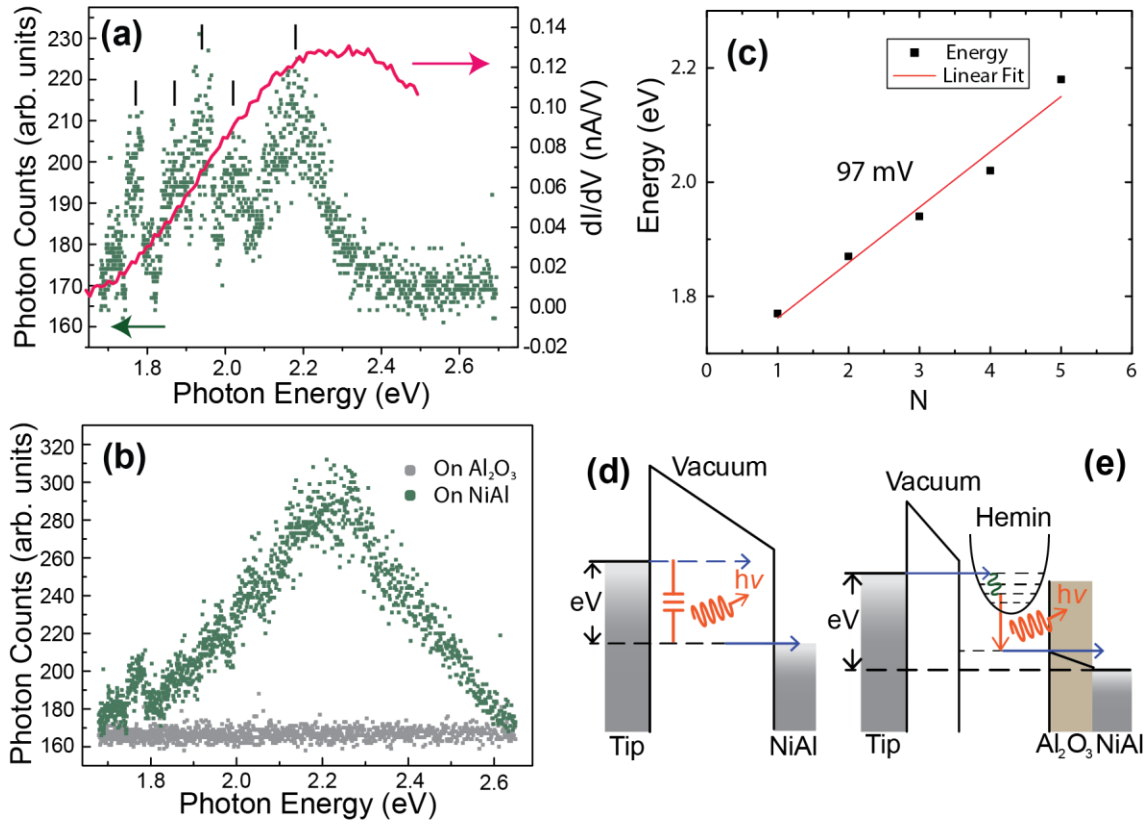


Figure 3

Bibliography

- [1] O.P. Charkin, N.M. Klimenko, D.O. Charkin, H.C. Chang, and S.H. Lin, *J. Phys. Chem. A* **111**, 9207 (2007).
- [2] A. Staniszewski, A.J. Morris, T. Ito, and G.J. Meyer, *J. Phys. Chem. B* **111**, 6822 (2007).
- [3] M. Nakamura, Y. Ohgo, and A. Ikezaki, *J. Inorg. Biochem.* **102** 433 (2008).
- [4] Y. Wang, P.C. Sevinc, Y.F. He, and H.P. Lu, *J. Am. Chem. Soc.* **133**, 6989 (2011).
- [5] T.G. Spiro, and T.C. Streckas, *J. Am. Chem. Soc.* **96**, 338 (1974).
- [6] E. Podstawka, C. Rajani, J.R. Kincaid, and L.M. Proniewicz, *Biopolymers* **57**, 201 (2000).
- [7] B.R. Wood, S.J. Langford, B.M. Cooke, J. Lim, F.K. Glenister, M. Duriska, J.K. Unthank, and D. McNaughton, *J. Am. Chem. Soc.* **126**, 9233 (2004).
- [8] R.J. Kurland, R.G. Little, D.G. Davis, and C. Ho, *Biochemistry* **10**, 2237 (1971).
- [9] S. Yoshida, T. Iizuka, T. Nozawa, and M. Hatano, *Biochem. et Biophys. Act.* **405**, 122 (1975).
- [10] S.W. Wu, N. Ogawa, and W. Ho, *Science* **312**, 1362 (2006).
- [11] S.W. Wu, N. Ogawa, G.V. Nazin, and W. Ho, *J. Phys. Chem. Lett. C* **112**, 5241 (2008).
- [12] U. Ham, and W. Ho, *Phys. Rev. Lett.* **108**, 106803 (2012).
- [13] L.W. Liu, T. Dienel, R. Widmer, and O. Gröning, *ACS Nano* **10**, 10125 (2015).

- [14] S.W. Li, D.W. Yuan, A. Yu, G. Czap, R.Q. Wu, and W. Ho, Phys. Rev. Lett. **114**, 206101 (2015).
- [15] C. Wagner, M.F.B. Green, P. Leinen, T. Deilmann, P. Krüger, M. Rohlfing, R. Temirov, and F.S. Tautz, Phys. Rev. Lett. **115**, 026101 (2015).
- [16] J. Repp, G. Meyer, F.E. Olsson, and M. Persson, Science **305**, 493 (2004).
- [17] X.H. Qiu, G.V. Nazin, and W. Ho, Science **299**, 542 (2003).
- [18] S.W. Wu, G.V. Nazin, and W. Ho, Phys. Rev. B **77**, 205430 (2008).
- [19] C. Chen, P. Chu, C.A. Bobisch, D.L. Mills, and W. Ho, Phys. Rev. Lett. **105**, 217402 (2010).
- [20] C. Chen, C.A. Bobisch, and W. Ho, Science **325**, 981 (2009).
- [21] Y. Zhang, Y. Luo, Y. Zhang, Y.J. Yu, Y.M. Kuang, L. Zhang, Q.S. Meng, Y. Luo, J.L. Yang, Z.C. Dong, and J.G. Hou, Nature **531**, 623 (2016).
- [22] B.C. Stipe, M.A. Rezaei, and W. Ho, Rev. Sci. Instr. **70**, 137 (1999).
- [23] A. Yu, S.W. Li, G. Czap, and W. Ho, J. Phys. Chem. C **119**, 14737 (2015).
- [24] T. Ohno, D. Haga, K. Fujihara, K. Kaizaki, and M. Matsumura, J. Phys. Chem. B **101**, 6415 (1997).
- [25] S. Choi, and T.G. Spiro, J. Am. Chem. Soc. **105**, 3683 (1983).
- [26] M. Abe, T. Kitagawa, and Y. Kyogoku, J. Chem. Phys. **69**, 4526 (1978).
- [27] S.W. Wu, G.V. Nazin, X. Chen, X.H. Qiu, and W. Ho, Phys. Rev. Lett. **93**, 236802 (2004).

Chapter 5

Visualization of Nano-Plasmonic Coupling to Molecular Orbital in Light Emission Induced by Tunneling Electrons*

5.1 Abstract

The coupling between localized plasmon and molecular orbital in the light emission from a metallic nanocavity has been directly detected and imaged with sub-0.1 nm resolution. The light emission intensity was enhanced when the energy difference between the tunneling electrons and the lowest unoccupied molecular orbital (LUMO) of an azulene molecule matches the energy of a plasmon mode of the nanocavity defined by the Ag-tip and Ag(110) substrate of a scanning tunneling microscope (STM). The spatially resolved image of the light emission intensity matches the spatial distribution of the LUMO. Our results highlight the near-field coupling of a molecular orbital to the radiative decay of a plasmonic excitation in a confined nanoscale junction.

*This chapter by A. Yu, S.W. Li, and W. Ho has been prepared for submission to *Phys. Rev. Lett.* under same title.

5.2 Article

Azulene has been the subject of many studies in photochemistry due to its interesting optical properties. Most notably, the molecule fluoresces from the S_2 state, instead of the usual S_1 state [1]. This violation of Kasha's rule [2] made it one of few unique molecules and has resulted in numerous studies to understand the origin of the deviation [3-5]. Though extensively studied in the gas phase, the electronic and optical properties of azulene when adsorbed on surfaces are not well known [6-8]. Earlier studies with scanning tunneling microscopy (STM) achieved low resolution images of azulene on metal surfaces, but sufficient to enable the differentiation from naphthalene [9-10]. Detailed imaging of molecular structure and electronic orbitals remain unrealized.

The scanning tunneling microscope (STM) is an ideal instrument for the study of molecular properties and interactions at the single molecule level. It can act as a localized electron source, allowing for the coupling of tunneling electrons to molecular orbitals, surface plasmons, and inducing light emission. Due to its ability to precisely position the tip, these properties and interactions can be probed with the same sub-Ångström spatial resolution. Previous experiments have demonstrated STM's ability to induced photon emission with atomic scale resolution from metallic nanoclusters [11] or molecules [12-14] adsorbed on a thin oxide layer grown on a metallic substrate. Here we gained insight into the electronic and optical properties of azulene on Ag (110) surface without a thin isolation layer. We imaged the LUMO of azulene with scanning tunneling spectroscopy (STS). Plasmon induced light emission from azulene was also studied with a spectrally resolved CCD. Photon imaging of single azulene molecule showed spatial dependence resembling LUMO, indicating coupling of the plasmon mode to the molecular orbital.

The experiment was conducted in a home built STM with a background pressure of 3×10^{-11} Torr [15]. The Ag (110) surface was cleaned through repeated cycles of Ne^+ sputtering and annealing to 700 K. The tip was electro-chemically etched from high purity Ag wires. Bias is applied to the sample with tip at virtual ground. Light emission from the tunnel junction was collected with a lens inside the vacuum chamber and guided to a spectrograph equipped with a liquid nitrogen cooled charged couple device (CCD) [12-14]. Room temperature azulene molecules were dosed *in situ* onto the surface through a variable leak valve, using its vapor pressure at room temperature of 1×10^{-4} Torr. Carbon monoxide molecules were also co-adsorbed on the surface to allow for more detailed structural imaging with a CO-terminated tip.

Upon sublimation onto the surface, azulene molecules appear as pear shaped protrusions in constant current topography (Fig. 1a, 1b). Images show there are two equivalent adsorption geometries on the Ag (110) surface, as shown in Fig. 1a, both with the axis of the molecule perpendicular to the $[1\bar{1}0]$ direction. To determine the adsorption geometry more precisely, topographic images were taken with a CO-terminated tip, showing the atomic structure of the Ag lattice (Fig. 1c) as well as more detailed structure of azulene. At the set point of 30 mV, 2.8 nA, images taken with the CO-tip can resolve the five and seven-member carbon rings (Fig. 1d), leading to the adsorption geometry of azulene on the Ag(110) lattice (Fig 1f). Each molecule straddles two Ag rows, with the center of the carbon rings near the short bridge site along $[1\bar{1}0]$.

The electronic structure of azulene was obtained from dI/dV spectra recorded over various points of the molecule, as displayed in Fig. 2 for adsorption with the five-member carbon ring at the top. A small bump at 0.6 V is observed in the dI/dV spectrum, indicating the presence of a localized electronic state (Fig. 2a). The intensity of the electronic peak exhibits spatial variations; the peak is more pronounced at the top and sides and weaker at the center and bottom.

The spatial dependence of the electronic state is visualized with dI/dV imaging at different biases (Fig 2c-e). Each image is composed of the dI/dV signal at each pixel, obtained with the lock-in technique and represents an intensity map at the chosen voltage. Comparison of the dI/dV images with calculated LUMO orbital of azulene from the literature shows striking similarity. The dI/dV images confirmed the origin of the electronic peak as stemming from the LUMO of azulene. In most cases where a molecule is adsorbed on a metal substrate, interaction between the molecule and substrate tend to delocalize the molecular orbitals due to mixing with substrate electronic states, causing them to lose their spatially confined features [18]. The fact that the LUMO can be imaged by tunneling spectroscopy indicates a relatively weak interaction between the azulene and substrate.

The electronic state of azulene can strongly couple with the plasmon modes of the STM nano-junction. This coupling can be probed by tunneling electron induced light emission. The light emission spectra taken on the metal substrate and over the center of an azulene molecule are shown in Fig. 3a, with the tunneling gap set at $V_B = 2.5$ V, $I_T = 1.0$ nA. On the Ag (110) surface, the emission spectrum features a broad and strong peak center around 2.2 eV with several lower energy peaks. The onset of the light emission occurs at 1.5 eV, just below the scale of the graph. The emission spectrum is attributed to the radiative decay of plasmon modes of the tip-substrate nanocavity [19]. A similar spectrum is recorded over the azulene molecule. However, the emission from the plasmon mode center around 2.2 eV is enhanced. This enhancement effect is observed for all azulene molecules we have examined. To understand the origin of such light emission enhancement, we have studied the bias dependence of the light emission. On both the Ag (110) surface and azulene, we see the onset of light emission at 1.6 eV. As the bias increases, the enhancement of photon emission over the azulene is observed for bias higher than 2.1 V (Fig.

3b). We attribute the photon intensity increase on azulene to interaction between azulene and surface plasmon on the Ag(110) substrate.

In tunneling electron induced light emission on metal surfaces, the emission mechanism involves the inelastic electron tunneling (IET) process. The tunneling electron gives up energy equal to a surface plasmon resonance (SPR) mode of the substrate, and photon emission occurs as a result of the decay of the plasmon. In the presence of a molecule, the molecular orbital can serve as the final state for the inelastic tunneling process (Fig. 4a). The lack of features corresponding to molecular fluorescence in our light emission spectrum for azulene implies that the IET process is the only emission mechanism. When the tip is placed over the azulene, the presence of the molecular orbitals provides another channel for the electrons to tunnel inelastically, enhancing the amplitude of the SPR excitation and the associated light emission. In order for a molecular orbital to effectively couple to the SPR, the energy of the plasmon excitation have to match the energy difference between the molecular orbital and bias voltage. From the STS data (Fig. 2a), the LUMO of azulene occurs at around 0.6 eV. The width of the dI/dV peak and imaging (Fig. 2c-e) suggest the LUMO extends in energy from 0.4 eV to 1.0 eV. At the bias voltage of 2.5 V, the energy difference between the tunneling electron and molecular orbital ranges from 1.5 eV to 2.1 eV, spanning the width of the LUMO peak. The onset of the SPR starts at around 1.6 eV from the light emission spectrum (Fig. 3b). When the energy difference between the bias voltage and plasmon mode matches the energy of the azulene orbital, the SPR is coupled to the azulene LUMO, accounting for the observed threshold for the enhancement of photon emission intensity at $V_B = 2.1$ V.

To visualize the electron – plasmon – photon interactions in azulene, photon emission imaging was performed at various bias voltages (Fig. 4b – 4d). For each image, a photon

emission spectrum was recorded at each pixel, and the spectrum was integrated to yield the total photon intensity at that pixel. The images give a visual depiction of the interactions. At a set point of $V_B = 2.0$ V, $I_T = 1.0$ nA, the photon image shows almost no spatial variation (Fig. 4b), as expected from the bias dependence curve in Fig. 3b. The enhancement effect from azulene does not occur until V_B reaches 2.1 V. As we raise the bias to 2.25 V, three faint lobes can be observed in Fig. 4c, which become more prominent at $V_B = 2.5$ V (Fig. 4d). Comparing the photon emission with dI/dV (Fig. 2d) images, we see the resemblance for the two different adsorption types. The similarity is a direct consequence of the interaction between SPR, LUMO of azulene, and the emitted photon. At $V_B = 2.0$ V, the energy difference between the bias voltage and azulene LUMO does not match the SPR, hence no emission enhancement is observed. When enhancement occurs at higher biases, the spatial dependence of the photon emission image will resemble the spatial dependence of the electronic state, separated in energy by a plasmon (Fig. 4c vs. Fig. 2c, and Fig. 4d vs. Fig. 2d). The photon images demonstrate the prominent role the azulene LUMO plays in the electron – plasmon – photon interaction.

In summary, we have studied the electrical and optical properties of azulene adsorbed on the Ag (110) surface. The LUMO state of azulene was visualized through STS imaging at, which can strongly couple with the tunneling electron induced plasmon excitation processes. The tunneling electron induced light emission spectrum from azulene shows the selective enhancement of the plasmon mode with an energy matching the difference between the injected electron and the azulene LUMO. Spatially resolved images of light emission show clear resemblance to azulene LUMO, confirming its role as the final state in the plasmon mediated inelastic tunneling process. Our results showcase the unique optical properties of azulene and the

ability of the STM to resolve and investigate electronic and optical interactions at the single molecule level.

Fig. 5.1 STM constant current topography of azulene on Ag (110). (a) Image showing two possible types of adsorbed azulene. (b) Zoom in view of one type. Tunnel junction was set at $V_B = 1$ V, $I_T = 0.1$ nA in (a) and $V_B = 1$ V, $I_T = 1$ nA in (b). A co-adsorbed CO molecule is seen in upper right corner of (a). (c-d) Constant current images with CO-terminated tip. The Ag lattice is resolved in (c). Scaled molecular skeleton of azulene is generated by ChemDraw with calculated bond lengths [16] and overlaid onto CO-tip image in (d). Tunnel junction was set at $V_B = 30$ mV, $I_T = 3$ nA in (c) and $V_B = 30$ mV, $I_T = 2.8$ nA in (d). (e) Schematic diagram of optical experiment. Light emission arises from decay of surface plasmon resonance (SPR) excited by tunneling electrons. (f) Adsorption geometry of one type of azulene. Scaled model of azulene and Ag lattice was generated based on CO-tip images in (c) and (d).

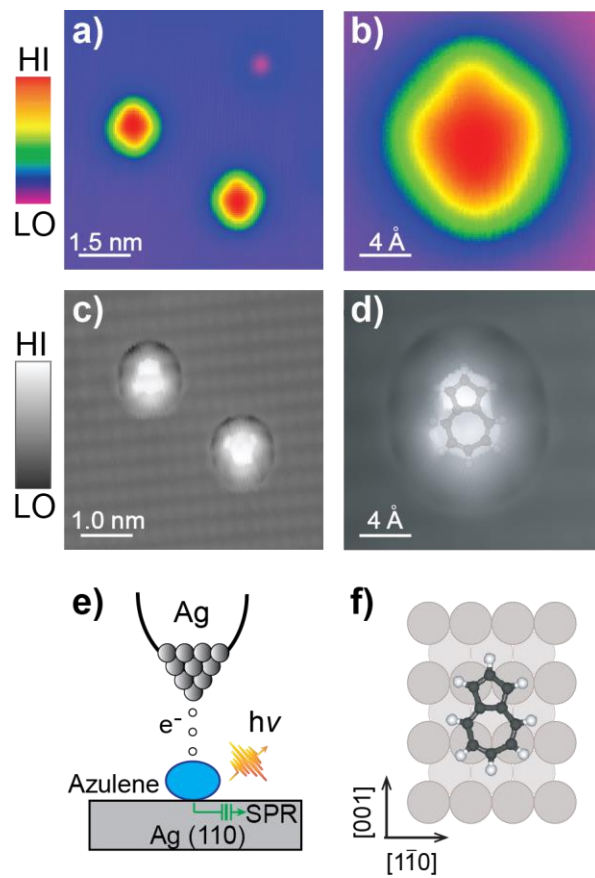


Fig. 1

Fig. 5.2 Scanning tunneling spectroscopy (STS) of azulene electronic states. (a) dI/dV spectra measured over different points of the azulene molecule, as indicated in inset. A bump in dI/dV is observed around 0.6 V, attributed to LUMO state of azulene. All spectra were taken with tunnel junction set at $V_B = 1.0$ V, $I_T = 1.0$ nA, lock-in modulation at 345 Hz with and 10 mV rms. (b) Calculated LUMO of azulene [17]. (c-e) dI/dV images at different voltages. For each image, tunnel junction was set at $V_B = 1.0$ V, $I_T = 1.0$ nA at each pixel, then with feedback disabled, bias was ramped to the selected voltage, and dI/dV signal was monitored with lock-in amplifier. The images give spatial distribution of the dI/dV signal at the selected voltages.

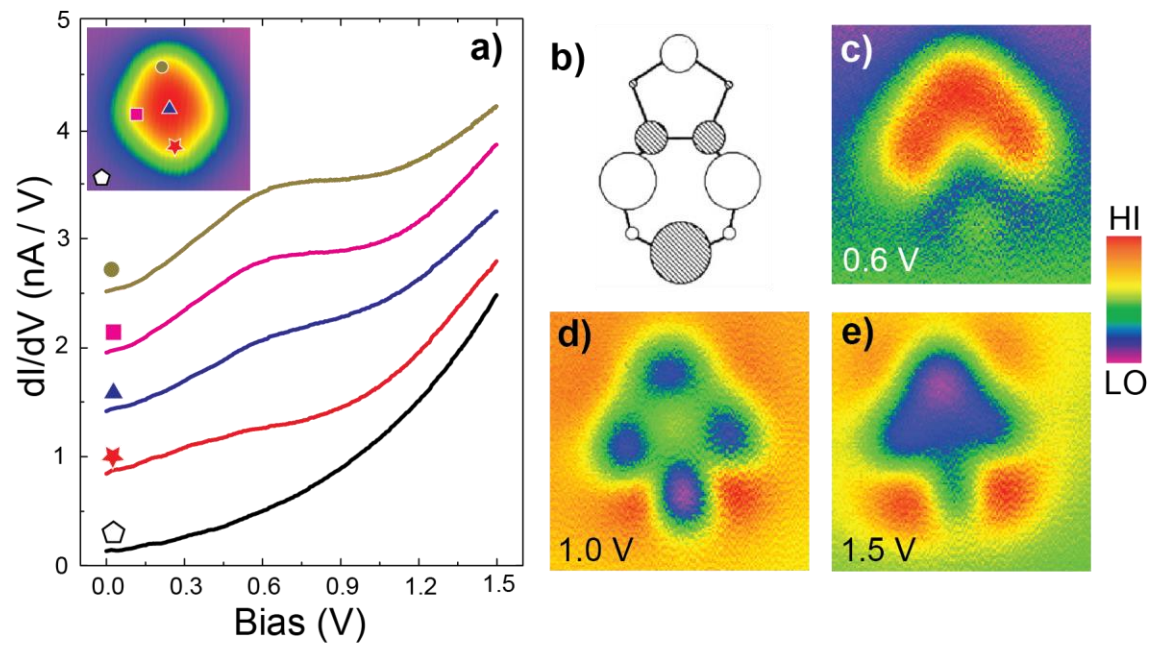


Fig. 2

Fig. 5.3 Tunneling electron induced light emission from azulene. (a) Light emission spectrum taken over Ag (110) (blue curve) and center of azulene (red curve). Tunnel junction was set at $V_B = 2.5$ V and $I_T = 1.0$ nA, and the nitrogen cooled CCD was exposed for 1000 s in both spectra. (b) Bias dependent photon emission spectrum from Ag (110) (blue curve) and azulene (red curve). To generate each curve, light emission was recorded as a function of the bias voltage and at the zeroth order of the monochromator, representing the total emission intensity for that voltage.

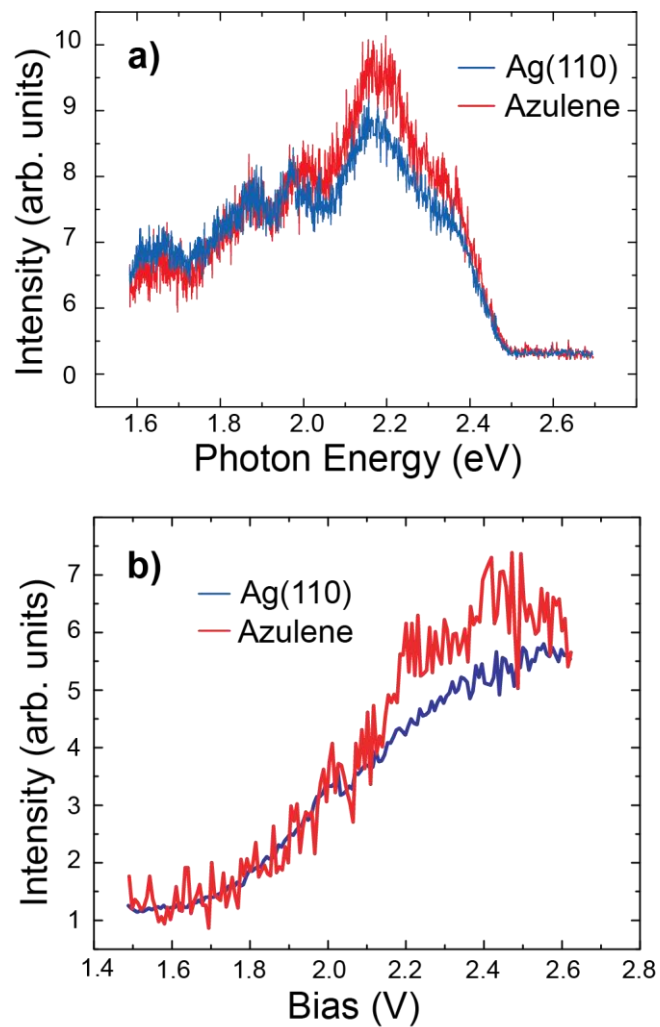


Fig. 3

Fig. 5.4 Photon emission imaging with the STM. (a) Schematic diagram of the light emission mechanism. Electrons tunnel inelastically by exciting a surface plasmon resonance (SPR). A molecular orbital, such as LUMO of azulene, can serve as the final state in the inelastic tunneling process. (b-d) Photon emission image at $I_T = 1.0$ nA but different bias voltages as noted. Each image is generated by recording the zeroth order light emission spectrum at each pixel, then integrating to obtain total photon intensity at that pixel. CCD was exposed for 3 s at each pixel. Images in (c) and (d) show resemblance to dI/dV images of the LUMO of azulene.

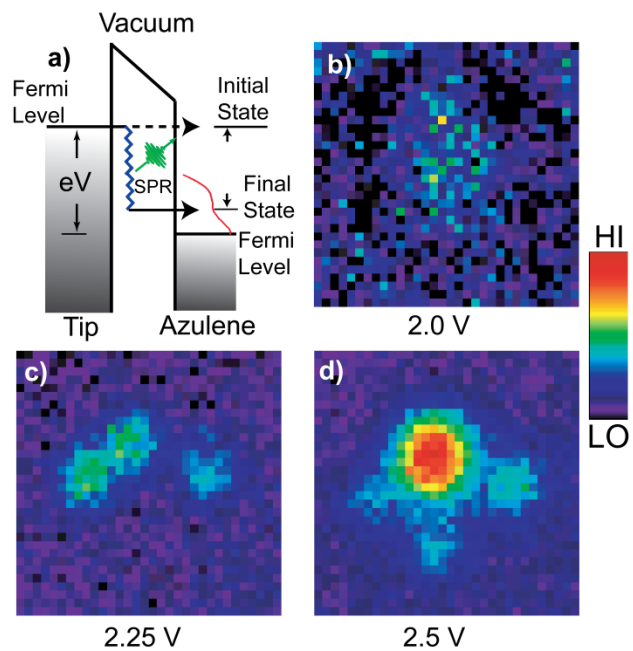


Fig. 4

Bibliography

- [1] M. Beer and H.C. Longuet-Higgins, *J. Chem. Phys.* **23**, 1390 (1955).
- [2] M. Kasha, *Discuss. Faraday Soc.* **9**, 14 (1950).
- [3] A.J. Wurzer, T. Wilhelm, J. Piel, E. Riedle, *Chem. Phys. Lett.* **299**, 296 (1999).
- [4] Y. Amatatsu and Y. Komura, *J. Chem. Phys.* **125**, 174311 (2006).
- [5] Y. Semba, K. Yoshida, S. Kasahara, C.K. Ni, Y.C. Hsu, S.H. Lin, Y. Ohshima, and M. Baba, *J. Chem. Phys.* **131**, 024303 (2009).
- [6] D. Dahlgren and J.C. Hemminger, *Surface Science* **144**, 459 (1982).
- [7] M.F. Lin, C.L. Huang, Y. T. Lee, and C.K. Ni, *J. Chem. Phys.* **119**, 4 (2003).
- [8] M. Barybin, *Coordination Chem. Rev.* **254**, 1240 (2010).
- [9] V.M. Hallmark and S.Chiang, *Phys. Rev. Lett.* **70**, 3740 (1993).
- [10] S. Chiang and V. M. Hallmark, *J. Vac. Sci. Technol. B* **12**, 3 (1994).
- [11] N. Nilius, N. Ernst, and H.J. Freund, *Phys. Rev. Lett.* **84**, 3994 (2000).
- [12] X.H. Qiu, G.V. Nazin, and W. Ho, *Science* **299**, 542 (2003).
- [13] S.W. Wu, G.V. Nazin and W. Ho, *Phys. Rev. B* **77**, 205430 (2008).
- [14] C. Chen, P. Chu, C.A. Bobisch, D.L. Mills, and W. Ho, *Phys. Rev. Lett.* **105**, 217402 (2010).
- [15] B. C. Stipe, M. A. Rezaei, and W. Ho, *Rev. Sci. Instrum.* **70**, 137, (1999).
- [16] T. Okazaki and K.K. Laali, *Org. Biomol. Chem.* **1**, 3078 (2003).

[17] D.M. Lemal and G.D. Goldman, J. Chem. Edu. **65**, 923 (1988).

[18] X.H. Qiu, G.V. Nazin, and W. Ho, Phys. Rev. Letts. **92**, 206102 (2004).

[19] Z.C. Dong, X.L. Zhang, H.Y. Gao, Y. Luo, C. Zhang, L.G. Chen, R. Zhang, X. Tao, Y. Zhang, J.L. Yang, and J.G. Hou, Nature Photonics **4**, 50 (2010).

Chapter 6

Concluding Remarks and Future Prospects

6.1 Concluding Remarks

This dissertation discussed several experiments done to expand the capability of the STM. A novel imaging technique, taking advantage of the rotational transition of H_2 , was developed and used to image MgP molecules on Au (110) surface. The resulting images gave insight to the nature of the interaction between H_2 and the different chemical components of MgP. The optical experiments allowed us to visualize the interaction between tunnel junction plasmon and electrons from nanocluster states and molecular orbitals. These results demonstrated the utility and versatility of STM light emission.

The successful implementation of hydrogen rotational imaging allows for future application of the technique to other molecules. The key ingredient is the interaction between H_2 and the underlying molecule. By monitoring the response of vibrational and rotational energies of H_2 to the local chemical environment, fundamental features of the interactions can be visualized. The different ways the H_2 can interact with its chemical environment give the method versatility and flexibility to examine different molecules.

In our experiment, the main interaction between H_2 and the MgP is electrostatic. The image contrast in our H_2 results from the H_2 reacting to the electrostatic potential posed by the MgP. Since H_2 can be a charge donor [1-2], the presence of highly electro-negative atoms such as nitrogen will preferentially trap the H_2 . This also means that H_2 can interact with molecular orbitals, something that is worth investigating.

Optical sensitivity of the STM is exhibited in this dissertation through the study of tunneling electron induced light emission. The light collected in the far field can give insight to the plasmonic interactions in the tunnel junction. The STM provides a means of localized excitation of junction plasmon mode and photon emission imaging gives a way to visualize the excitation probability with sub-Angström spatial resolution.

The interaction between junction plasmon and Au nanoclusters were visualized through the study of light emission from the tunneling junction. The nanoclusters exhibit quantum confined electronic states in two dimensions. While earlier experiments demonstrated particle-in-a-box like states in one-dimensional metal chains, the extension of these states to two dimensions have not been widely reported [3-4]. Our experiment demonstrated the coupling of two dimensional nanocluster electronic states to the tip-nanocluster junction plasmon through photon emission imaging. The interaction is further highlighted through light emission from nanoclusters of different sizes and dimers.

Our experiments on hemin and azulene molecules further demonstrate the value of optically sensitive STM techniques. In previous studies of molecular light emission, the main emission mechanism involves transition to a molecular orbital as the final state [5-7]. Our experiment on hemin show that optical transition can also occur where the final state is the substrate states near the Fermi level. Such a transition showcases the unique interplay between the hemin vibronic states and the tunnel junction plasmon.

It should be noted that optical transitions from vibronic states are only possible if the molecule is isolated through an insulating layer. The presence of the insulating layer like Al_2O_3 lengthens the lifetime of the tunneling electron in the molecule, allowing for optical transition to

occur. Intermixing of molecular and substrate electronic states tend to smear the molecular orbitals and quench light emission [8].

For this reason, our results on azulene are surprising. The interaction between azulene and the Ag surface is weak enough such that we were able to image the LUMO with STS. The LUMO also lies at the right energy such that inelastic tunneling from the tip to excite a junction plasmon can also tunnel into the LUMO, enhancing the plasmon intensity. While the experiment highlights the interaction between molecular orbital and tunnel junction plasmon, an interesting question remains is the realization of light emission from molecular transitions in the STM.

6.2 Future Prospects

The successes of the experiments presented here open the possibility of fruitful future studies. The first of these is the application of hydrogen rotational imaging to molecular orbitals. Our imaging of MgP molecules was conducted on the metallic surface, where it is impossible to identify the molecular orbital. When placed on the oxide, the MgP preserves the spatial distribution of the LUMO in STM images [9-10]. Applying the same imaging method as discussed in Chapter 2, we were able to probe the interaction between H₂ and LUMO of MgP. The H₂ rotational imaging resembles the MgP LUMO, indicating charge transfer from the H₂ to the MgP. Our results have been published in Physics Review Letters [11]. H₂ rotational imaging of other molecules can also give insightful information on their chemical structure as well as orbital interaction with H₂.

Our experiment on Au nanoclusters highlighted their electronic and optical properties and interaction with plasmons. Since Au is an active catalyst in nanoscale experiments [12], understanding their plasmonic properties can help us improve their chemical reactivity. In

particular, Au is an ideal catalyst in CO oxidation or CO₂ reduction reactions [13]. The results obtained in this dissertation could give us better understanding of the mechanisms involved as the plasmon modes can be used as a guide to photochemistry and catalytic reactions.

The experiments on hemin and azulene also give us opportunity to explore the optical properties of these molecules further. We have seen how the interaction of azulene LUMO with SPR of metal surface can lead to enhanced light emission. Further studies include looking for light emission from molecular transitions. As noted earlier, azulene emits from the S₂ state rather than the usual S₁ state [14]. Applying STM light emission methods to an azulene system supported on insulating layer, we can potentially map the excitation of azulene with sub-Angstrom resolution, elucidating the emission mechanism and its connection with molecular orbitals.

Another rewarding experiment is the upconversion of photons. By shining femtosecond laser into the chamber, the combination of photons and tunneling electrons can potentially excite light emission at a higher energy than the incoming photon. Such studies have been performed on surfaces and other molecules [15]. The study of upconversion process for azulene can give us further insight into the electron-photon coupling inside the molecule. The experiment, if successful, would further demonstrate the effectiveness of STM imaging and light emission techniques.

Bibliography

- [1] W.L. Yim, J.S. Tse, and T. Iitaka, Phys. Rev. Lett. **105**, 215501 (2010).
- [2] C.S. Carr, and J.B. Hughes, Environ. Sci. Tech. **32**, 1817 (1998).
- [3] T.M. Wallis, N. Nilius, and W. Ho, Phys. Rev. Lett. **89**, 236802 (2002).
- [4] N. Nilius, T.M. Wallis, and W. Ho, J. Phys. Chem. B **109**, 20657 (2005).
- [5] X.H. Qiu, G.V. Nazin, and W. Ho, Science **299**, 542 (2003).
- [6] S.W. Wu, G.V. Nazin, and W. Ho, Phys. Rev. B **77**, 205430 (2008).
- [7] C. Chen, P. Chu, C.A. Bobisch, D.L. Mills, and W. Ho, Phys. Rev. Lett. **105**, 217402 (2010).
- [8] W.L. Barnes, J. Mod. Opt. **45**, 661 (1998).
- [9] S.W. Wu, N. Ogawa, G.V. Nazin, and W. Ho, J. Phys. Chem. C **112**, 5241 (2008).
- [10] U. Ham, and W. Ho, Phys. Rev. Lett. **108**, 106803 (2012).
- [11] S.W. Li, D.W. Yuan, A. Yu, G. Czap, R.Q. Wu, and W. Ho, Phys. Rev. Lett. **114**, 206101 (2015).
- [12] M. Valden, X. Lai, and W. Goodman, Science **281**, 1647 (1998).
- [13] A. Berko, Z. Majzik, and A.M. Kiss, J. Phys. Conf. Series **61**, 110 (2007).
- [14] M. Beer and H.C. Longuet-Higgins, J. Chem. Phys. **23**, 1390 (1955).
- [15] B. Zhou, B.Y. Shi, D.Y. Jin, and X.G. Liu, Nature Nanotech. **10**, 924 (2015).

Appendix A

Operation and Maintenance of a Femtosecond Laser System

A.1: Introduction, Safety, and General Maintenance

This is a comprehensive guide to the maintenance and operation of the Ti:Sapphire Femtosecond laser system in STM 2. In this first section, general laser maintenance guides and safety operating procedures are discussed. Later sections will discuss in detail the operation of the various components of this complex system.

A.1a: Laser Safety:

The first and most important issue regarding laser operation is safety. The STM 2 laser system includes a diode pump laser operating at 532 nm with power greater than 5 W and a Ti:Sapphire pulsed laser at 820 nm with average power at 800 mW. Such powerful beams can easily cause irreversible eye damage should direct exposure occur. To prevent such accidents, the following safety precautions should be taken at all times:

- Before turning on the laser, hang the “laser on” sign outside STM 2 door. This warns other people that laser is operating and to use caution when entering the room. Also, if someone else is in the room, warn them that you are turning laser on.
- Do not have any metallic objects (watches, rings, etc) on your hands/ wrists when working on optics. They can reflect laser beam inadvertently.
- When making alignment adjustments on the optical table, always keep eyes above beam path. By same logic, never direct beam upwards above the optical table.

- Always fix optical components on the table that are in use. A falling mirror could reflect beam in an unpredictable direction
- Always block off any stray beams on the table. Unblocked beams can cross path with walkways and desk area around the optical table and become a major hazard.
- Wear safety goggles whenever possible. We have special cards that allow the beam to be seen even when wearing goggles, one for 530 nm wavelength, another for 800 nm. They make alignment easier with the goggles. Use them as much as possible.
- Use minimum power necessary when aligning laser. The green pump laser is more visible for a given power, use that for alignment to junction, to minimize the power necessary.

A.1b: Cleaning Optics:

The second most important issue for laser system maintenance is cleanliness. Due to the sensitivity of the various optical components of the system to dust pollution, it is critical to keep the room clean. Vacuuming of the STM 2 room should be done at regular intervals, and the drapes around the optical table should always be kept down unless in the process of alignment.

Even with regular upkeep, it is often necessary to clean the optical components themselves. Proper procedure is important, to avoid damaging expensive and hard to replace parts.

Guidelines for cleaning optics are below (see also Fig. A.1):

- Fold two to three pieces of lens paper to about $\frac{1}{4}$ in width. Clamp firmly with scissor clamps, making sure the end of the scissors does not protrude out of the lens paper.
- Cut the end of the paper if necessary for confined spaces.
- Use dropper to soak lens paper with methanol or optics grade acetone. Make sure paper is damped but not overly wet.

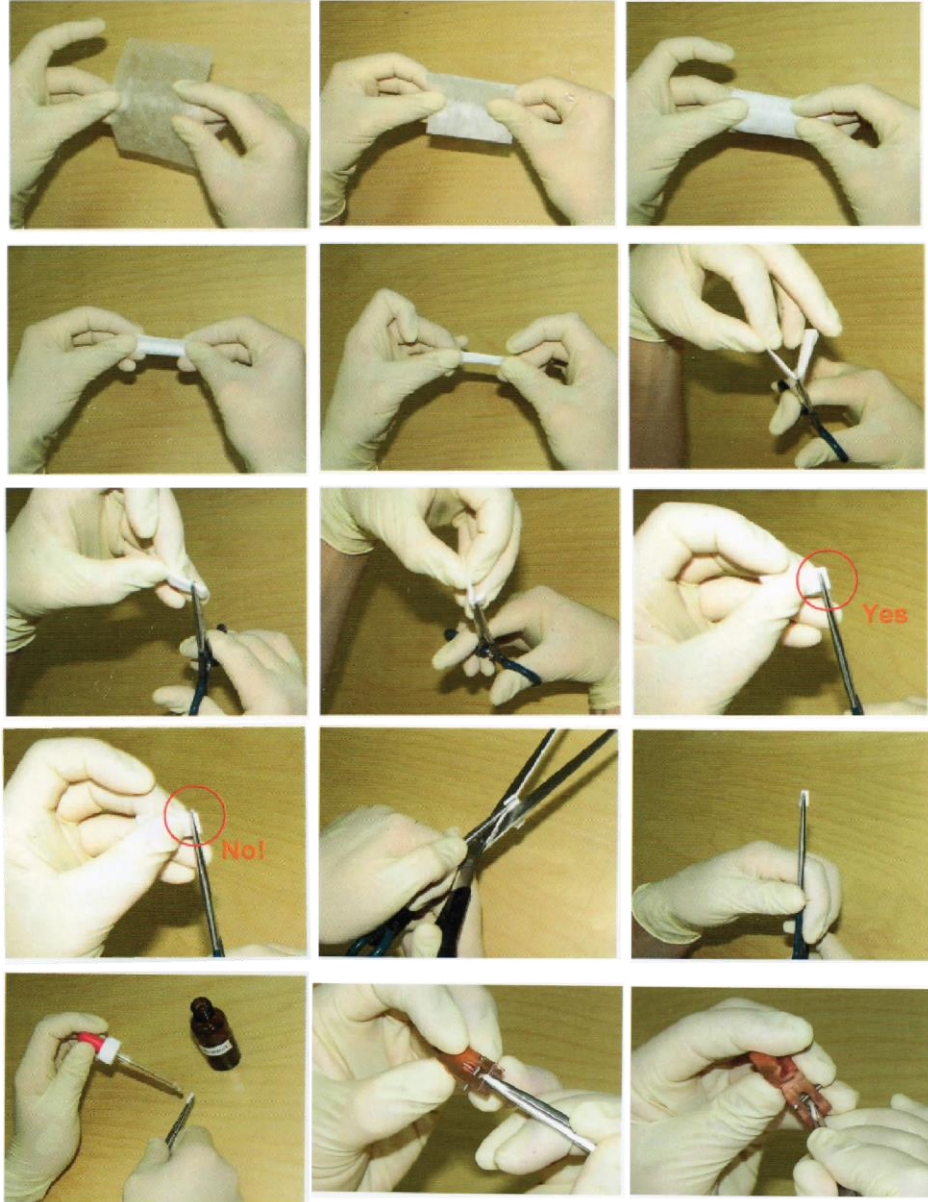


Fig. A.1: Cleaning optics and laser crystal

- Wipe across the surface of the optics component in one smooth, firm motion. Do not press too hard into the optics, as it may cause scratches on the surface. You can make one more swipe with the other unused surface of the paper, but do not reuse the same lens paper after initial wipe.
- Repeat with fresh lens paper if necessary.
- Take care that you do not make contact with the optics surface with the clamp.

A.1c: Cooling Water:

Both the pump laser, Verdi V diode laser from Coherent, and the Ti:Sapphire oscillator from Giga Optics require water cooling to operate. They share the same cooler and the water lines are connected in parallel. The cooler unit must be on whenever the power to the pump laser is on. Unless unit is in the process of changing water, there is really no reason to turn off the cooler. The cooling water must be changed every 2 to 3 months. Use deionized water and ethanol alcohol in a 95% – 5% mixture by volume. Note on cooler unit the date of each water change to keep track of when the next change should be. See Fig. A.2 for details.

A.2: Ti:Sapphire Femtosecond Laser Operation

This section details the operation of the Ti:Sapphire femtosecond oscillator. The basic theory and operation, as well as the procedure to achieve mode-lock, methods to optimize output power, will be discussed. Once familiar with the theory and operational details of the system, you can formulate your own procedure to obtain best performance from the laser.

A.2a: Ti:Sapphire Laser Theory

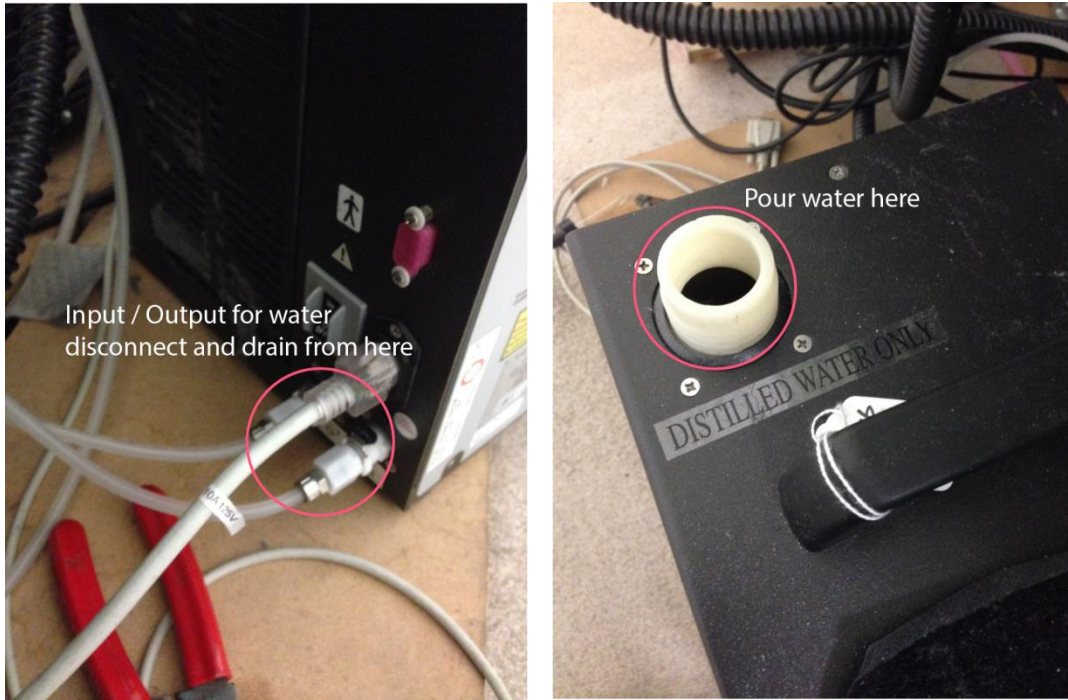


Fig. A.2: Water cooling for Verdi Laser

This is a brief description of the theory of Ti:Sapphire laser. For more detailed information, consult the references cited at end of the manual. In a Ti:Sapphire laser, the lasing medium is Al_2O_3 crystal doped with Ti^{3+} ions. See Fig. A.3 for an energy diagram of the lasing process. When embedded within the Al_2O_3 lattice, the Ti^{3+} ions have a single d shell electron in their outer level. The interaction between this electron and neighboring oxygen atoms lifts the degeneracy of the angular momentum states of the d electron, creating an energy gap in the green – blue region. This is the absorption band of the Ti:Sapphire laser. After the absorption of a green photon, the Ti^{3+} ion can lower its energy by displacing from its equilibrium position. This caused the resulting emission to be lower in energy (red shift). Due to the interaction between the electronic state and vibrational levels of the Ti^{3+} ion, the electron can decay into a multitude of vibrational states in the final state. Thus the emission spectrum of the Ti:Sapphire crystal has a wide bandwidth, making them ideal for tunable lasers.

To generate ultra-fast pulse from the Ti:Sapphire crystal, a process called Kerr Lens Mode-Locking (KLM) is used. In simple terms, mode-locking is a process in which the many optical modes in a laser cavity become locked in phase and generate short pulses. To achieve this, a resonant cavity, such as shown schematically in Fig. A.4, is used. When the pump laser hits the Ti:Sapphire crystal, the generated laser beam propagates in both directions along the crystal axes. The resonant cavity amplifies the resulting standing wave modes, creating a train of short pulses.

The optical properties of the crystal facilitate the creation of mode-locked pulses. Due to the dispersive properties of the crystal, a non-linear effect known as “self-focusing” occurs. When the beam propagates in the crystal, the self-focusing effect causes the index of refraction to increase at the center of the beam. This has two effects, one is it creates more favorable condition for mode-locked lasing at the center of the beam. By using a lens to focus the pump

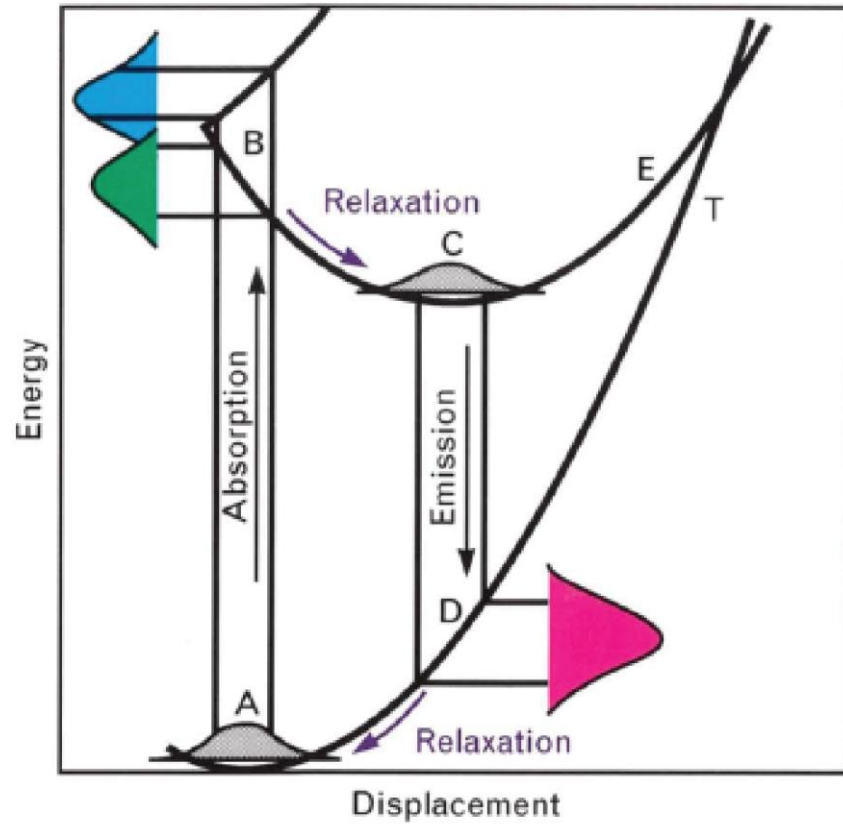


Fig. A.3: Energy diagram for Ti:Sapphire lasing [1]

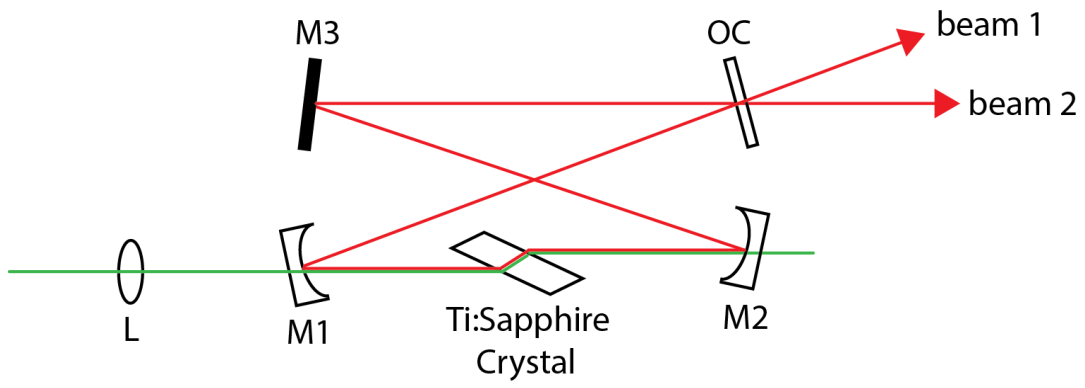


Fig. A.4: Schematic diagram of laser cavity

beam as it enters the crystal, the mode-locked lasing is even more emphasized in the cavity. Self-focusing in the Ti:Sapphire crystal also introduces self-phase modulation in the laser beam, generating more bandwidth for mode-locked lasing, shortening the pulse width. Detailed description of the theory of femtosecond Ti:Sapphire lasers can be found in the references [1-2].

A.2b: Laser Operation Characteristics

Below are the specifications for the Gigaoptics Gigajet 50 femtosecond laser system. When all optics are aligned and optimized, these are the parameters that should be expected. The specifications assumed a pump laser power of 5.5 W at the entrance of the Gigajet system. The stated power of the Verdi pump laser and measured power could be different.

Max mode lock power: 840 mW

Central Wavelength: 820 nm

Pulse Width: ~30 fs with pulse shaper

Polarization at output: s polarized (parallel to surface)

To get maximum power of 840 mW, fine tuning of the oscillator is necessary. Under normal circumstances, power of 750 – 800 mW is acceptable. See Fig. A.5 for complete laser performance characteristics.

A.2c: Verdi Pump Laser Operation

The Verdi 5 diode laser is the pump laser for the Ti:Sapphire system. Below is a detailed account of its operating procedures. See Fig. A.6 for picture of front control panel.

Test data report

Customer: UCI Prof. Wilson Ho
Manufacturing Date: Sep-01-2009

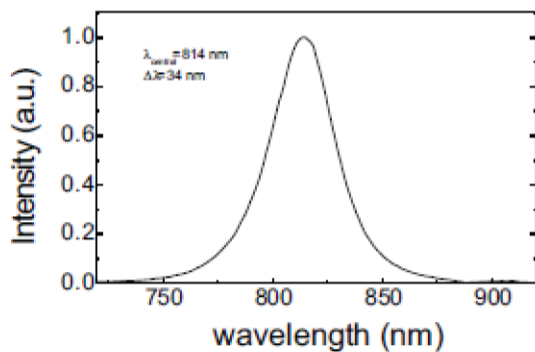
MODEL NO.	GIGAJET 50	GIGAOPTICS GmbH
SERIAL NO.	G50-18	Blarerstr. 56
MFG. DATE	9-2009	D-78462 Konstanz
		Germany
		US Patent 4,618,423
		MADE IN GERMANY

Micrometer positions:

L: 0.12
OC: 2.03
M2: 2.81
K: 5.38

Output power @5.5 Watt pump power: 800 mW

Output Spectrum



Pulse duration after external
linear compression < 26 fs

Repetition rate ~5.005 GHz

Pump laser used for testing:
Coherent Verdi V6

Test date: Sep 01, 2009
Measurements by: CJ

Fig. A.5: Gigaoptics Laser Performance



Fig. A.6: Verdi 6 Laser Controller Front Panel

Starting Procedures:

- Before turning on laser power controller, check cooling water is on and running. Make sure water has been changed within reasonable time. (See Section A.1c)
- Turn on power to controller. Switch is on the back.
- Once power is turned on, the system will start warming up. The text “system warming up” should be displayed on the front display panel. It usually takes 10 – 15 mins for laser to be fully warmed up before it can be used.
- Once system is warmed up, the display should say “Standby”, assuming the laser key is in “standby” position. Turn key to “Laser Enabled” position to turn on diode current. At this point, the laser is lasing, but shutter is still closed.
- Adjust laser power with knob. The power ranges from 0.01 W to 5.5 W. Increasing output power to higher than 5.5 W is not recommended.
- Press “Shutter” button on controller to open shutter. At this point, you should be able to see output beam on table.
- **Note on safety:** Try to look away from table when standing up after turning on laser shutter. It minimizes chance of stray beams hitting your eyes.
- You may adjust power with the laser on. It does take some time for power to stabilize, though.

Shut Down Procedures

- Close the shutter, turn laser key to “Standby” position.

- Press “Menu Select” on front panel, use up and down keys to cycle options until “LBO heating/cooling”. Press “Menu Select” again once you enter the sub-menu to start cooling the diode.
- Once the LBO temperature reading goes to around room temperature ($< 25^{\circ}\text{C}$), it is safe to shut off the power to the controller.
- Should you want to restart laser during the cooling down process, press “Menu Select” again in LBO heating / cooling submenu to warm up the laser again. Once the LBO is warmed up, it should say “Standby” again in the main menu, and can be operated as before.
- Once the LBO has cooled, it is best to turn off power. There is a glitch in the controller that if you leave it on after cooling too long, an error message will appear.
- Since diode in the laser have finite life time, do not leave the laser on for extended amount of time unless necessary.
- If laser is done for the day, but need to be turned on again the next day, it is best to put it on standby mode rather than do a complete shutdown.

A.2d: Mode locking Gigaoptics System

To get the femtosecond system to mode lock, it may require some tinkering with internal optical components. See Fig. A.7 for positions of all mirrors and micrometers.

- Turn on pump laser. Use the two mirrors to guide pump beam into the Gigaoptics system (See Section III for diagram of optical path). Make sure power is set at 5.5 W. Keep in mind that actual power may be different from one displayed. Right now a displayed power of 5.15-5.2 W will give approximately 5.5 W at input of Gigaoptics.

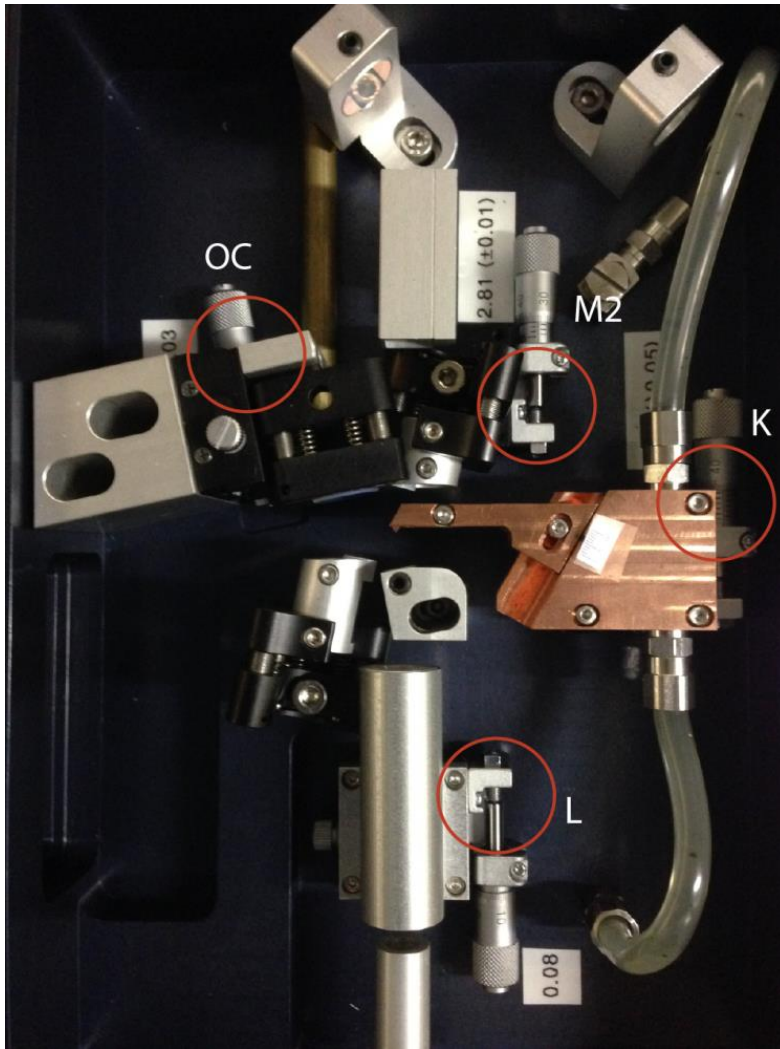


Fig. A.7: Gigajet Laser Cavity: Mirror Positions

- Wait a few minutes for pump power to stabilize. Once the pump power has increased, Ti:Sapphire crystal should start lasing in CW mode.
- Use the power meter to measure the output power of the Ti:Sapphire laser. CW power should be around 400 mW.
- To start mode locking, perturb the cavity by pressing the mode locking button to the left of the laser. As you press the button, the beam will change shape and complexion, until it disappears. For best results, press the button only slightly, until the beam change complexion and let it go quickly. It will take repeated presses to start mode locking.
- Alternatively, you can trigger mode locking by pushing the translational stage that M2 is mounted on. Be careful not to change the micrometer setting while doing so. In some cases this will be more effectively than using the push button.
- Once mode locked, the color of the laser beam will change to a darker shade of red. The power measured will also increase. The optimum power should be around 800 mW, though the beam may not reach that desired power at first. Even power as low as 500 mW can be acceptable, as the system can be optimized.

The above instructions assume that mode locking can be achieved relatively easily. In most cases, though, some adjustments are needed in order to achieve mode locking. In such cases, follow the steps below in order to get system back into mode locking condition

- Check water cooling. It is rare that there would be problem with it, but you should check it first. It's important for the water cooling to be working because the Ti:Sapphire crystal need to have stable temperature in to mode lock.
- Clean the optics and crystal inside the cavity. To clean the crystal, unscrew the crystal holder assembly and take assembly out of the cavity. Very gently, wipe both faces of the crystal

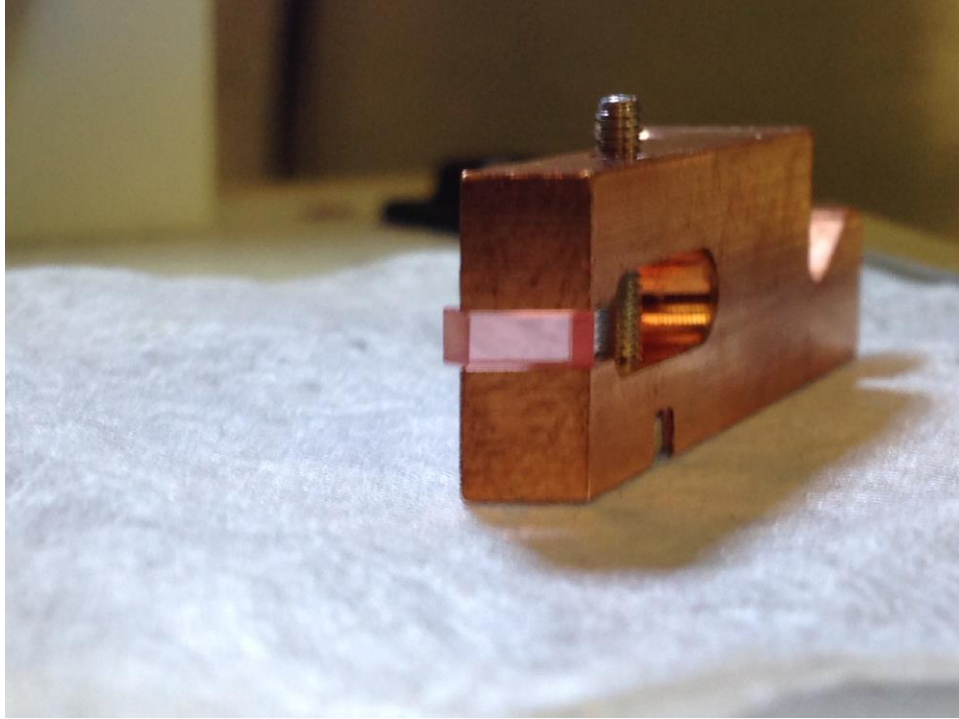


Fig. A.8: Ti:Sapphire Laser crystal holder

with acetone using method described in Section I. Since the crystal face is very narrow, fold the lens paper appropriately. (See Fig. A.8 for picture of crystal holder assembly)

- **Note: Be very careful in cleaning the crystal, as it is possible to nudge crystal out of position if pressed too hard. Ti:Sapphire lasing is very sensitive to crystal orientation in the holder.**
- To clean the four mirrors (M1, M2, M3, OC) comprising the cavity, move micrometers on OC and M2 all the way back to give you more room. **Remember to note down the micrometer positions before moving them.** Move the mirrors back to original positions when finished.
- Put the crystal holder back in place, use the position marker on the holder to place it near the original position.
- After cleaning the internal optics, you should see increase in Ti:Sapphire output power. Try to mode lock system again. If difficulty persists, a more thorough realignment of the cavity mirrors will be required.
- Ability to mode lock depends most sensitively on position of M2 and K. Adjusting the micrometer position of M2 changes the beam shape. For M2 very close to zero (mirror close to crystal), the cavity would be out of the stability zone and unable to lase. As you move M2 back, you will start to see the CW lasing from the Ti:Sapphire crystal. The beam should look bright shade of red with a horizontal line across it. As M2 is moved further back, there comes a point where the appearance of the beam will change, to a duller color and rounder beam shape. The optimum mode locking position should be within 50 μm of this point. As a starting point, put M2 to where the laser beam change appearance and move back a few microns.

- Make sure CW power is maximized. To do this, perform beam walk by adjusting M3 and OC. (See Fig. A.9 for positions of screws.) Start with the horizontal direction, adjust the two mirrors simultaneously until power is maximized. Continue with the vertical direction. While adjusting the horizontal direction, turn the screws in both mirrors in same direction. For vertical direction, turn them in opposite directions. To get best alignment, repeat the beam walk several times. You should be able to get around 400 – 450 mW of CW power.
- Once CW power is optimized, try to obtain mode lock by varying K and M2. Start with the previous optimum position of K, step in increments of a few microns. For each position of K, adjust M2 as stated above to find mode locking position. Perturb the cavity with the push button or pushing the translation stage of M2 to obtain mode locking. Check both higher and lower values of K.
- When changing K, the CW power is likely to decrease. This is due to the input beam being out of focus when it hits the crystal. To adjust the focus, use L. Again, after each adjustment of K, adjust L to maximize power. This last step can be done after mode locking condition is found.
- After all adjustments are made, record the micrometer positions of all mirrors (OC, M2, K, L). It will be useful to note the mode locking condition so next time you have a starting point to work with.
- Once found, the mode locking condition should be pretty consistent. Minor adjustment with M2 might be required, but should not deviate much from optimized position. Once a while, the optics may need to be cleaned, so follow above procedures and you should be able to get system back into mode locking condition.

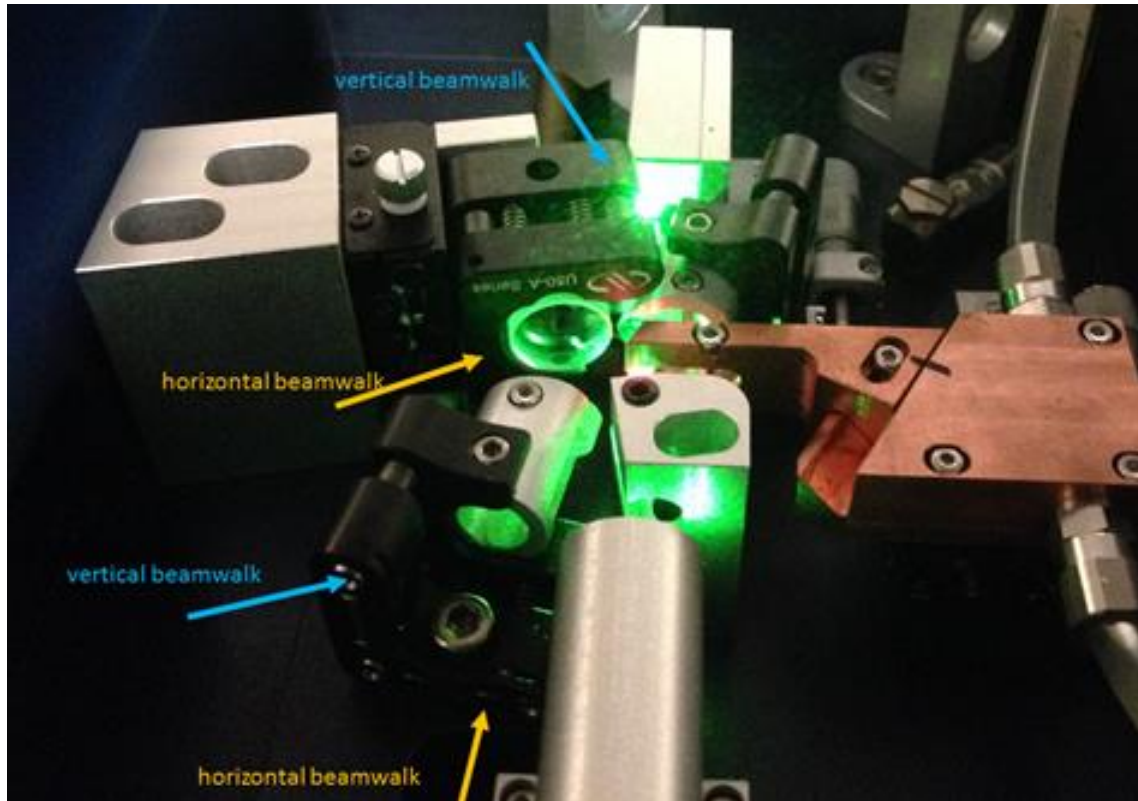


Fig. A.9: Beamwalking M3 and OC

- Moving the crystal holder along the mounting slot can help find best mode locking spot on the crystal, but doing so may require realignment of K and L. Note that a “measuring tape” has been added to the crystal mount to make it easier to position crystal repeatably.
- **Important Note: In the cleaning and aligning of the cavity, make sure the mirror mounts M1 and M2 are not disturbed. They are integral to the cavity’s ability to mode lock, and disturbing them will make irreversible changes to the geometry of the cavity. We do not have ability to adjust M1 and M2 beyond using the micrometer.**

Re-mounting the crystal in the holder

If, for whatever reason, whether it was moved out of position during cleaning, or requires replacement, the crystal needs to be replaced in the holder. Follow the steps below. Fig. A.10a shows the correct orientation to mount crystal. Fig. A.11 is quote should a crystal replacement is needed.

- Prepare a clean area with a flat surface. Tools needed include tweezer with plastic tip (do not use metal tweezers), and correct Allan wrench key. The tools should be cleaned to UHV standards.
- On the clean surface (could cover with aluminum foil), place two layers of lens paper. Put the crystal on the lens paper, in the correct orientation to be clamped by the holder.
- Put the holder over the crystal, pressing the end face against the lens paper on the table surface (Fig. A.10b). Carefully tighten the screw over the crystal so that the crystal and holder end face are parallel to each other. It might help to have someone else press the crystal against the table with a plastic tweezer. The screw needs to be very tight.

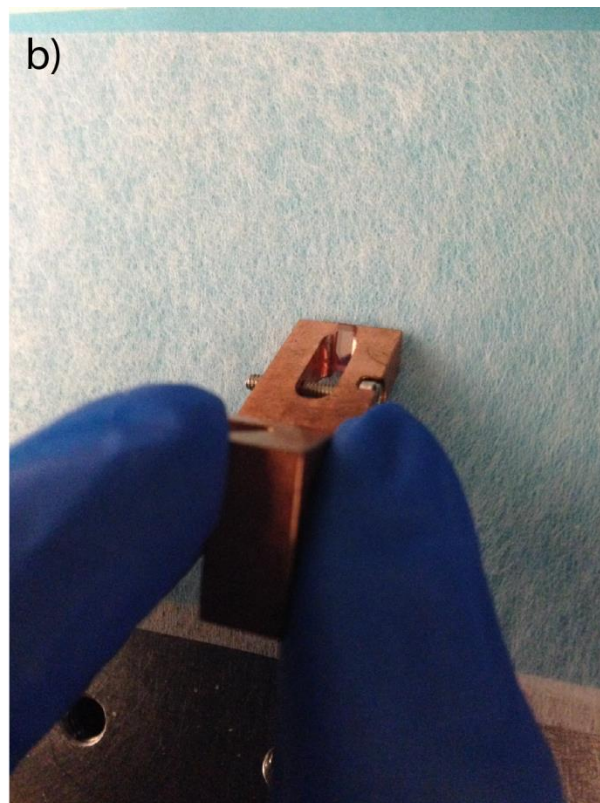
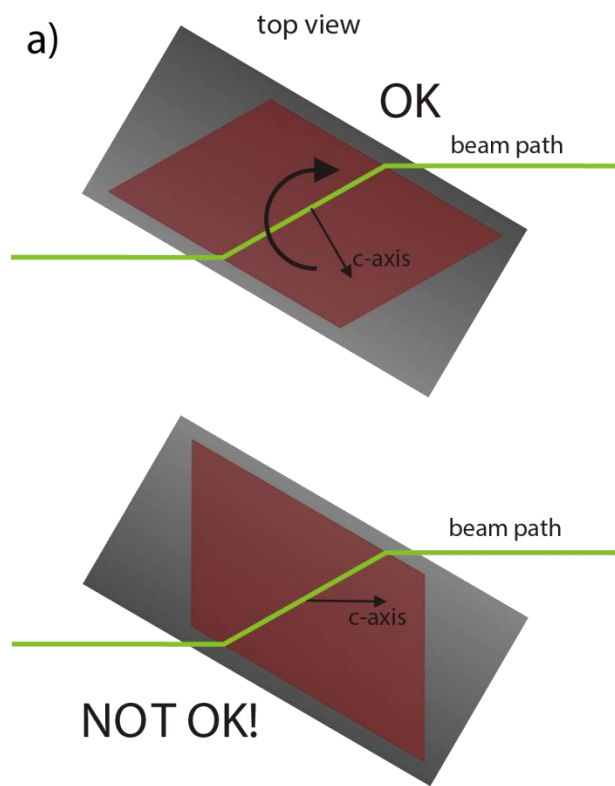


Fig. A.10: Mounting crystal onto holder



GT Crystal Systems, LLC
27 Congress Street
Salem, MA 01970
Phone: (978)745-0088 / Fax: (978)744-5059
www.gtat.com

Quotation #0713047.xls
7/16/2012

Price Quotation

To: UC Irvine

RFQ: email

Attn: Arthur Yu

NO. PAGES: 1

QUANTITY	DESCRIPTION	UNIT PRICE
1 or 2	HEM Ti:Sapphire Laser Rod 90° Laser Polish // Brewster Angle Ends 4mm x 2mm x 1.70 mm Path Length α 514 : 5.00 \pm .35 per cm, FOM: >150 LPSP* Absorption ~ 57%	\$1,320
*LPSP = Low Power Single Pass		
This quote is valid for 30 days. Terms: Net 30 days. This delivery schedule is subject to revision depending upon production schedule when order is received.		All prices FOB Salem, MA

Delivery: 3-4 Weeks, ARO

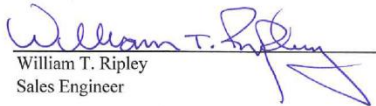

William T. Ripley
Sales Engineer

Fig. A.11: Quote for replacement Ti:Sapphire crystal

- After the screw is tightened, inspect the crystal position to ensure crystal orientation is correct, and crystal face is absolutely parallel to end face of crystal holder. If not, system performance and ability to mode lock will be affected.
- It might be advisable to check the crystal assembly under a microscope to ensure better crystal alignment. It is also possible to perform the installation under the microscope. Make sure to put lens paper on microscope stage before putting crystal on it.
- For minor adjustments of crystal alignment, don't take the crystal completely out of the holder. Just loosen the screw and adjust alignment and re-tighten.
- After installing the crystal, clean both crystal faces before mounting it back into laser system.

A.3: Basic Optical Alignment

This section discusses the basics of alignment laser beam through the optical table. It goes over the overall setup of the STM 2 optics system, how to use irises and the working of the laser power controller.

A.3a: STM 2 Optics Path

Fig. A.12 shows the complete optical path of the STM 2 system. There are two independent paths for the green (pump) and red lasers into the junction. There is also option to use or bypass the delay stage. To align the laser beam along the optimum path, use the vertical and horizontal controls on mirrors. Keep the beam close to center of each mirror for best results. There are multiple irises along the path, they are instrumental to proper alignment of beam and their use is discussed in the next section.

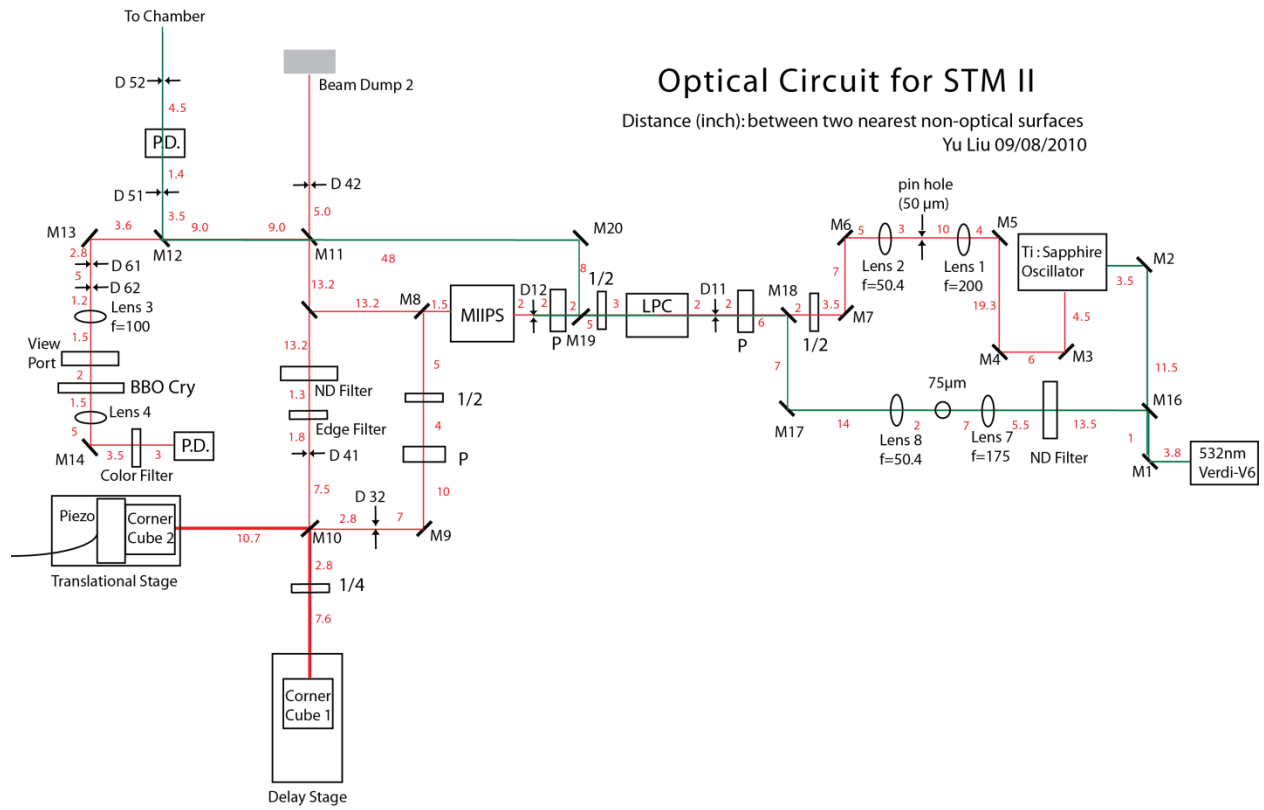


Fig. A.12: Optical path for laser system in STM 2 (drawn by Yu Liu, 2010)

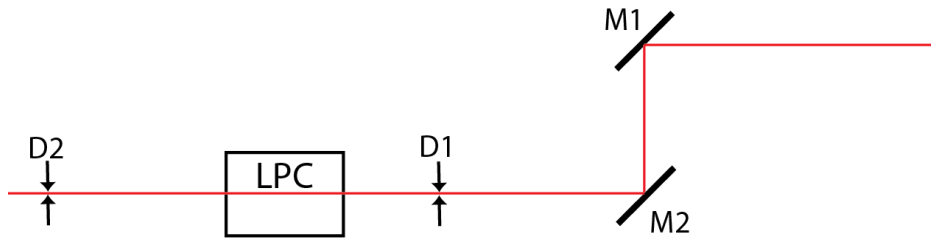


Fig. A.13: Alignment using irises

A.3b: Alignment Using Irises

To ensure proper beam alignment along the path, irises are important tools. Generally, two irises are used in tandem with two mirrors to ensure correct path of the beam. In setting up the optical system, alignment is optimized through use of mirrors. Once optimization of optical path is achieved, two irises are placed and centered on the optimized path so that in future alignments they can be used to reproduce the desired beam path. Fig. A.13 shows an example of an optical pathway aligned with irises. To align with the irises, use M1 to align beam to center of D1, then use M2 to align beam to center of D2. Repeat the process several times until the beam passes through centers of both D1 and D2.

A.3c: Using the Laser Power Controller (LPC)

For experiments involving shining laser into the STM junction, one big obstacle experimentally is the temperature fluctuation caused by the laser shining on the tip. Such thermal effects will cause instability in the tunnel junction and make it difficult to scan normally. To combat such problems, the LPC is used to minimize the power fluctuations of the laser, and make a stable tunnel junction. Below are instructions on using the LPC. Consult Fig. A.14 for front control panel of the LPC.

- LPC consists of the “black box” unit on the optical table and the controller. First, make sure the laser passes through the entrance and exit points of the LPC unit. Two irises are placed in front and behind the LPC, use them for correct alignment.
- Once beam is aligned, turn on power on the LPC controller. Note that if controller is on but no laser beam passes through, controller will show error code.

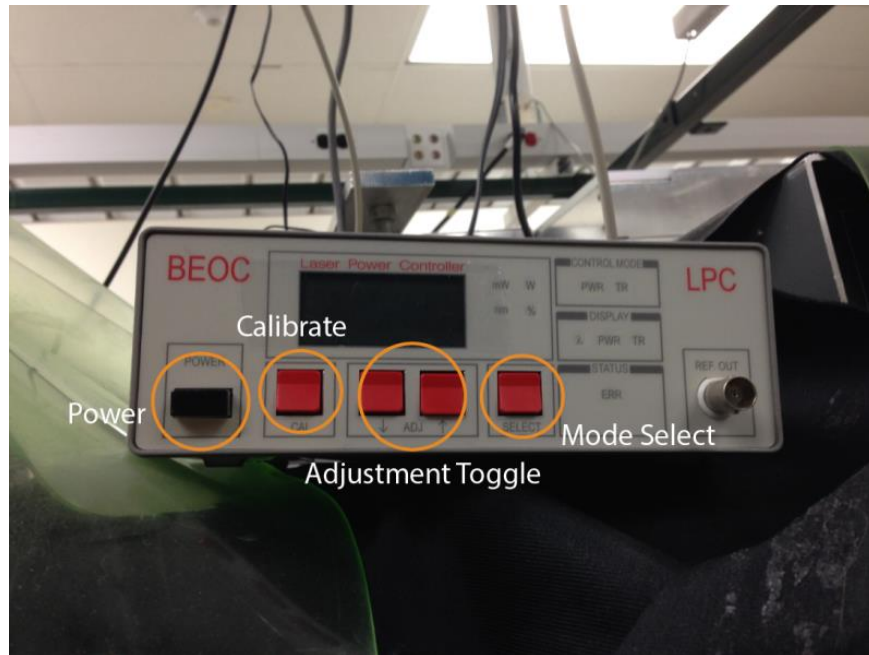


Fig. A.14: Laser Power Controller Front Panel

- There are two operating modes for the LPC: power mode and transmission mode. In power mode, the output power of LPC is fixed, no matter what the input power is. In this mode, the maximum output power of LPC is around 75-80% of the input power. In transmission mode, the transmitted power as a fraction of the input power is constant. So the output power would fluctuate if the input does also. We always operate in constant power mode for STM operations.
- With the beam passing through the LPC, press “Select” to cycle through the displays. When the “Control Mode” is highlighted, press up and down arrows to choose between power and transmission mode. Pressing “Select” again to choose the wavelength of the beam, and again to choose the desired power.
- When the selected power is too low or too high, the error light will turn on. Adjust power until error light is off. For best stability, make sure to operate in the LPC’s “comfort zone”.

A.4: MIIPS Operations

To get the best pulse width and shape out of the Ti:Sapphire laser, a pulse shaper is used. The MIIPS system includes a “black box” on the optical table and controlling software. Also working with the MIIPS is a spectrometer from Ocean Optics. With the pulse compression capabilities of the MIIPS, the output pulse width can be improved to less than 30 fs.

A.4a: Internal Alignment of MIIPS

In order for the MIIPS to be working properly, the laser beam has to be aligned properly at the entrance. This shouldn’t have to be done very often, but if performance of MIIPS is suffering, it might be due to misalignment at the entrance. Fig. A.15 shows the external view and internal optics of MIIPS. There are only two points of alignment possible on the system.

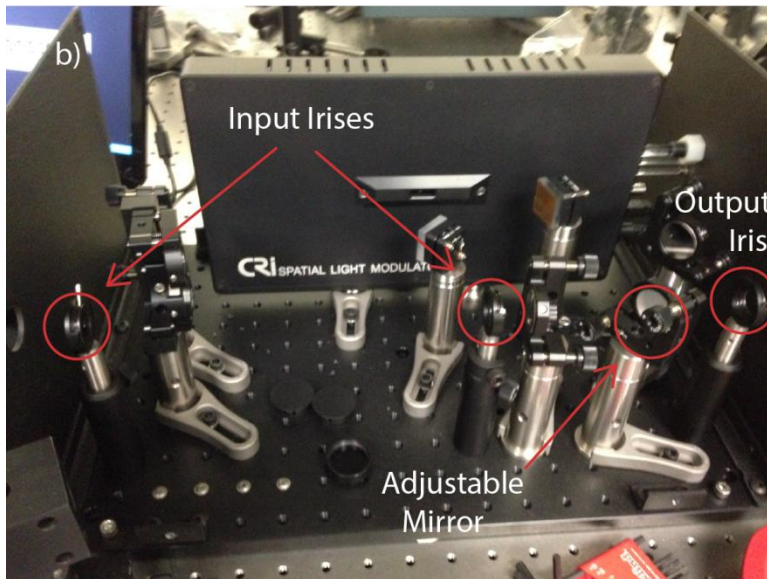


Fig. A.15: External and internal view of MIIPS

- Use external optics (those before MIIPS box) to align to centers of input irises at the entrance of the MIIPS.
- At the output window, adjust the last mirror (circled in Fig. A.15b) to put beam at center of the output iris.
- **DO NOT adjust any other optical component in the MIIPS box. It may cause permanent misalignment that we do not know how to correct without company help.**

A.4b: Using MIIPS software

Once the internal optical path has been aligned, the MIIPS system is ready to be used. The working principle involves taking the second harmonic signal of the laser and using that to optimize the pulse width. The detailed mechanics will not be discussed here. Nevertheless, for this reason we need a BBO crystal to generate second harmonic and Ocean Optics Spectrometer to monitor both fundamental and second harmonic spectrum. Some notes on MIIPS alignment below, as well as instructions on using the software. Fig. A.16 shows the main menu and measurement menu of MIIPS software.

- Fig. A.12 shows the optical path to the spectrometer for MIIPS measurement. Since we want to mimic experimental conditions as much as possible, the MIIPS procedure should be done either with or without going through delay stage, whichever condition the experiment is done in.
- Alignment of delay stage is discussed in section A.5. In aligning to the spectrometer, make sure the laser beam passes through the BBO crystal. If the beam passes through the two irises before the crystal, that would make it pass through center of BBO crystal.

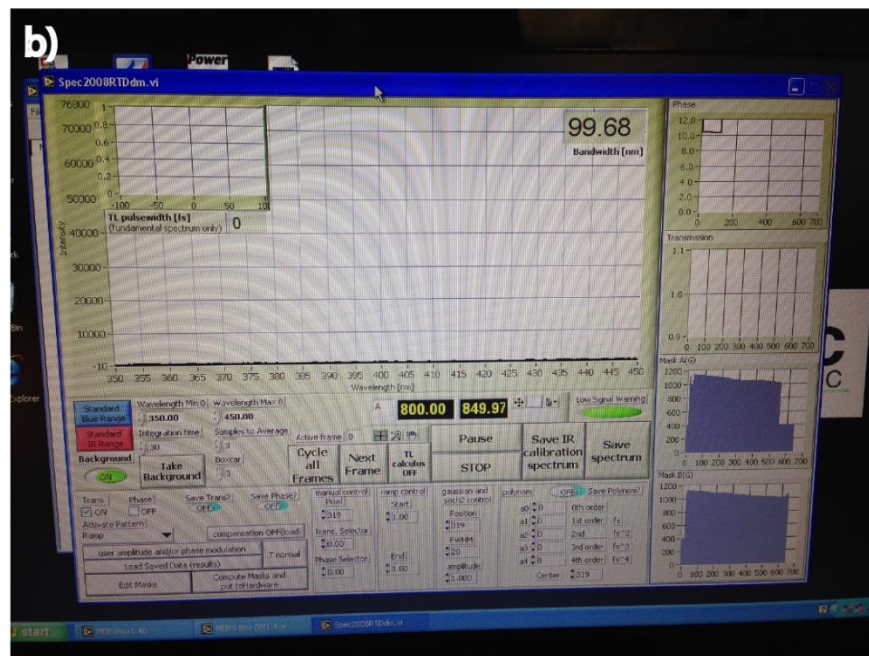
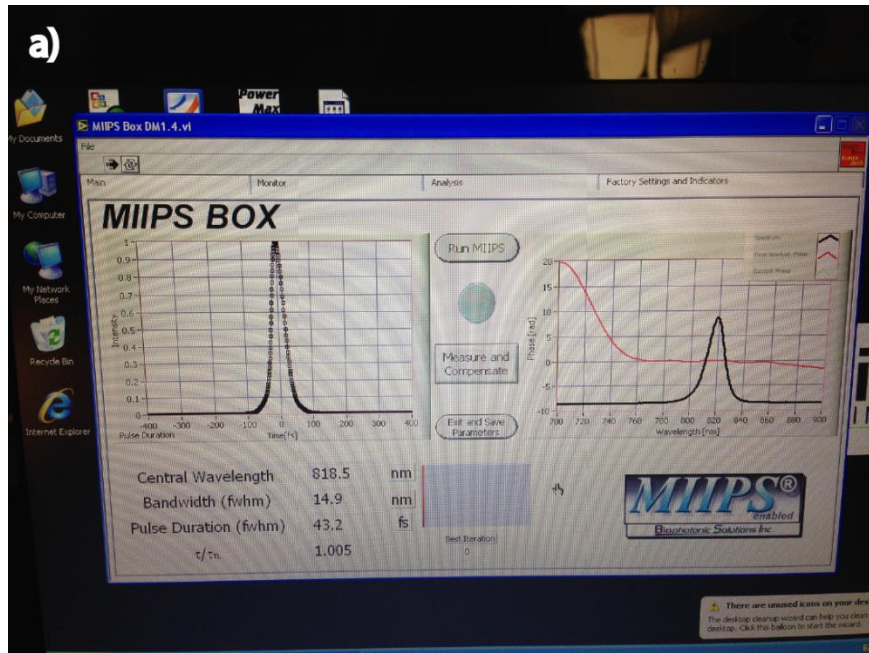


Fig. A.16: Main Menu and Measurement Menu for MIIPS

- Power of generated 2nd harmonic is dependent on rotation angle of the BBO crystal. Rotate the crystal to maximum 2nd harmonic power by visually looking at the generated blue beam. A finer optimization can be performed with the “Measure” screen in the MIIPS software with the spectrometer.
- There is colored filter in front of spectrometer. It filters out the fundamental wavelength of the laser, so only second harmonic will pass through. Use the filter the switch between fundamental and 2nd harmonic for viewing in spectrometer.
- Once the laser has been properly aligned and spectrometer set up, start MIIPS program. Select the COM port that the MIIPS box is connected to. Wait for software to initialize. Note that the USB cable must connect to the same port each time.
- From the Main Tab, click on the “File” menu and select whether “Fine” or “Coarse” measurement is require.
- Go to Monitor Tab. From there, click on “Measure Spectra / Create Modulations” button.
- Take background by blocking laser and pressing the “Take Background” button. Override previous background file when prompted.
- Perform IR calibration: unblock laser, observe that the spectrum displayed is not filtered or obstructed, and press “Save IR calibration spectrum” to save it. Make sure the wavelength range in the lower left corner includes the full range of the fundamental of your laser. For best results, keep the min and max of the range center around the peak of the spectrum. Also, the “Integration time” should be chosen such that the peak of the spectrum is in the middle of the spectrometer’s range.

- Press “Save IR calibration Spectrum” to save the calibration file. After performing IR calibration, be sure to return the Wavelength Min and Wavelength Max button to ranges of the second harmonic of the laser.
- To maximize performance for MIIPS data, set the “Boxcar” average to no more than 3. Set “Integration time” such that the 2nd harmonic spectrum should be at least 1000 counts. Ideally, the range for the blue region (2nd harmonic) should be half of that for the IR region.
- Press “Stop” to return to the Monitor Tab display. For most applications, the option “Start MIIPS From User-Defined Phase” should be on “No” and “Use Amplitude Modulation Type” should be T Mask
- Return to the Main Tab and press “Run MIIPS” to start measurement.
- After the MIIPS finishes, look at the pulse shape and pulse width on screen. If the pulse shape is nice and symmetric (no side peaks), and the pulse width is acceptable, the laser is ready for use. If not, make fine adjustments along the optical path, then restart process.

A.5: Aligning Delay Stage

To perform ultrafast optical experiments, it is customary to measure the signal as function of delay between two pulses. To set up the two pulse trains, the delay stage, essentially a Michelson interferometer, is used. Below is a guide to align the interferometer and setting up the signal vs. τ experiments. Fig. A.17 shows the optical path of the delay stage.

A.5a: Delay Stage alignment

- The key component in the delay stage is the 50/50 beam splitter (BS). After coming out of the MIIPS, the beam is sent through a quarter wave plate and a vertical polarizer before being reflected by a mirror (M9) into the BS. Before the BS, there is a large iris (D32), use mirror M8 to align to center of D32.

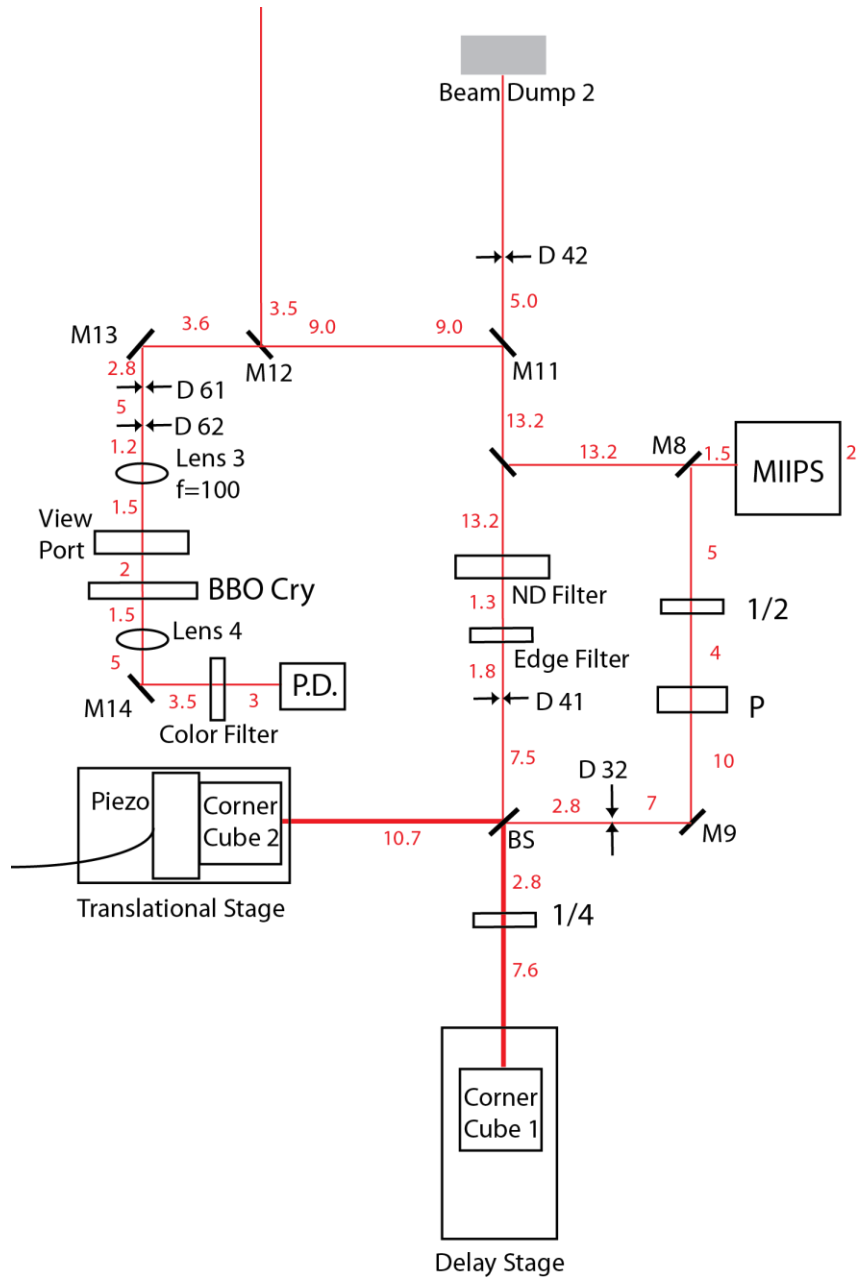


Fig. A.17: Optical diagram for delay stage (drawn by Yu Liu, 2010)

- The beam splits into two parts after the BS. One goes to the linear translator (CC1), the other goes to a corner cube mounted on a piezo shaker and 2-D translation stage (CC2). To make sure the converged beam is co-linear, we align each path separately using two irises along the exit path of the delay stage (D41 and D42).
- To align CC1, use M9 to align to D41. Use the translational stage on the corner cube on the linear translator to align to D42.
- To align CC2, again use M9 to align to D41. Use the mount on the BS itself to align to D42.
- Repeat the two alignments several times to make sure the two beams overlap. At each iris, cover one beam, then the next to see if two beams overlap. May have to dim lights in room to see beam clearly.
- You do not have to move the translational stage of the corner cube of P2 in the alignment. The stage is there to find the temporal overlap position of the two paths.
- Once the two paths are well-aligned, use mirrors to direct to the Ocean Optics spectrometer for MIIPS measurement or directly to the chamber as desired.

A.5b: Finding Zero Point

In order to perform signal vs. delay experiments, it is necessary to find point at which the two pulse trains overlap in time. In the interferometer, the length of the two legs can be varied by translation stages, creating path difference that caused the delay between two pulses. To find the zero point, we use the translation stage in CC2.

- Align the delay stage the same way as for MIIPS. We need the 2nd harmonic to see the overlap.
- Instead of shining into the spectrometer as before, put a beam card in front and observe the 2nd harmonic beam from the two paths. It will be necessary to turn the lights off in the room

to see the spot. Also, this should be done after optimizing the MIIPS, so the 2nd harmonic power should ideally be the best.

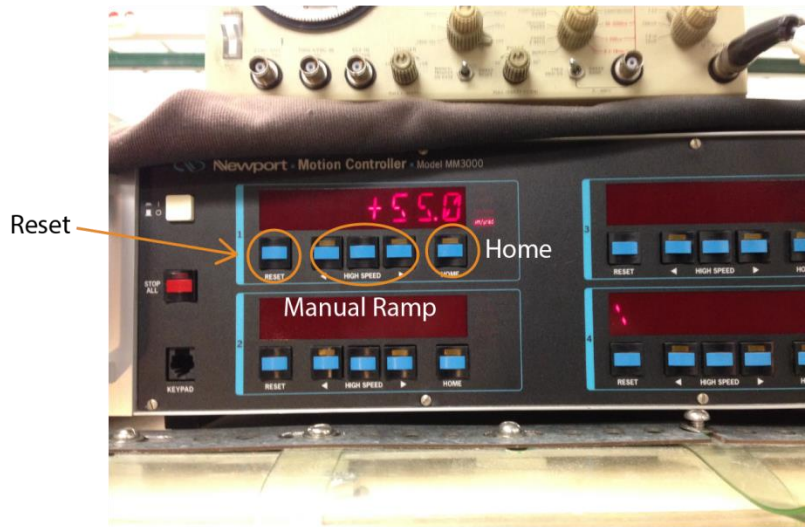
- With the combined beam on the beam card, carefully tune the translation stage on P2 (in direction of beam path) to find zero point. Once zero point is reached, interference from the two paths would cause the combined beam to blink in and out. The effect is quite obvious as the intensity can fluctuate between twice as normal to completely dark. This process can take a long time. Patience is required.

A.5c: Autocorrelation

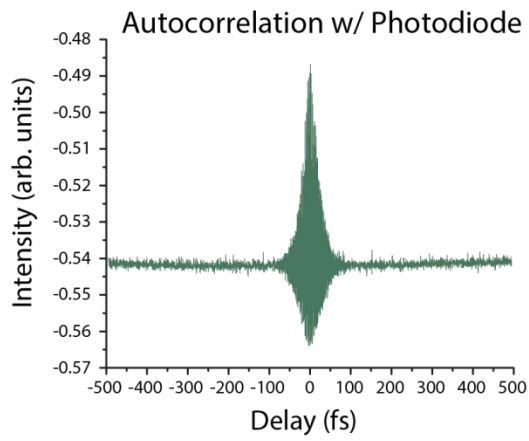
Once the zero point is found following last section, we can fine tune the alignment by performing autocorrelation. Generally, this involves measuring the photon intensity of the 2nd harmonic as a function of delay.

- Remove the spectrometer and replace with photodiode. The connection should be there already.
- If have not done so already, zero the linear translator to reset position. Fig. A.18a shows picture of front panel of linear translator.
- Open the Labview program for autocorrelation measurement, “Signal vs. Delay”. The program can be used for photodiode measurement, as well as measuring current, dI/dV , etc.
- Once the relevant connections are made, the start the program with appropriate delay values. The range from $-30\ \mu\text{m}$ to $+30\ \mu\text{m}$ is sufficient. For the photodiode measurement, the delay at each step is not so important, but for measurements such as I or Z,

a)



b)



c)

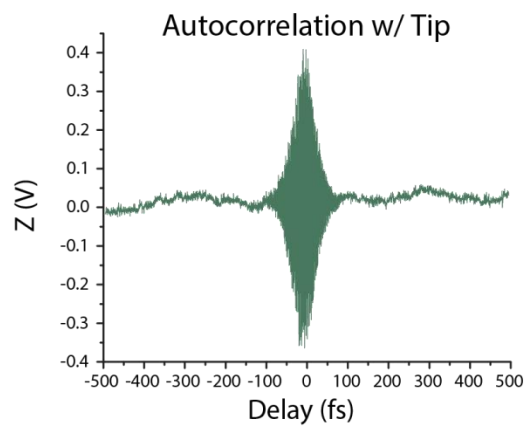


Fig. A.18: Linear Translator and Autocorrelation

- For the autocorrelation measurement, you should see photon intensity increase as pulse delay goes to zero. A typical autocorrelation curve is shown in Fig. A.18b.
- The optimum height to width (FWHM) ratio of the autocorrelation curve should be about 7:1. From the FWHM of the autocorrelation curve (τ_A), the pulse width (τ_p) can be determined. The two widths are related by $\tau_A = k\tau_p$, where k is the deconvolution factor, equaling to 1.41 for Gaussian pulse shape and 1.54 for Sech² pulse shape [3].

A.6: Aligning to the Tunnel Junction

The most important step before doing experiment with laser is actually getting the laser to align to the junction. The process can be a challenge, so here are some tips to help with the process. Fig. A.19 shows diagram for aligning to junction.

- If possible, always use green laser to align to junction. For green, it's possible to lower laser power to a few milliwatts and still have beam be visible.
- Start by aligning the beam with the two irises at the entrance of the periscope. This ensures the correct beam path going into the periscope. Depending on whether delay stage is used or not, the beam might be coming from different paths. Aligning to the two irises (D1 and D2) ensures that even if path of beam is changed before the periscope, once the beam is aligned with the irises, the rest of the path to the junction will remain unchanged.
- After the periscope, the beam will go through the STM viewpoint, then the lens inside chamber before hitting the sample and reflecting out. To ensure optimum beam path, use top mirror (M1) in periscope to make sure beam passes through center of STM viewpoint. Then use bottom mirror (M2) in periscope to make sure the beam passes through center of lens in the chamber. Look into the chamber for the beam spot in center of lens. Note that the spot

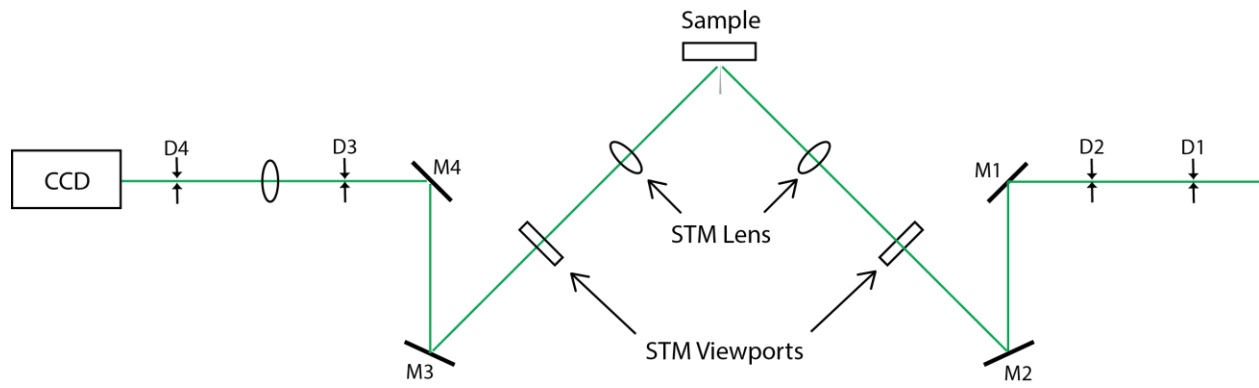


Fig. A.19: Alignment to STM junction

should not be bright. If there is bright spot, it means the beam is bouncing off somewhere inside the lens holder.

- After the beam path is aligned with center of the viewpoint and lens holder, use the X-Y movement of the lens holder to find the sample and tip. First try to see the reflected beam at the output window. Move the input lens holder both horizontally and vertically to get it to hit the sample. Again, avoid seeing any bright reflections. It's okay if you cannot find the tip at first. Getting the reflected beam out is a good first step. All the while, make sure input beam is still at the center of lens holder.
- Once the reflected beam is visible, walk the beam across the sample to find the tip. Use the video camera to locate the tip. When the beam is on the tip, we should see the tip and its reflection on the sample. Put the beam in between the two tips.
- During the alignment, make sure the beam shape is round and not distorted. Distortion is a sign that the beam is hitting something either on the way in or the way out. Check that the beam is not hitting the walls of the lens holder (both input and output), or any of the wires inside the scanner. Also check that the output path is clear all the way to the camera.
- In most cases, the alignment is done with the scanner doors open. This is the best as you can see the laser spots inside the scanner and see if beam hits anything. Sometimes though, if you need to realign laser at low temperature, where opening doors is not possible, the process becomes much more challenging. In that case, you need to look at the camera as well as use the laser spot on the lens holder as guide. The most important thing is still seeing the reflected beam at the output. If you have that, at least you know beam is hitting sample. Finding the tip from there should not be too difficult.

- Once the laser has been aligned, it is good habit to perform autocorrelation at the junction to confirm the spatial and temporal overlap of the two legs of the delay stage. In this case, we monitor z as a function of delay. Setup the delay stage and linear translator as before, but instead of monitoring photodiode output, monitor STM z output with feedback on. Example of such a measurement is shown in Fig. A.18c.
- If performing light emission experiment, it is also important to align the output path correctly. With the beam already align to the junction, look inside chamber to see that output beam is roughly at the center of the output lens holder. If not, use X-Y controls to adjust accordingly.
- In the path to the nitrogen cooled CCD, there are two irises, one big one in front of “black box” (D3), the other one right in front of the CCD (D4). Use two periscope mirrors at the output side to align through both irises.
- Do not shine the laser directly into the CCD. Use the metal cover when aligning.
- Once the irises are aligned correctly, move the beam back to the video camera. We need to optimize the field of view of the output lens holder. With the tip image center on the monitor, pan the lens holder in X and Y directions until the tip image is obstructed. Check that there is ample room to pan in both X and Y directions. Realign the lens holder so that the tip is placed at the center of the field of view of the lens holder. You might have to readjust the camera so tip image remains in center of monitor. Use the mirrors in front of the camera to reacquire tip image if realignment of lens holder moves it off center of monitor.
- Check alignment through the two irises again. Check field of view of lens holder again after that.
- For more exact alignment of the CCD, the spectrograph software needs to be used. Such procedure is beyond the scope of this manual. Check Chi Chen’s thesis for more details.

Bibliography

[1] K.F. Wall, and A. Sanchez, *Lin. Lab. J.* **3**, 447 (1990).

[2] W.T. Silfvast. *Laser Fundamentals* (Cambridge Univ. Press, 2004).

[3] J-C.M. Diels, J.J. Fontaine, I.C. McMichael, and F. Simoni, *Appl. Optics*, **24**, 1270 (1985).

Appendix B

Design and Construction of a Helium Purifier

B.1 Introduction

Due to the increasing cost and uncertain delivery of liquid helium, it has become increasingly difficult to run low temperature experiments. To combat the helium shortage and to save cost for the long term, our group decided to build a helium recycling and liquefaction facility. As part of the liquefaction process, the design and construction of the helium purifier system is an important part of the overall system. Below is a detailed description of the design and construction of the purifier unit, detailing changes over three generations design.

B.2 Generation 1

Design

In the first generation purifier, the design is a simple tube in and tube out. (Fig. B.1) The main chamber contains the zeolite pellets which act as a filter for the impurity in the helium gas passing through it. To maximize the effectiveness of the zeolite filter, we want the helium gas to spend the most of time inside the zeolite. Therefore, one side of the tube was extended to almost the bottom of the purifier, and acts as the outlet. This way, the helium gas would have to travel through the zeolite to get out, allowing for maximum trapping potential of impurities. The top flange seals the nitrogen tank and has three ports (Fig. B.2). The two ports along the diameter of the flange are the inlet and outlet ports for the helium gas. The side port is for temperature sensor monitoring temperature inside purifier body. Two ports are also added on the purifier body itself,

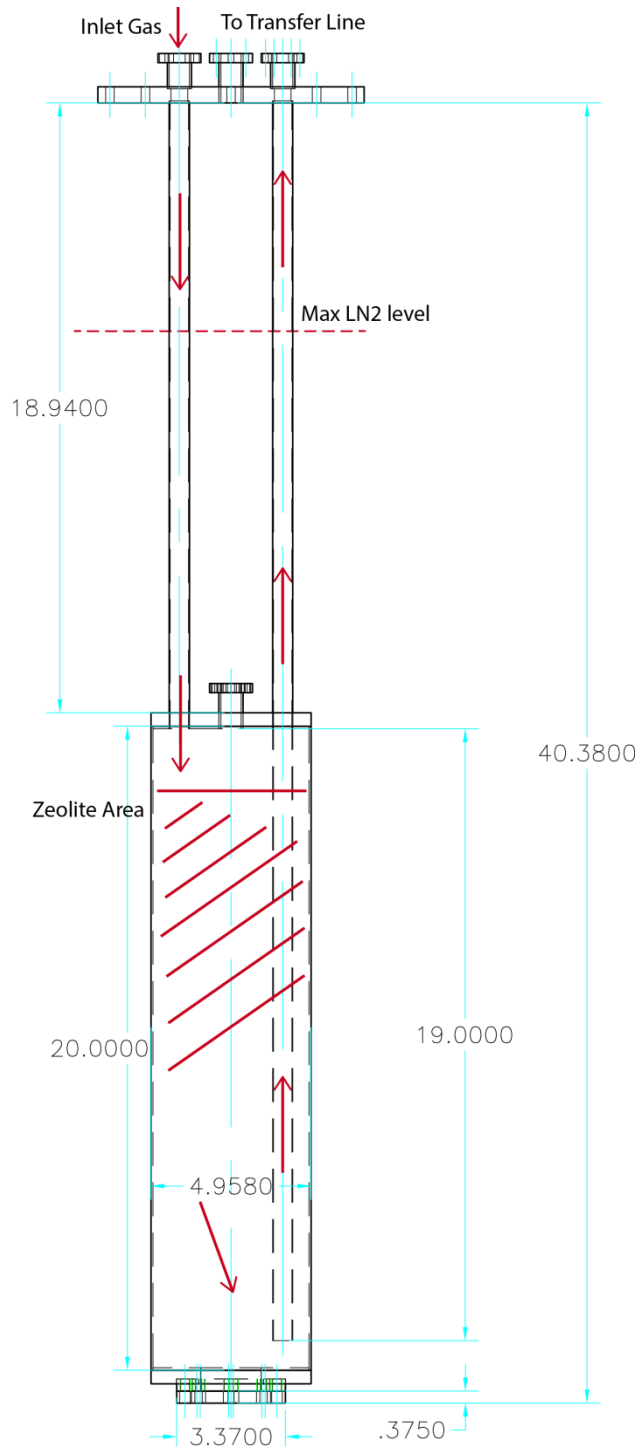


Fig. B.1: Overall structure of generation 1 purifier

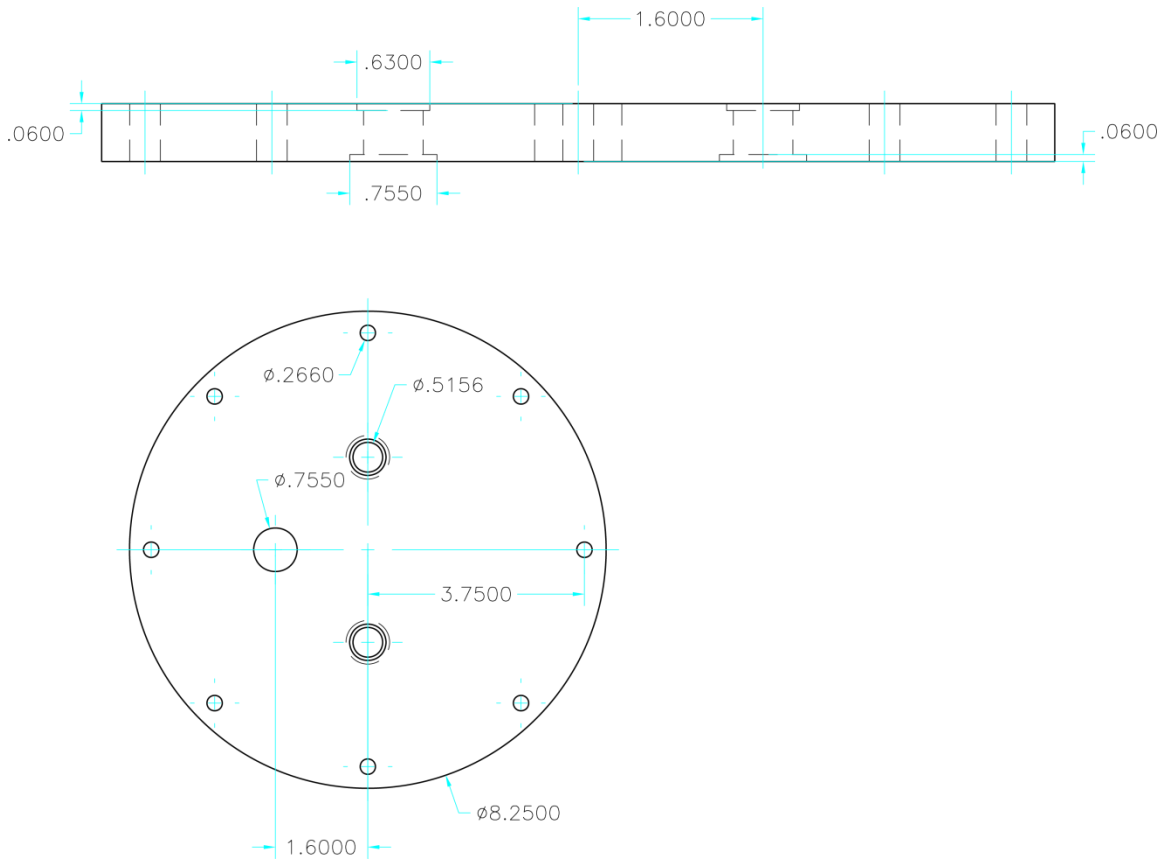


Fig. B.2: Generation 1 nitrogen tank flange

for temperature sensor and filling zeolite pellets (Fig. B.3). There is also a 3-3/8 flange on bottom of purifier to seal and to drain the zeolite in case we need to use fresh pellets (Fig. B.4 and B.5).

Construction

The first generation purifier is welded together into a single piece. There is no assembly required. To make sure everything is leak tight, the order of the welding is important. First, the mini-flanges on top of the nitrogen tank flange are welded. The two flanges for the inlet and outlet are welded outside, while the feedthrough port is welded inside. Then, the two tubes for the gas inlet and outlet are welded to the top of the purifier body. The purifier body top should have the mini-flange ports welded first (Fig. B.3). The welding of the tubes to the purifier body top flange should be done on the inside. Then the tubes, with the top flange, welds to the nitrogen tank flange. After this, the bottom flange should be machined and welded to the 3-3/8 flange (Fig. B.4, B.5). The final step involves welding the top flange, bottom flange and the body tube together (Fig. B.1).

All parts used for construction are 304 stainless steel. The nitrogen tank flange and the two purifier body flanges can be machined from disks. There are numerous companies to buy the materials from, such Speedy Metals or Industrial Metal Supply. For the inlet and outlet tubes, the OD is 5/8'' and wall thickness is 0.028''. The wall thickness is thinner than normal vacuum tubing to reduced heat transfer to the outside, but still thick enough to support the weight of the purifier body. The tubing can be bought at McMaster Carr. For the large 5'' tubing for the purifier body, again we want to use as thin wall as possible. Only Nor-Cal company sells 5'' tubing with 0.083'' thick wall, other companies have at least 1/8'' wall for tubing that big.

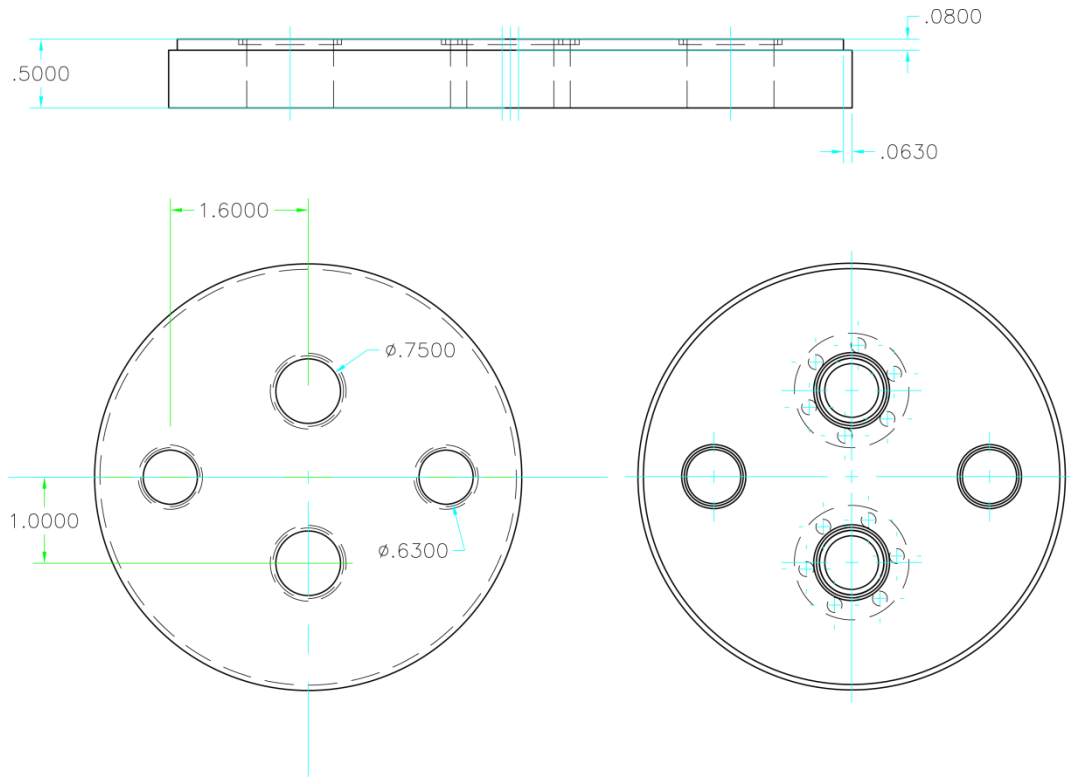


Fig. B.3: Generation 1 purifier body top flange

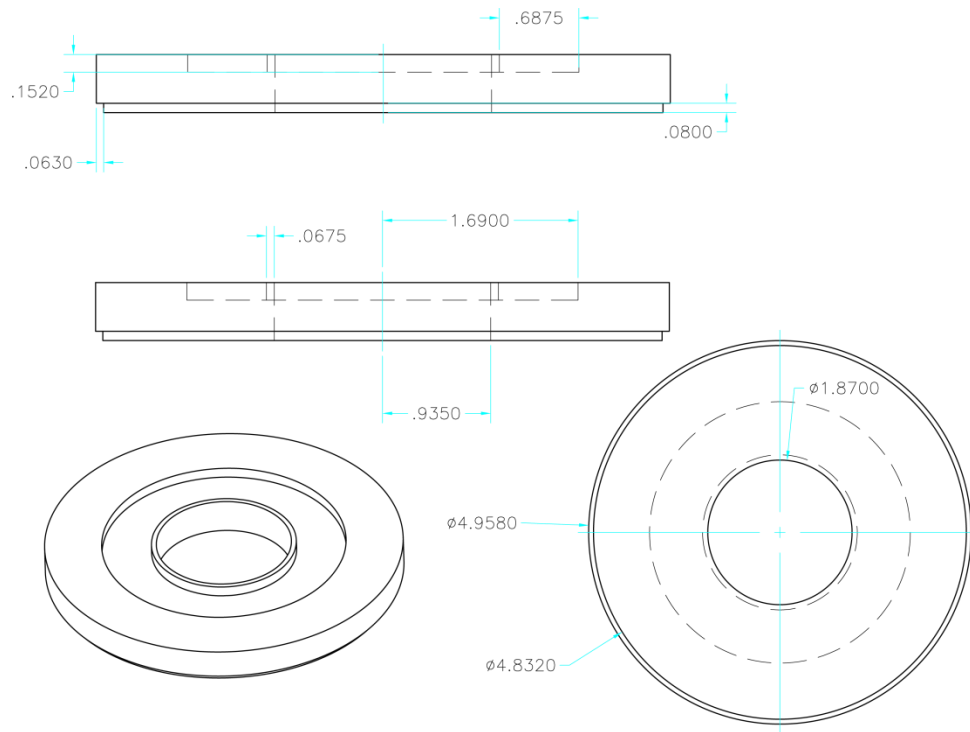


Fig. B.4: Generation 1 purifier body bottom flange

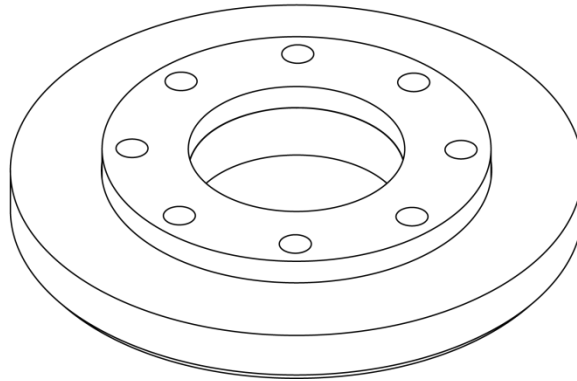
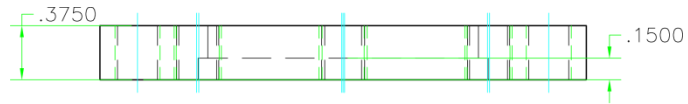


Fig. B.5: Generation 1 purifier body 3-3/8'' flange assembly.

At the outlet port, there should be a ball valve to seal the purifier when it is not being used. The ball valve needs to be custom made, with one end being mini-flange and the other quick-connect for the helium transfer line. To make this, the ball valve from McMaster Carr was chosen, with 3/4" tube endings for welding the connectors. The part number is: 44755K212 (this could change). After acquiring the valve, disassemble it by loosening the four screws. Keep the center sealing component safe, and take the two end parts to machine shop for welding. The lengths of the tubing should be as short as possible to minimize height of purifier. The exact length depends on the design. In general, the overall height of the purifier needs to be low enough such that the transfer tee will not bend when inserted. It is usually good to make it as short as possible. Fig. B.6 shows the drawings for welding the connectors to the ball valve, the dimensions are meant for Generation 3 purifier, but the procedure is same for all three.

One of the 2 center mini-flanges on the purifier body can be used to mount a temperature sensor. Type K thermocouple sensor was used, and the sensor was mounted on a threaded rod into the CF flange. The placement of the sensor is not ideal, as it is close to the top and not anchored thermally to any solid object. Ideally, we should have sensor buried inside the zeolite to get effective measurement of temperature.

Shortcomings / Improvements

The design, while simple and straightforward, does have drawbacks. Initially, the side with the long tube was chosen as the input side. When pumping and venting the purifier, it was found that the zeolite would get sucked in through the long tube and get into the valves at the inlet side. A screen was put in front of the inlet angle valve to solve the problem. In addition, another screen was put on the end of the long tube at bottom of purifier. To mount this, a Swagelok

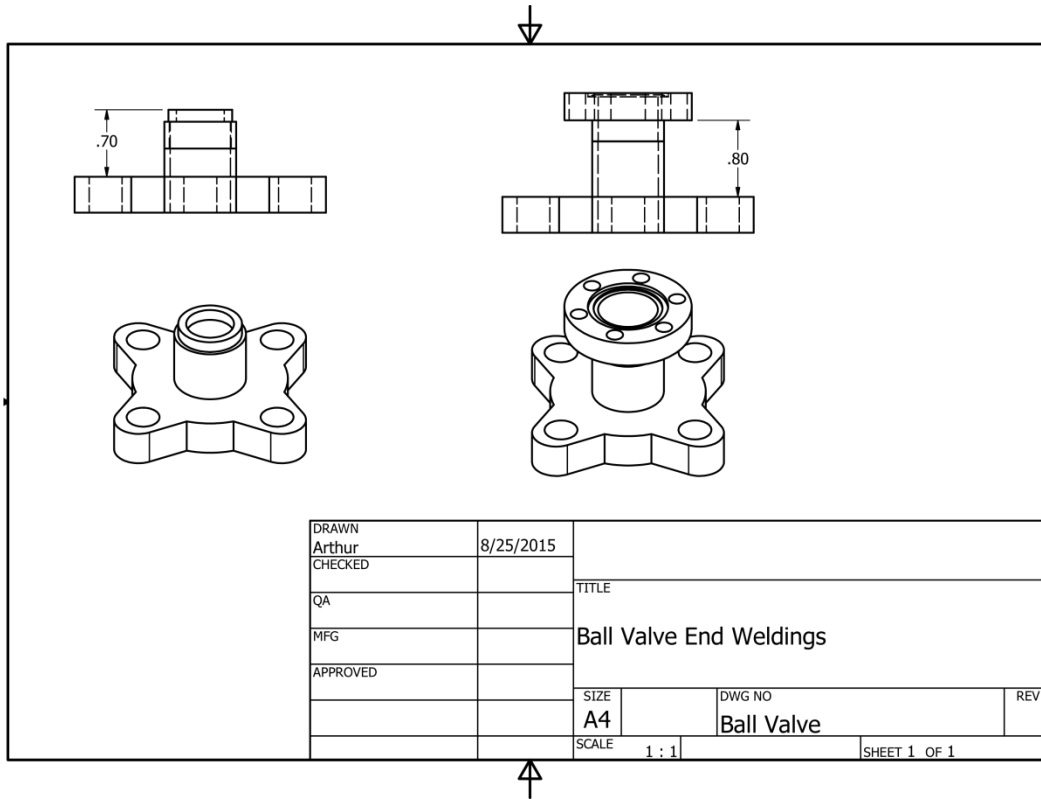


Fig. B.6: Welding for ball valve ends

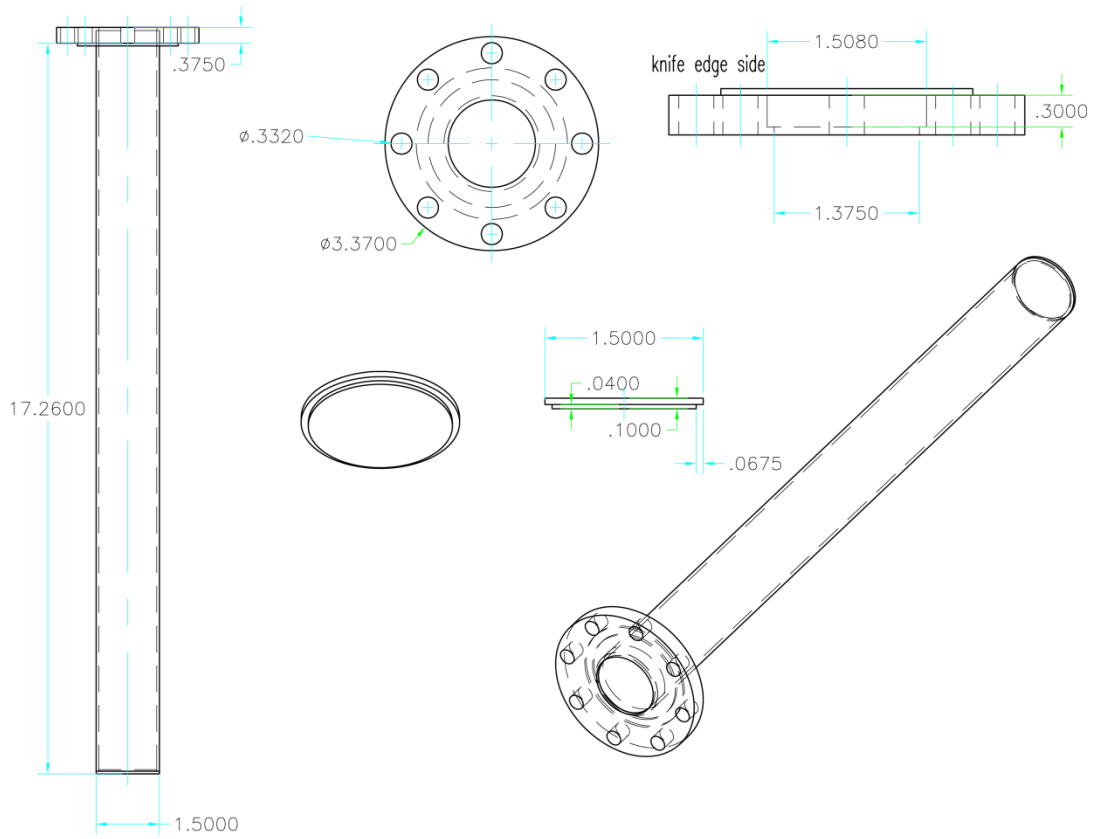


Fig. B.7: Center hollow tube for purifier bottom

connector is epoxied to the end of the tube and the screen is applied by hand tightening the matching connector with the screen.

After initial usage, another defect of this design is the temperature of the purifier body. Due to the large volume inside the body, the temperature at the center is not low enough. Our initial temperature reading was around 90 K. Furthermore, as the liquid nitrogen level decreases, the temperature is very sensitive to the liquid level and would rise to above 100 K. To combat this, a hollow tube was inserted into the center of the purifier from the bottom flange (Fig. B.7). Afterwards, the temperature reading became slightly lower, but now the purifier temperature is not as sensitive to nitrogen level as before, and can maintain temperature better as level drops.

B.3 Generation 2

Design

The experience of the generation 1 purifier gave us insights to improve the design. First, instead of complete welded assembly, it will be possible to disassemble the purifier into components. Second, the simple gas-in-gas-out approach puts all purification power in the zeolite, which decreases the lifetime of purifier before regeneration. We had problems with clogging early in generation 1 purifier's lifetime, which was only solved by introducing a "pre-purifier" into the system. We hope to have a two-stage purification system where the incoming gas is cooled by the outgoing gas and allows impurities to condense in a separate container before reaching the zeolite. We also like to maximize the time the gas spends in the zeolite, making the zeolite more effective.

Whole Purifier Assembly

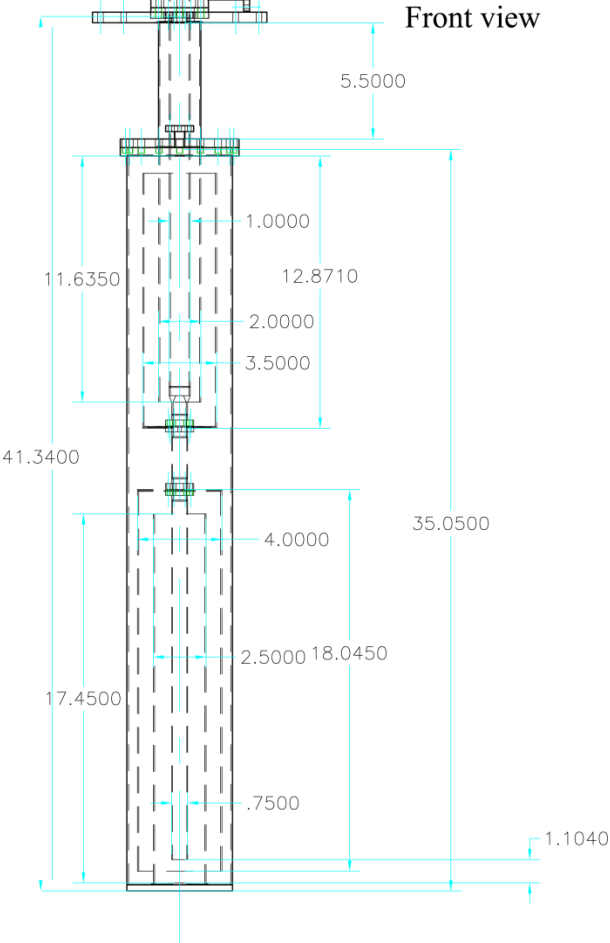


Fig. B.8: Generation 2 purifier overall view

Nitrogen Tank Flange Assembly

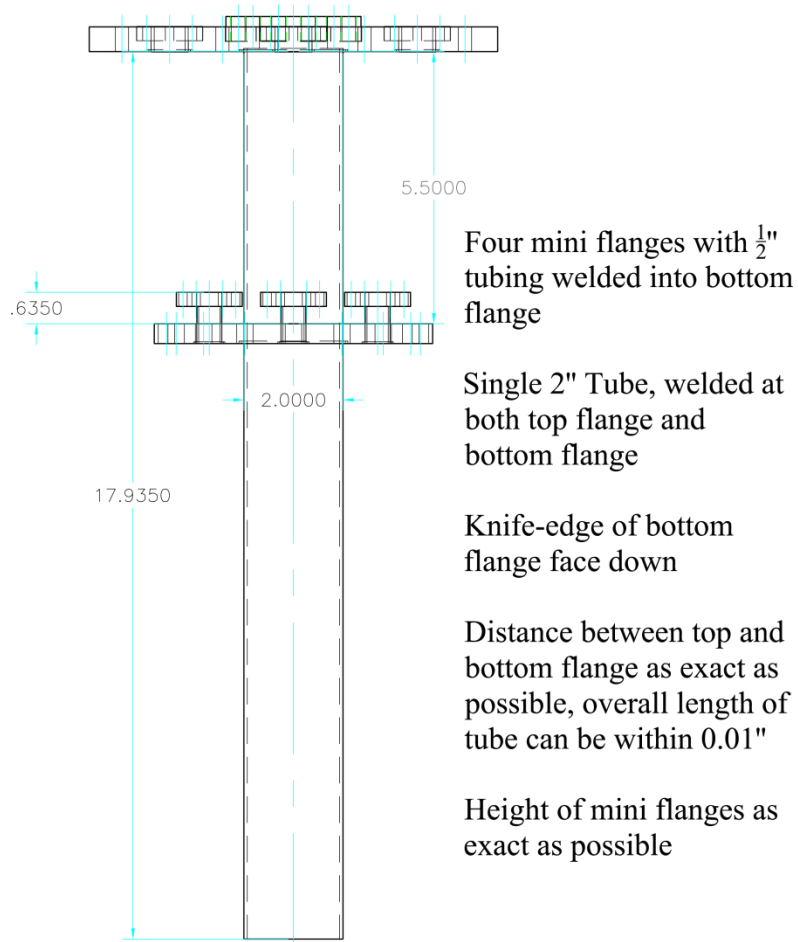
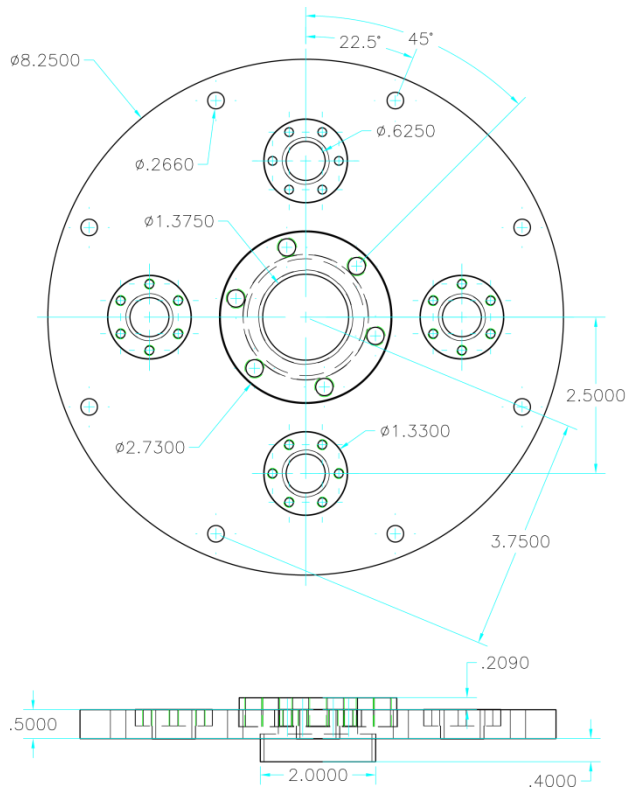


Fig. B.9: Generation 2 purifier nitrogen tank flange assembly



Nitrogen Tank Flange

-8.25" Flange with 8 through holes for $\frac{1}{4}$ -20 screws

-Center 2- $\frac{3}{4}$ " CF Flange with 1- $\frac{1}{2}$ " tubing opening, tapped, 0.209" above large flange

-4 mini CF Flanges, flushed with surface, tapped.

-Note orientation of all holes for all flanges

-short 2" tube welded to backside of flange

Fig. B. 10: Generation 2 purifier nitrogen tank flange

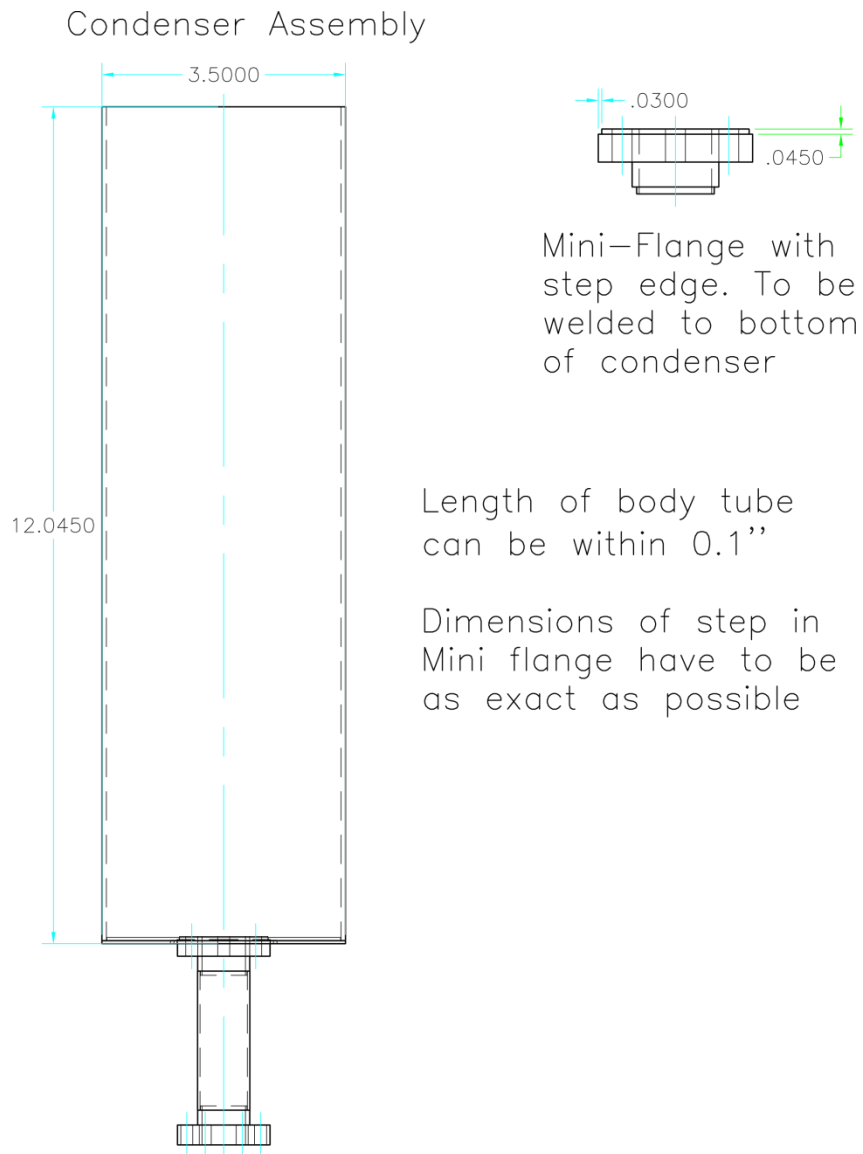


Fig. B.11: Generation 2 purifier condenser assembly

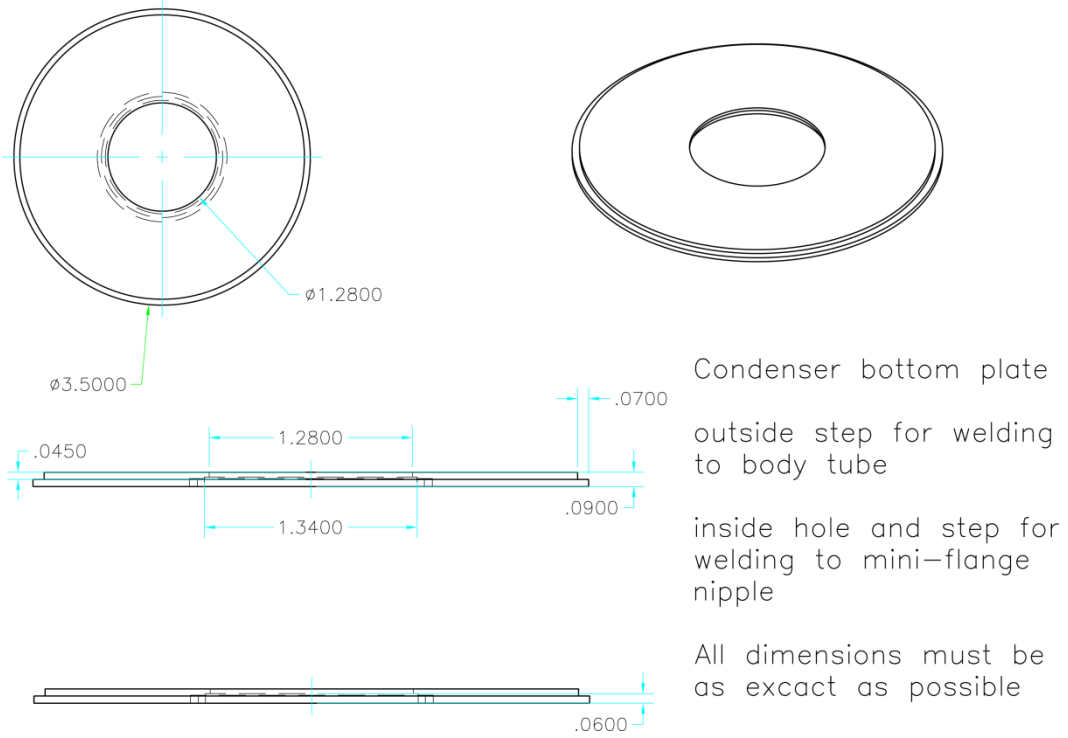
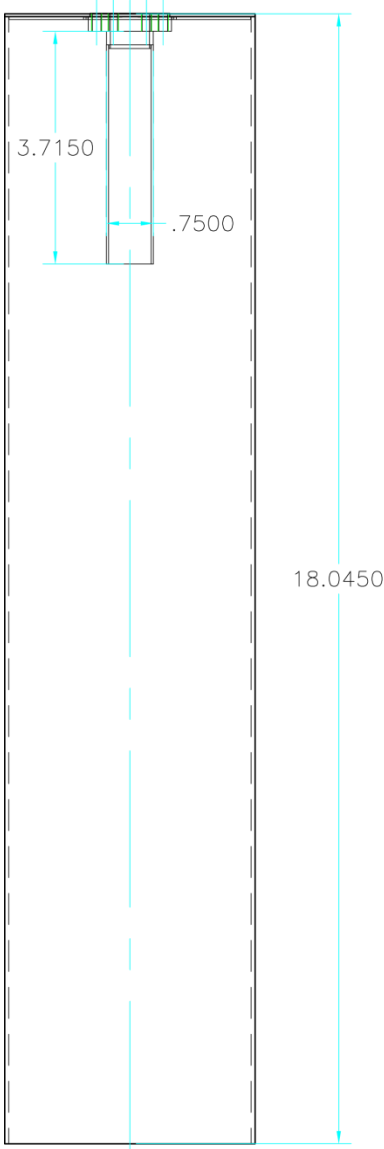


Fig. B.12: Generation 2 purifier condenser bottom plate

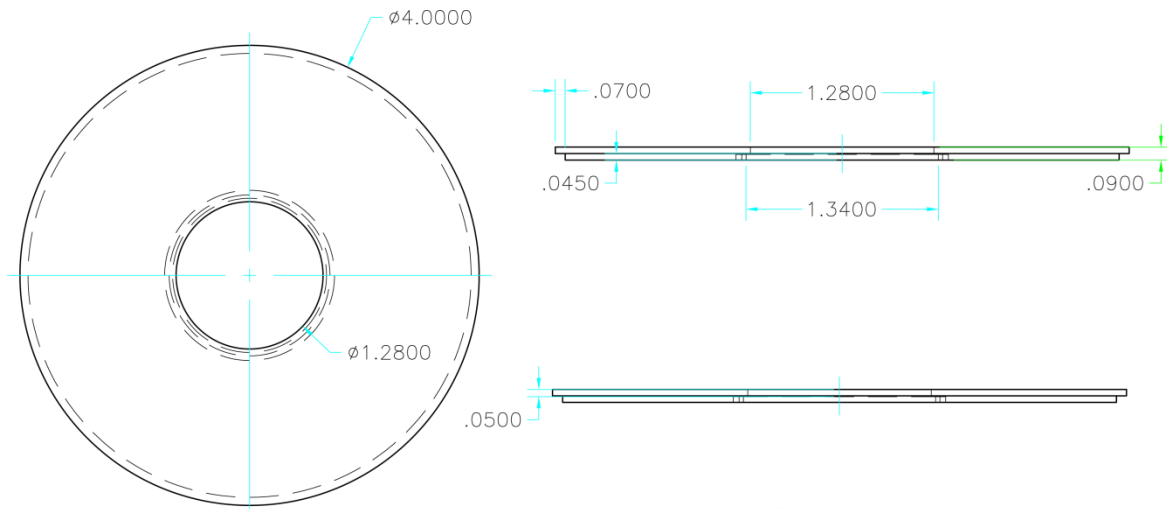
Outlet Gas Shield Assembly



Mini Flange welded to 0.75" Tubing.

Length of tubing and outside body within 0.1"

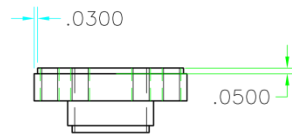
Fig. B.13: Generation 2 purifier outlet shield assembly



Shield for Outlet Gas, top plate

Similar to condenser, outer step for body tube, inner step for mini-flange

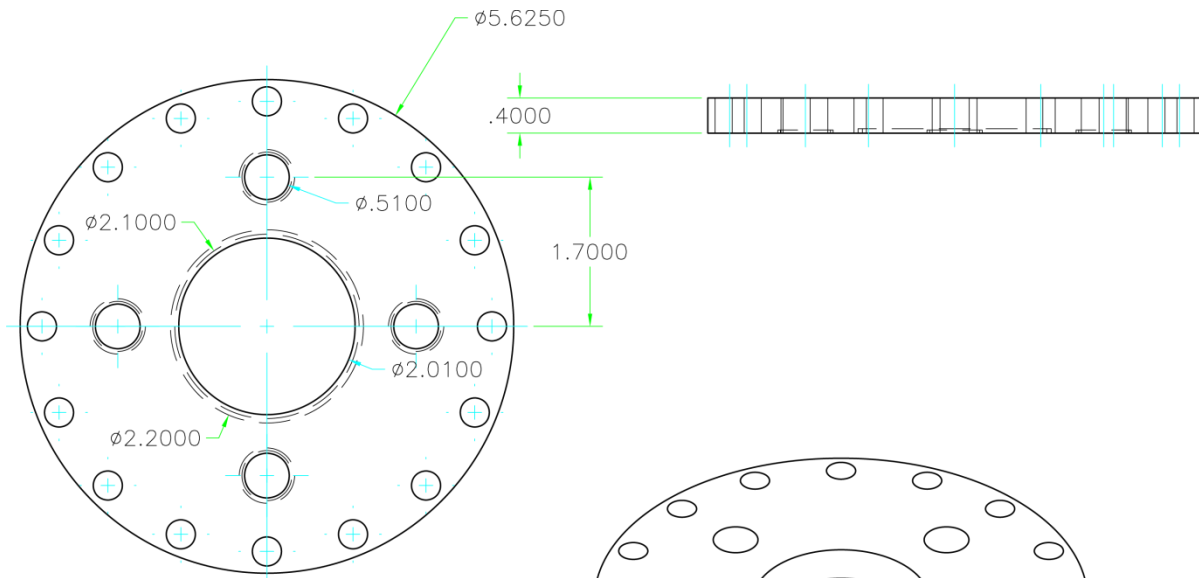
Dimensions as exact as possible



Mini-flange with step

Rotatable, Tapped

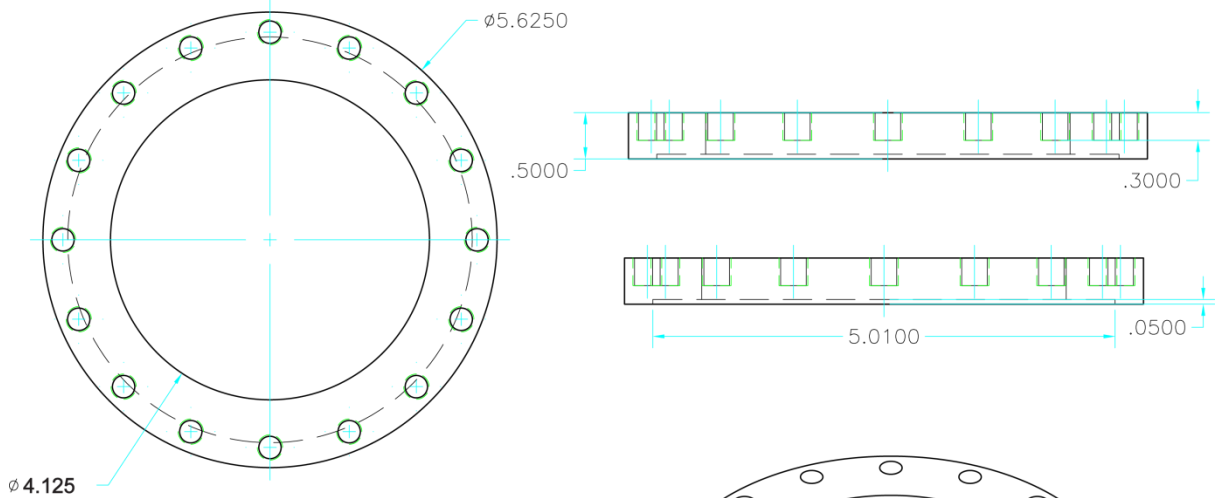
Fig. B.14: Generation 2 purifier outlet shield top plate



Custom Designed 6" CF Flange
(Cover for Purifier body)

Bolt holes, knife-edge same
OD = 5.625"
thickness = 0.4"

Fig. B.15: Generation 2 purifier cover flange



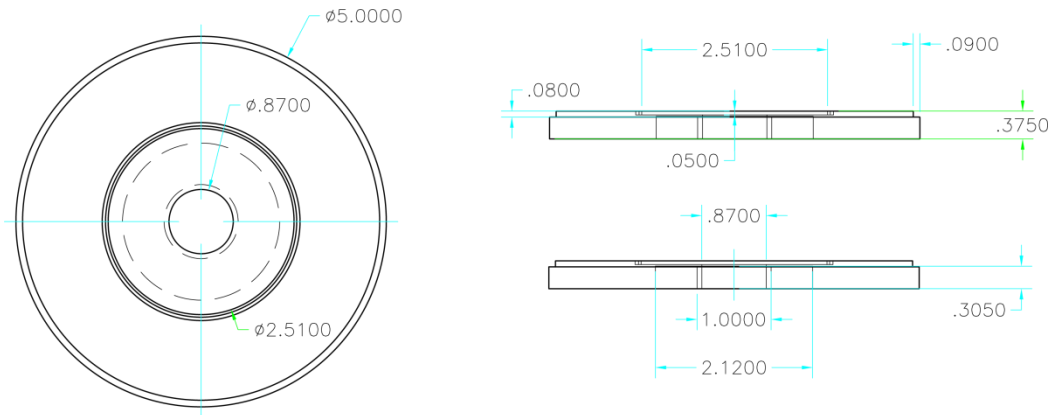
Top flange for purifier body

Custom made 6" CF Flange

Knife-edge as is, blind
tapped holes instead of
through holes, thinned down

To be welded to 5" Tube

Fig. B.16: Generation 2 purifier body top flange



Bottom Flange for Purifier body

outer step for welding to body tube

center step for welding tubing to hold zeolite

Weld $2-\frac{1}{8}$ " CF Flange to Backside of Flange

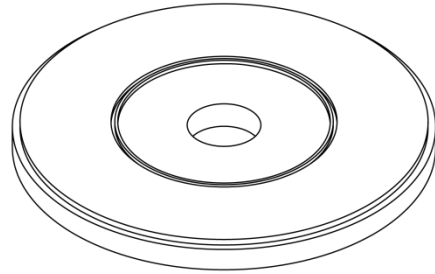
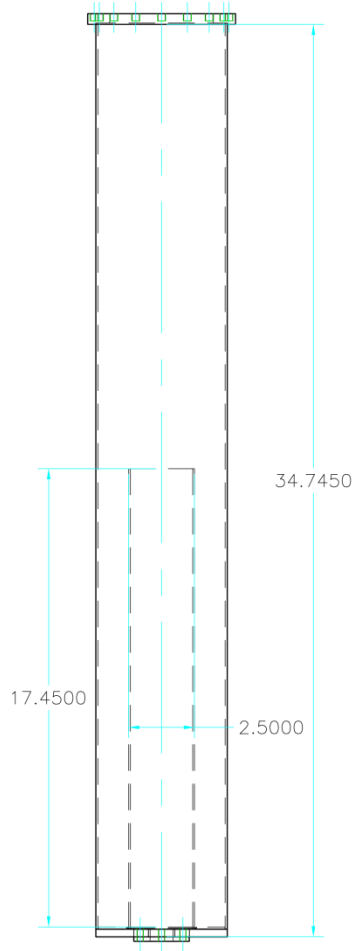


Fig. B.17: Generation 2 purifier body bottom flange



Purifier Body Assembly

Center Zeolite Tube welded to bottom flange

2- $\frac{1}{8}$ " CF Flange weled to backside of bottom flange

Lengths of body tube and zeolite tube within 0.1"

Fig. B.18: Generation 2 purifier body assembly

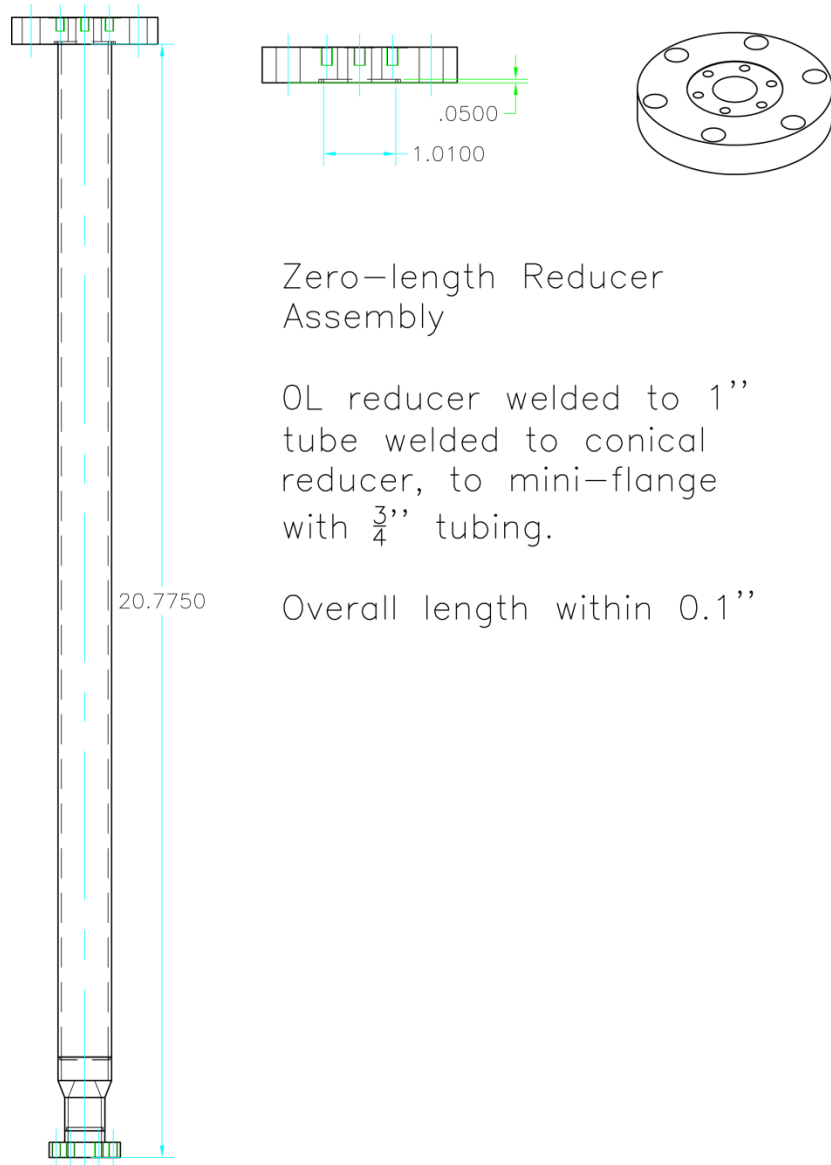


Fig. B.19: Generation 2 purifier zero-length reducer assembly

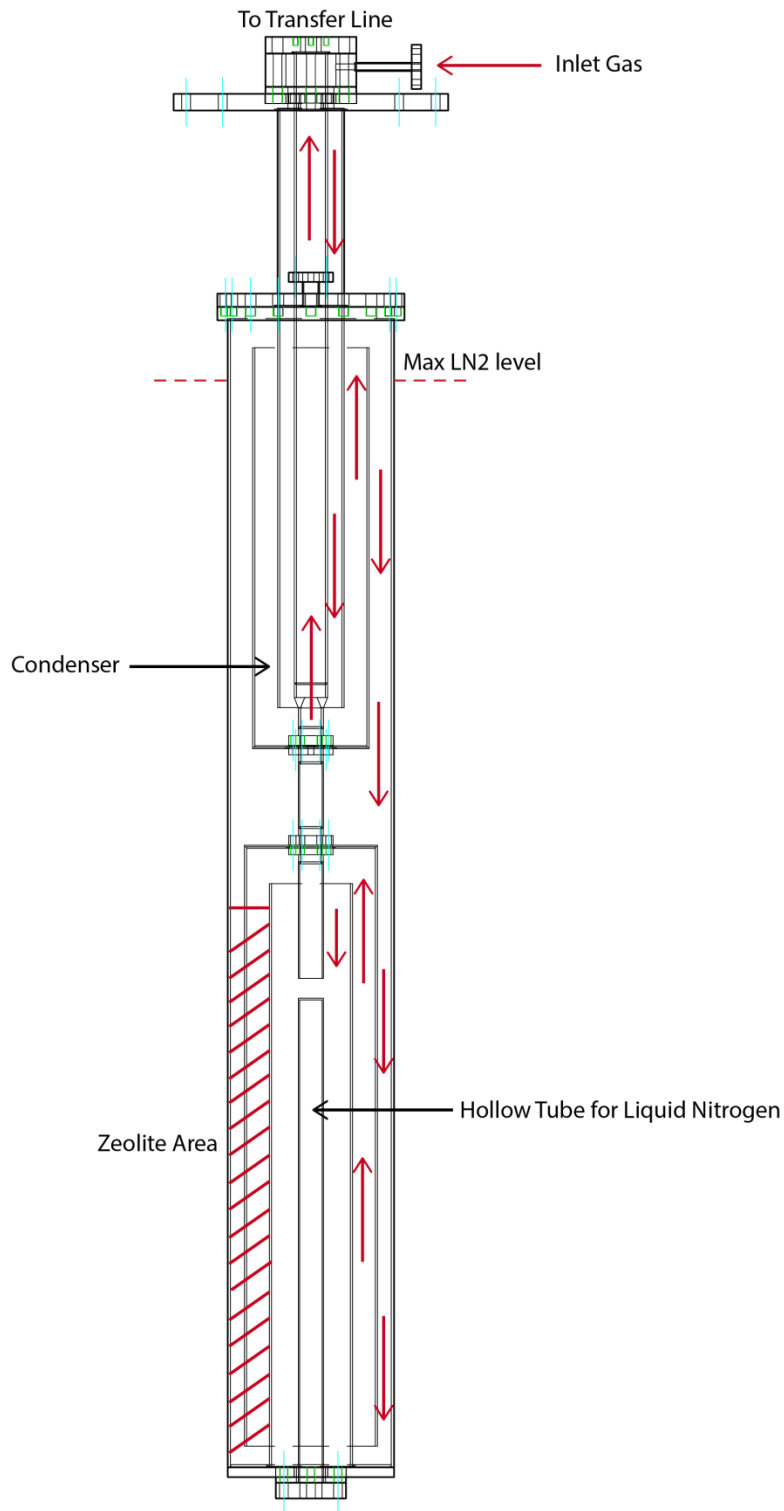


Fig. B.20: Gas flow for generation 2 purifier

The overall design of the generation 2 purifier is shown in Fig. B.8. The generation 2 purifier has three main components: nitrogen tank assembly (Fig. B.9, B.10), condenser assembly (Fig. B.11, B.12), and gas outlet assembly (Fig. B.13, B.14). The purifier body is now also separated into three flanges: the cover flange (Fig. B.15), the body top flange (Fig. B.16), and the body bottom flange (Fig. B.17) together make up the purifier body (Fig. B.18). The outlet of the purifier goes through a one-inch tubing welded to a zero-length reducer (Fig. B.19). The reducer connects to the ball valve in the same way as the generation 1 purifier. In the return path, the time of helium gas in the zeolite was increased further by having an outlet shield. Such a shield also puts the outlet opening farther away from the zeolite, decreasing the likelihood of a clog happening. The complete helium gas path is shown in Fig. B.20.

Construction

The construction of the generation 2 purifier is more complicated. There are many different parts that need to be made. To start, the four big flanges need to be custom made and ordered. To order the flanges, drawings need to be sent to different companies for quotes. It's important to note the orientation of all the holes and mini-flanges when placing order. The generation 2 purifier flanges were ordered from Nor-Cal company. For the different tubes used in the design, the 2", 1" and 0.75" tubes can be purchased from vacuum companies like Nor-Cal. The larger diameter tubes at 2.5", 3.5", and 4" can be purchased from Speedy Metals company or Industrial Metal supply. The 5" tube for purifier body should still be purchased from Nor-Cal due to their availability of tubing with 0.083" wall thickness. In general, the tubes with the thinnest wall thickness should be used.

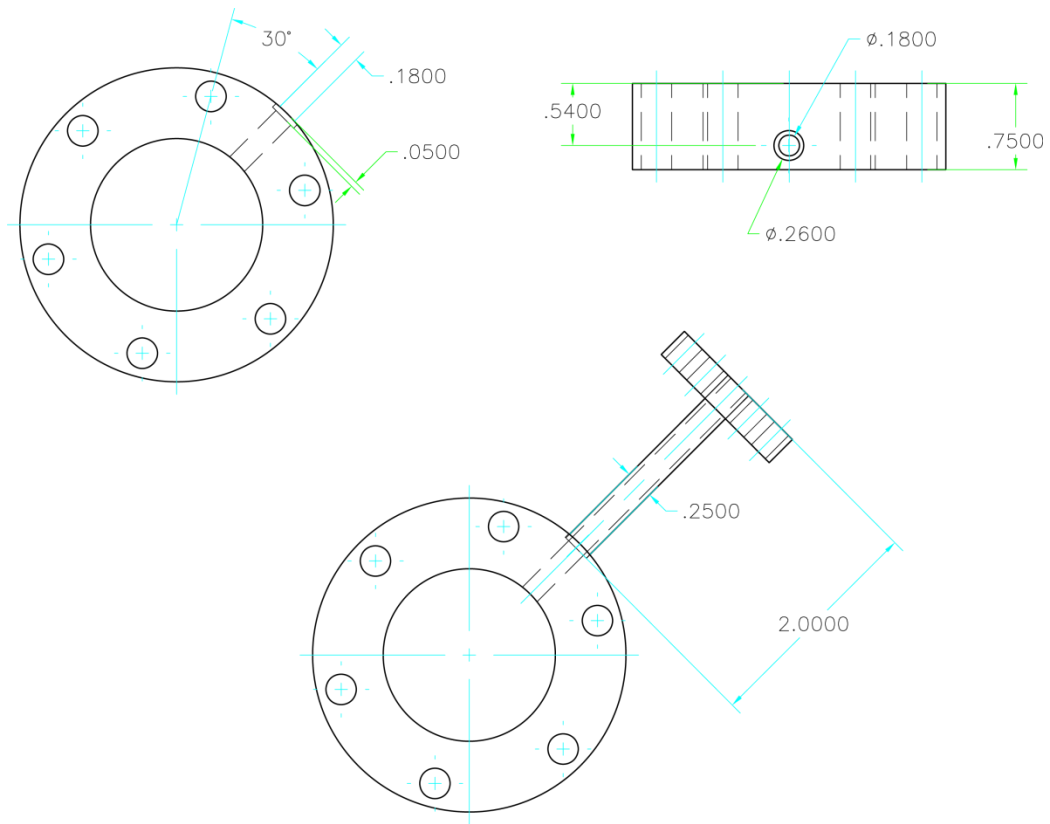


Fig. B.21: Doubled-sided flange assembly

After the flanges have been ordered, the different assemblies can be made. First, the nitrogen tank flange assembly needs to be welded. The nitrogen tank flange, 2'' tube and purifier cover flange are welded together to form the nitrogen tank assembly (Fig. B.9). The internal assemblies for the condenser and gas outlet also needs to be made (Fig. B.11 and Fig. B.13). For the condenser assembly, welding of the bottom plate to the mini-flange needs to be done carefully as so the knife-edge remains protruded out to give effectively seal. Similar consideration needs to be made for outlet gas assembly. Similar to construction of the purifier body in generation 1, the purifier body is welded together with the top flange, outside tube, and bottom flange (Fig. B.18). Be sure to weld the zeolite tube to bottom flange first before welding the purifier body tube. The center zero-length reducer assembly and the double sided flange for inlet gas also need to be welded (Fig. B.21). The ball valve at outlet follows same design as previous version.

After all assemblies are constructed, the different parts are put together. The intricacy of the design means that the procedure to put everything together must be followed closely. First, the double-sided flange inlet and zero-length reducer assembly are installed. Note that we need long screws for this, so prepare in advance. Next, the condenser assembly is installed. This could be a challenge since we cannot see the flange at end of the 1'' tube when installing the condenser. The flange is tapped, so we should be able to insert screws from the bottom and tighten the flange. After the condenser, the outlet gas shield can be installed. Again, the flange on the gas shield should be tapped. After this step, the inner structure of the purifier is finished. We can tape thermal couple wire to the bottom of the gas shield to monitor temperature inside the zeolite. A second thermal couple sensor could be mounted on the condenser. In generation 2 purifier, Type E thermal couple is used due to better performance at low temperature.

The final step in the purifier assembly is putting the zeolite into the purifier body and inserting the whole structure into it. The zeolite should go on the outside of the tube inside the purifier body (Fig. B.20). Since we need to insert the purifier structure, it's best to not fill the zeolite completely at first. Fill it halfway, insert the purifier inside the body as much as possible but without closing the flanges. Use a soft tube or hose to fill the rest of the zeolite through the gap between the flanges. When the zeolite is filled, close the flanges together. It may be difficult due to the friction with the zeolite, use long screws to slowly close the gap between the two flanges.

Shortcomings / Improvements

The generation 2 purifier suffers from several design defects. Soon after putting into use, it was found that the much larger purifier body made it difficult to cool. The measured temperature both at the top and bottom of the purifier was higher than that found in generation 1. The shortened length of the neck meant that as the nitrogen level lowers, the top of the purifier would be exposed outside of the liquid. The big center 2'' tube also meant there is more conductance with the outside. All these factors made the cooling power of this purifier less than the previous version.

Besides the higher temperature, there are some other design flaws in the generation 2 purifier. In the condenser and outlet shield, the mini-flange making the connection have through holes, thus the gas can leak through, bypassing the condenser and worse, the zeolite. Such a problem can cause major issues with the liquefier system. In the early usage, it was found that the purifier was not effective due to constant clogging. The leak problem was found and temporary solution is to use epoxy to seal all the screws. It was also found that the condenser had

substantial amount of ice in it, meaning it has served its purpose to collect impurities before it has chance to get to the zeolite. In future designs, the condenser should be retained as a useful feature, but implementation should be improved to get rid of the leak problem associated with using CF flanges.

On a practical level, the design of the outlet shield made inserting purifier into the body very difficult due to friction with the zeolite. The performance advantage of such design, if any, does not outweigh the difficulty such a design has in assembling the whole purifier together. In the future, going back to the simple single tube into the zeolite would be better. Overall, the generation 2 has not been a success. Its many design innovations do not cover up the flaws. We did learn a lot from the design and construction process, though, and it will help in the design of the generation 3 purifier.

B.4 Generation 3

Design

Based on the lessons learned from the generations 1 and 2 purifiers, the design of the generation 3 incorporates features from both designs. The heat exchange between inlet and outlet gas will be retained, as well as the condenser assembly. But the length of the neck portion will be lengthened, to make sure the whole purifier assembly is submerged in the liquid nitrogen. This necessitates the shortening of the condenser, which will make it less effective, but the compromise is worth it. The overall layout of the design is shown in Fig. B.22.

The biggest change from generation 2 is the return to a simple tube into the zeolite for the outlet as in generation 1 (Fig. B.22). The elimination of extra layers, and the shortening of the purifier body, creates space for zeolite roughly equal to that in the generation 1 purifier. Another

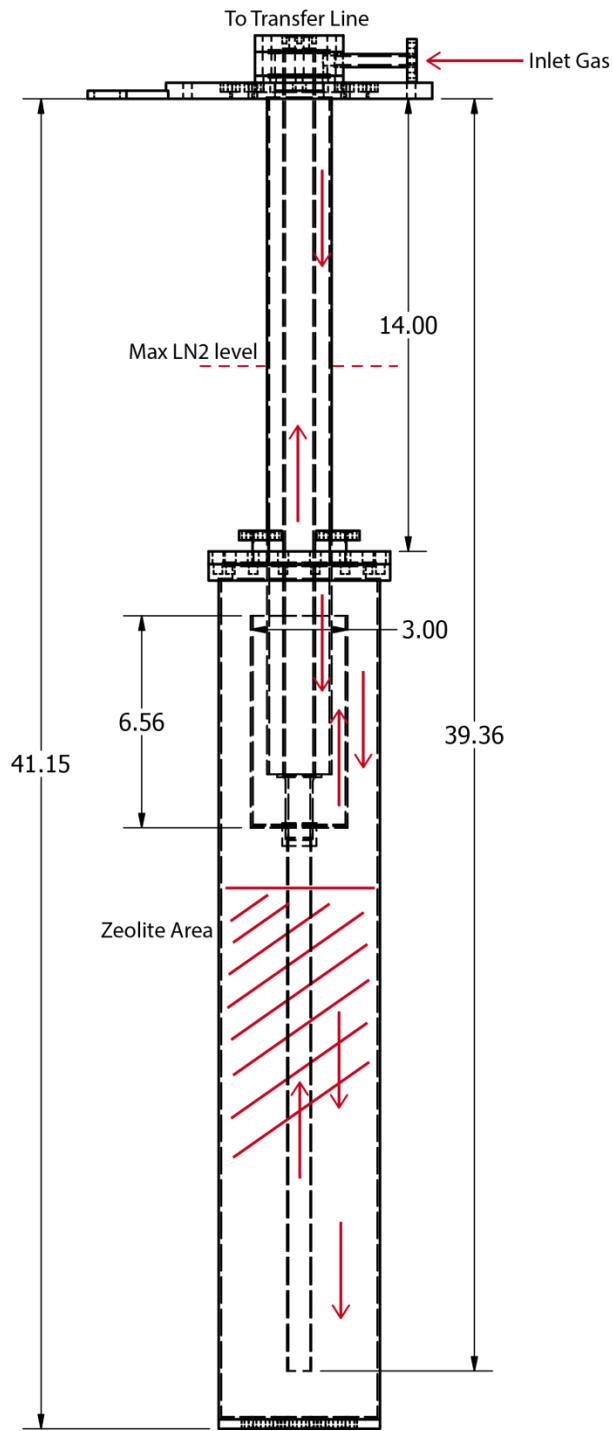
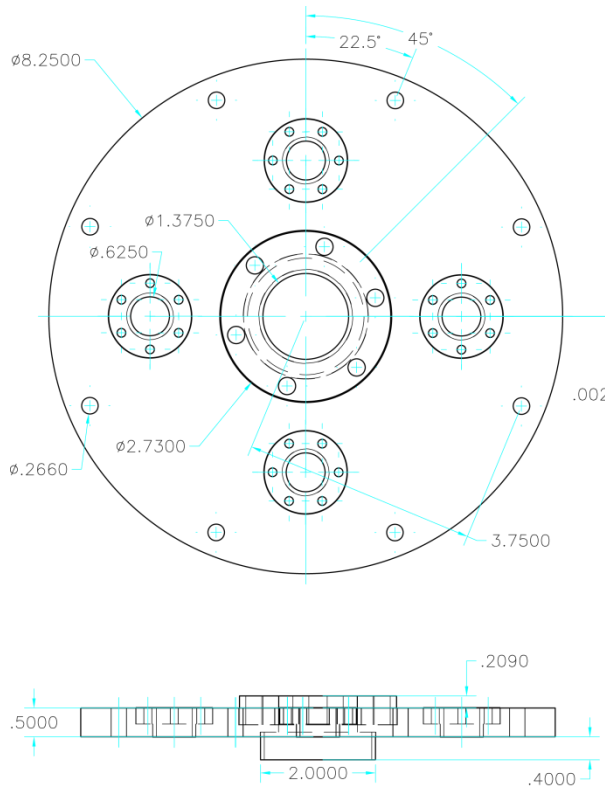


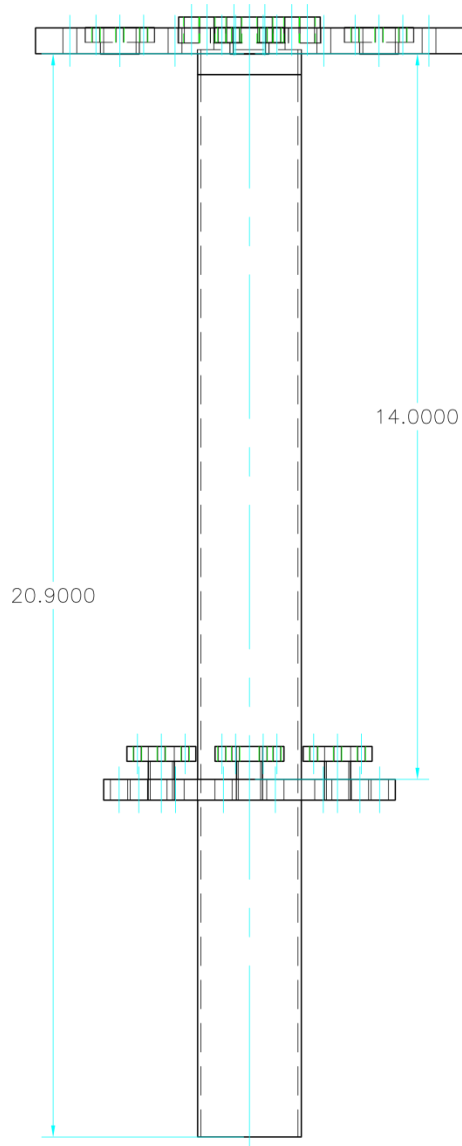
Fig. B.22: Generation 3 purifier overall layout



Nitrogen Tank Flange
(Flange 1)

- 8.25" Flange with 8 through holes for 1/4-20 screws
- Center 2-3/4" CF Flange with 1-1/2" tubing opening, tapped, 0.209" above large flange
- 4 mini CF Flanges, flushed with surface, tapped.
- Note orientation of all holes for all flanges
- short 2" tube welded to backside of flange

Fig. B.23: Generation 3 purifier nitrogen tank flange



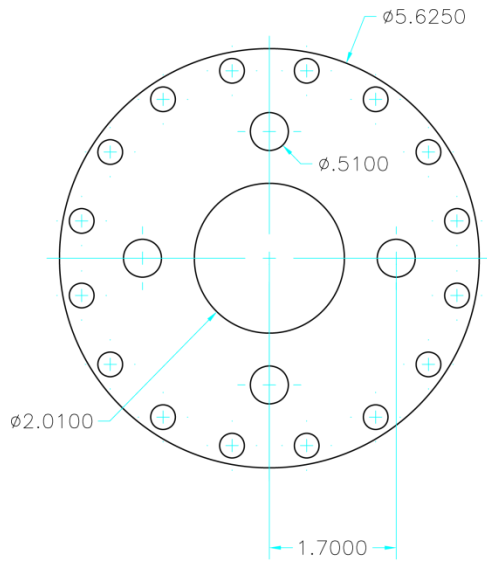
Nitrogen Tank Flange Assembly

–2” Tube welded to back of nitrogen tank flange

–Cover Flange welded to 2” Tube.

–Gap between flanges exact, Total length can be within 0.1”

Fig. B.24: Generation 3 purifier nitrogen tank flange assembly



Cover Flange (Flange 2)

–6”CF Flange with modifications

–OD to 5.625”, thickness to 0.4”, through bolt holes

–Center hole for 2” tubing, side holes for 0.5” tubing

–Note orientation of bolt holes in relation to 0.5” holes

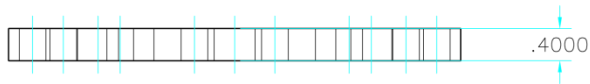
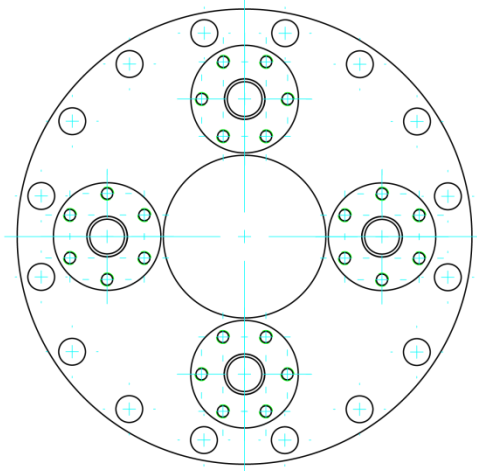


Fig. B.25: Generation 3 purifier cover flange



Cover Flange Assembly

–4 mini CF Flanges with 0.5” tubing welded to Cover flange.

–Mini flanges to be tapped

–Note height of mini flanges, can be within 0.1”

–Note orientation of tapped holes on mini flanges to center hole

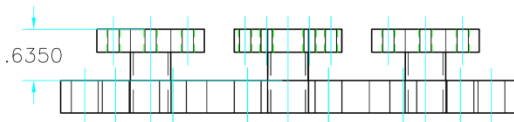
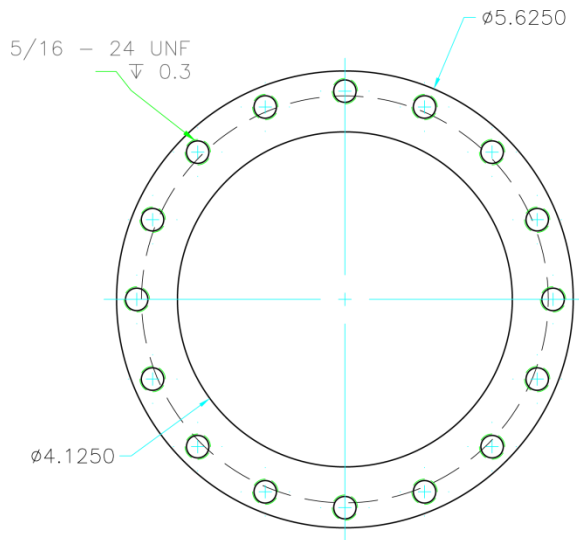


Fig. B.26: Generation 3 purifier cover flange assembly



Top Body Flange (Flange 3)

-6" CF Flange with modifications

-OD to 5.625", thickness to 0.5". Blind tap holes to 0.3"

-Center hole at 4.125"

-Shallow step on back of flange for welding to 5" tubing

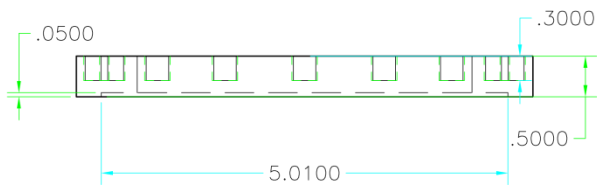
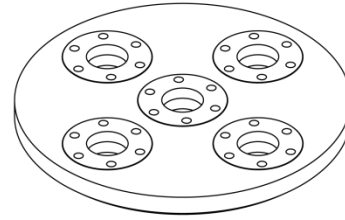
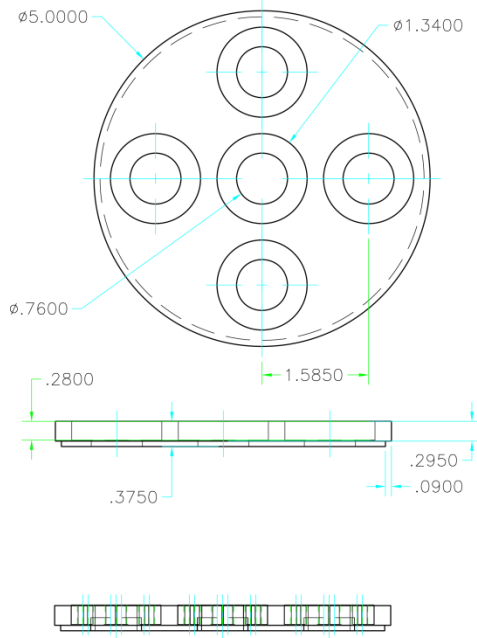


Fig. B.27: Generation 3 purifier body top flange



Bottom Body Flange (Flange 4)

–outer step for welding to 5” tubing.

–inner holes for mounting 1.33” CF flanges with 0.75” ID

–surface of mini-flanges should be flushed with surface of big flange (can protrude slightly)

–All dimensions as exact as possible

Fig. B.28: Generation 3 purifier body bottom flange

improvement on the design is the use of NPT for the condenser assembly. This removes the leak problem caused by the through holes in CF flanges.

Other minor changes include decreasing the diameter of the condenser slightly, so that it will be easier to put zeolite into the purifier through the mini-flanges on top without the zeolite going into the condenser. Because the outlet tube is at the center now, it will be impossible to insert hollow tube in center for liquid nitrogen. To counter this, extra mini-flanges were added on the side on the purifier bottom flange (Fig. B.27). Copper rods can be inserted through these ports into the zeolite to increase thermal conductivity.

Construction

As in generation 2 purifier, the design is subdivided into assemblies that can be constructed separately. The nitrogen tank flange, cover flange, and body top flange follows basically same design as in generation 2 (Fig. B.23 – B.28). Instead of just ordering the flanges and ask the machine shop to weld the assemblies together, the generation 3 purifier was ordered directly from the company. All the drawings were sent to company and the nitrogen tank assembly and the purifier body assembly were made completely by company. Building the purifier this way reduces the workload of the machine shop, which can take a while as there is only one person who does the welding. When sending the drawings to companies, make sure to specify the orientation of bolt holes and flanges. As always, leak check the parts after it has arrived.

When assembling the generation 3 purifier, the condenser assembly is the key (Fig. B.29). The zero length reducer and double sided flange is same as in generation 2. The center one inch tube welded to the zero length reducer has been extended, an NPT half nipple welded to end of the one-inch section and a 0.75” extension was also added to reach near bottom of zeolite (Fig.

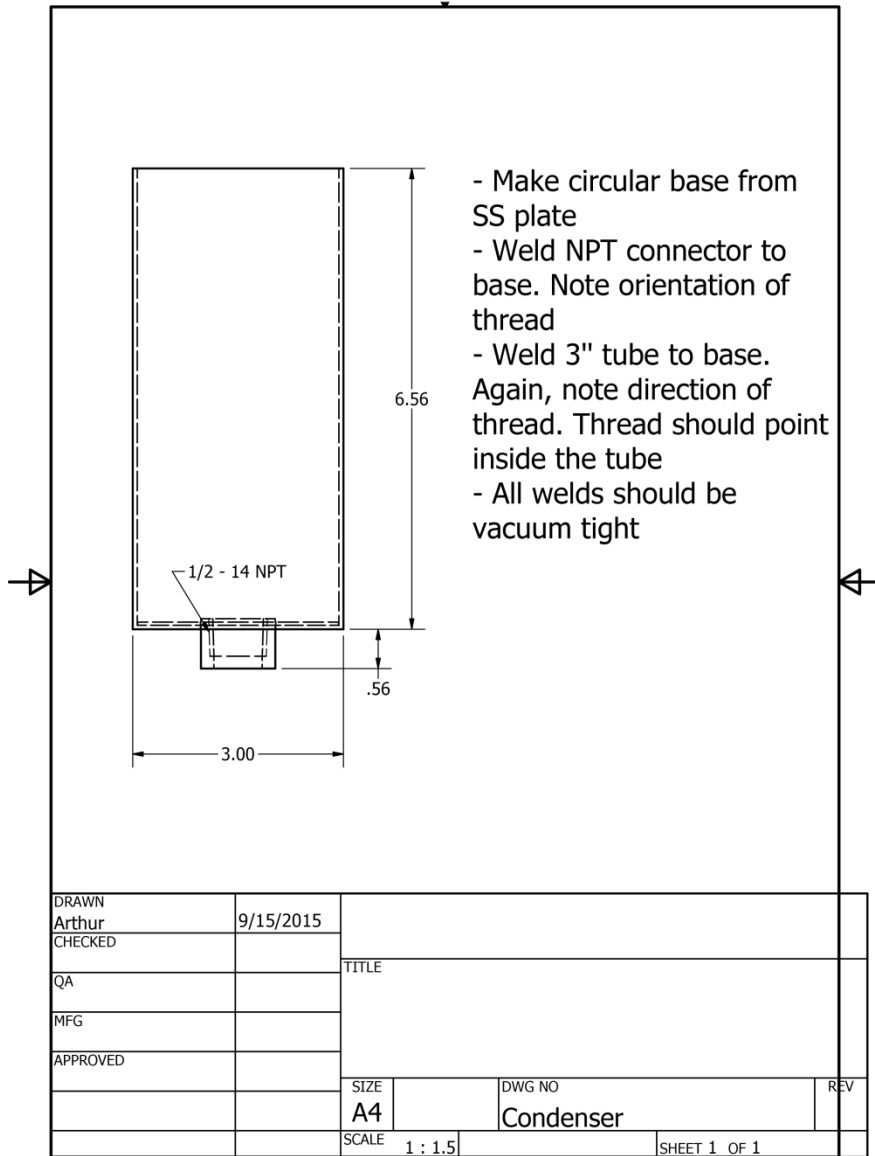


Fig. B.29: Generation 3 purifier condenser assembly

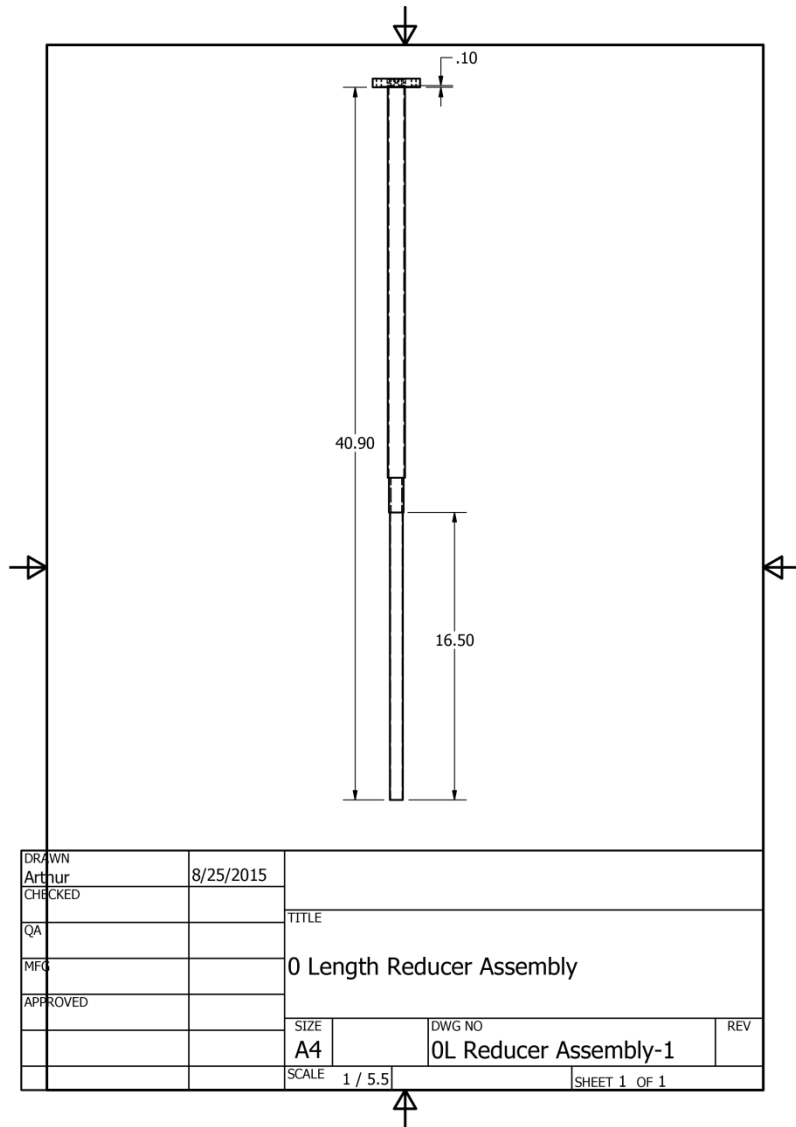


Fig. B.30: Generation 3 purifier zero-length reducer assembly

B.30). An NPT adaptor is also welded into the condenser, which allows it to be screwed onto the center tube. After installing the condenser, the whole structure can be inserted into the purifier body. The zeolite can be poured through the mini-flanges on top. To measure temperature, thermal couple leads can be taped to the center tube at the bottom and the condenser. Copper rods can be added to the side flanges on the purifier body bottom flange.

Future Improvements

The generation 3 purifier has proven to be very effective in the time it was put into use, despite the fact that the copper rods are not implemented yet. Out of the three designs, generation 3 performs the best. During the several months that this purifier was in operation, we have not had clogging problems or had to regenerate the zeolite. The presence of the condenser, coupled with larger volume of zeolite and lower temperature compare to generation 2, give generation 3 purifier the edge in performance. To further improve the design, several minor changes are proposed. On the nitrogen tank flange, the number of holes to mount to the tank was increased to 16. This way, the orientation of the purifier with respect to the nitrogen tank can be adjusted. Further, the double-sided flange with the inlet tube can be changed to a NPT connector, which increases the flow rate at the inlet side.